



School of Engineering and Physical Sciences

Department of Electrical Electronic and Computing Engineering

Master of Science Dissertation

Design and Fabrication of Multilayer Piezoelectric NEMS Resonators

Muhammad Faizan

July 2016

Supervisors: Prof. Guillermo Villanueva (EPFL)

Prof. Marc Desmulliez (HWU)

Abstract

We have successfully demonstrated the fabrication of self-actuating multilayer NEMS resonators including cantilevers and double clamped beams. Resonant sensors are widely used as precision mass sensors for the detection and quantification of small concentration of analyte molecules in a gaseous solution or bacteria from biological sample which requires extremely high mass sensitivity and responsivity of the resonant sensor. Nanofabrication techniques have enabled the use of ultrathin layers for the fabrication of resonant sensors to significantly enhance sensitivity by reducing the mass of the sensor. Aluminum nitride (AlN) as an ultra-thin PZE layer has significant advantages over other transduction techniques due to its high PZE efficiency, good mechanical and thermal stability and compatibility with CMOS processing. 50nm ultra-thin layer of AlN was deposited over 25nm thin layer of platinum (Pt) in order to get well textured columnar growth of AlN crystals. AlN deposition parameters were carefully optimized to enhance piezoelectric response. The residual stress and piezoelectric properties of AlN film were studied as a function of deposition conditions. Short circuiting of electrodes was the most critical problem which was solved after implementing two different process flows. Oxide bridges were fabricated in order to avoid unwanted electrical contact between different metallic layers. At the end, suspended cantilevers and beams were suffering from bending due to high compressive stress in the active layer. Residual stress of -169.80 MPa was calculated using Stoney formula by measuring the curvature of wafer before and after the deposition of individual layers.

Numerous studies have already been done on shifting of the resonance frequency due to the variations in attached mass on the surface of a resonator but there is still room for the investigation of surface stress changes on the resonance frequency. Application of surface stress induces a change in beam stiffness and dimensions which alter the resonance frequency of the cantilevers and doubly clamped beams. The motivation of this project was to carried out different experiments to study the effect of surface stress on the resonance frequency by using an active piezoelectric layer for the actuation of resonant structures. Application of voltage across PZE layer generates a longitudinal stress across the beam which leads to a shift in resonance frequency. Vibrometer was used to find the resonance frequency of the released devices.

Acknowledgements

I would like to thank my project supervisors Prof. Guillermo Villanueva from EPFL and Prof. Marc Desmulliez from HWU for their support and guidance throughout the project. Their valuable advice and technical discussions helped me in increasing my knowledge of the respective field and achieving the project objectives successfully.

Secondly, I would like to express my sincerest gratitude to Annalisa De Pastina for helping me out in the fabrication of oxide bridges. Special thanks to Kaitlin Howell, Andrea Lozzi, Marco and all the members of Advance NEMS group for making my stay cheerful and wonderful.

Last but not the least, I am grateful to my parents for their encouragement and unwavering support throughout the duration of my master dissertation.

Table of Contents

Chapter 1: Introduction	8
1.1. Background.....	8
1.2. MEMS/NEMS Resonator	10
1.3. Microcantilever Beam Resonator.....	10
1.3.1. Modes of Operation	11
1.3.2. Commonly used methods of resonator excitation and detection principles.....	12
1.3.3. Applications of Micro cantilever Resonators	15
Chapter 2: Multilayer Piezoelectric NEMS Resonator	19
2.1. Piezoelectricity	19
2.1.1. Piezoelectric Coefficients	19
2.1.2. Piezoelectric Charge Coefficients	20
2.2. Proposed design of Multilayer Piezoelectric Resonator	20
2.3. Aluminum nitride material characterization.....	21
2.3.1. DC Pulsed reactive magnetron sputtering for AlN thin films	22
2.3.2. Effect of deposition conditions on AlN growth	23
2.3.3. Platinum electrode layer for AlN thin film growth.....	28
2.4. Optimization of AlN deposition parameters	30
Chapter 3: Finite element analysis of multilayer piezoelectric resonators	33
3.1. Structural Analysis.....	34
3.2. Modal Analysis	36
Chapter 4: Fabrication	39
4.1. First Process Flow	40
4.1.1. Mask Design	41
4.1.2. Experimental Work.....	42
4.1.3. Discussion	53
4.2. Second process flow.....	58
4.2.1. Mask Design	59
4.2.2. Experimental work	60
4.2.3. Discussion.....	71
4.3. Resonance frequency measurements.....	74
5. Conclusion	76
6. References	78

List of Figures

Figure 1: Components of MEMS smart system	8
Figure 2: Application areas of MEMS resonators	10
Figure 3: Cantilever sensor modes of operation: (A) dynamic mode detecting mass changes on the cantilever by changes in resonance frequency; (B) bimetallic mode detecting temperature changes by a static bending due to different thermal expansion of the metal layer and silicon cantilever; (C) static mode where asymmetrical molecule absorption cause tensile stress, results in bending the cantilever upwards; (D) static mode where asymmetrical molecule absorption cause compressive stress, results in bending the cantilever downwards [15].....	11
Figure 4: Block diagram of a resonant sensor.....	12
Figure 5: Different excitation and detection techniques for microcantilever resonators [18]	14
Figure 6: Basic components of a chemical sensor	16
Figure 7: SEM image of silicon-based resonant cantilever with hexafluoro-2-propanol functionalized mesoporous silica sensing film [31]	16
Figure 8: PZT based self-sensing microcantilever [36].....	17
Figure 9: Direction of forces affecting a piezoelectric element.....	19
Figure 10: Block diagram of Multilayer Piezoelectric Resonator	21
Figure 11: Schematic diagram illustrating the basic components of a magnetron sputtering system [49]	22
Figure 12: Basic mechanism of Pulsed DC magnetron sputtering. Positive pulse reverse the potential on the target and attracts electrons in order to neutralize the positive charge buildup on the insulator surface [52]	23
Figure 13: Rate of deposition of AlN film as function of substrate temperature [53]	24
Figure 14: SEM cross-sectional view of AlN thin films deposited at different substrate temperatures of (a) 60 °C (b) 160 °C (c) 250 °C (d) 340 °C (e) 430 °C (f) 520 °C [53].....	25
Figure 15: AlN film deposition rate for different nitrogen flow rates [55]	26
Figure 16: Residual stress in AlN grown on Pt, Al and Ti as a function of gas flow rates [56].....	26
Figure 17: Piezoelectric coefficient d_{33} of AlN grown on Pt, Al and Ti as a function of gas flow rates [56]	27
Figure 18: Piezoelectric coefficient d_{33} of AlN grown on Pt, Al and Ti as a function of sputtering pressure [56].....	27
Figure 19: Residual stress of AlN grown on Pt, Al and Ti as a function of sputtering pressure [56]	28
Figure 20: Measured residual stress (solid diamond) and stress derived from out-of-plane strain (XRD-open circles) as a function of AlN thin-film thickness [60]	29
Figure 21: Cross section of an AlN film. The left side shows the film grown on (111)-oriented Pt and the right side shows the growth on thermal SiO ₂ [61]	29
Figure 22: Fabricated test structures for resistance measurements.....	31
Figure 23: Top and bottom platinum contact pads for resistance measurements	32
Figure 24: Structural geometry of proposed cantilever design	33
Figure 25: Deflection of the cantilever beam under the influence of 2V	34

Figure 26: Relationship between cantilever bending and applied potential for three different beam lengths.....	35
Figure 27: Deflection of cantilever for different beam lengths	36
Figure 28: Reduction in first modal resonance frequency of the cantilever with increase in beam length	37
Figure 29: First three mode shapes of a 60x6 μ m cantilever under no loading force; (a) f_{res} of first mode is 39879 Hz; (b) f_{res} of second mode is 2.4981e+5 Hz; (c) f_{res} of third mode is 7.0002e+5Hz	38
Figure 30: (a) First mask layer for patterning of bottom platinum layer; (b) Second mask layer for patterning of top platinum layer	41
Figure 31: (a) Third mask layer for patterning of devices on top platinum layer; (b) Fourth mask layer for patterning of contact pads.....	42
Figure 32: Alignment marks	42
Figure 33: Appearance of silver color after Pt layer deposition	43
Figure 34: First mask layer to pattern bottom Platinum layer electrode	44
Figure 35: Appearance of purple color gives an indication of complete etching of top layers and shows that underneath AlN layer has been exposed	45
Figure 36: Second mask layer to pattern top Platinum layer electrode	47
Figure 37: Fitting of plus (+) sign inside the square shows the perfect alignment of second layer with the first layer	47
Figure 38: Third mask layer to pattern devices	49
Figure 39: Photolithography results after development of device layer.....	49
Figure 40: Photolithography results of 5 μ m wide cantilevers after development.....	50
Figure 41: Poor photolithography results for 1 μ m wide cantilevers due to overexposure	50
Figure 42: Making of openings for structure releasing.....	51
Figure 43: Released cantilever after wet etching of oxide layer	52
Figure 44: Cantilever suffering from stiction	52
Figure 45: Processes involved in dry etching and formation of fences due to redeposition of etched material on the side walls	53
Figure 46: Formation of high fence on the edge of platinum layer after dry etching	53
Figure 47: SEM image shows the possible region of failure where top Pt layer step onto the bottom Pt layer	54
Figure 48: SEM image showing fences of bottom Pt layer that are visible on the top Pt layer	55
Figure 49: SEM image showing unwanted material connecting top and bottom platinum layers	55
Figure 50: Formation of fences after etching platinum layer in STS.....	56
Figure 51: Underneath Pt layer has been exposed after unwanted etching of mask layer	57
Figure 52: (a) First mask layer for patterning of top platinum layer; (b) Second mask layer for patterning of bottom platinum layer.....	59
Figure 53: (a) Third mask layer for patterning of SiO ₂ bridges; (b) Fourth mask layer for patterning of contact pads.....	60
Figure 54: Fifth mask layer for patterning of devices on top platinum layer	60
Figure 55: First mask design layer to pattern top Pt layer.....	61
Figure 56: Second mask layer for patterning of bottom Pt layer	62
Figure 57: Third mask layer for patterning of SiO ₂ bridges.....	62
Figure 58: Fabrication of SiO ₂ bridges for electrical insulation between different layers.....	63

Figure 59: Broken SiO ₂ bridges due to over etching of SiO ₂ layer in BHF	63
Figure 60: Illustration of the liftoff process	64
Figure 61: Fourth mask layer for patterning of gold contact pads	65
Figure 62: Photolithography of contact pads for gold deposition.....	65
Figure 63: After 100nm of gold deposition.....	66
Figure 64: Fabrication of gold pads and lines for the electrical connection with the top Pt layer	66
Figure 65: Gold line passing over the oxide bridge.....	67
Figure 66: Fourth mask layer for the patterning of devices	67
Figure 67: Anisotropic etching of silicon using Bosch process.....	68
Figure 68: Cantilever tips are out of focus due to bending downwards	69
Figure 69: SEM image showing etched cavity and released cantilevers and doubly clamped beams	69
Figure 70: SEM image of released devices.....	70
Figure 71: Over etching of silicon from underneath the anchored platform	70
Figure 72: Working principle of Toho Technology FLX 2320-S	71
Figure 73: Simulation of cantilever with material stress in ANSYS Multiphysics.....	72
Figure 74: Fabricated multilayer piezoelectric resonators	73
Figure 75: PCB mounted and wirebonded with the chip for providing voltage signal to the resonators ..	74
Figure 76: Resonance frequency of 60μm long cantilever measured with Laser Vibrometer MSV-400 ...	75
Figure 77: Appearance of cracks on the top platinum layer when voltage was exceeded the threshold limit. SEM image on the right shows the rupturing of layers	76

List of Tables

Table 1: Commercial MEMS based applications [1]	9
Table 2: Piezoelectric Charge Coefficients	20
Table 3: Test wafers deposited with different deposition conditions for AlN film growth.....	30
Table 4: Material properties for FEM	34
Table 5: Simulated results of cantilever deflection for different applied voltages	35
Table 6: Data set for cantilever deflection for different beam lengths.....	36
Table 7: Data set for the first modal resonance and prestressed resonance frequencies for different beam lengths.....	37
Table 8: Optimized deposition rates for SPIDER.....	43
Table 9: SPIDER Deposition parameters for AlN, Pt and SiO ₂ films	43
Table 10: Approx. etch rates of SiO ₂ and Pt for Nexus IBE350	45
Table 11: Optimized deposition rates for SPIDER.....	46
Table 12: Etch rates and etch time of SiO ₂ , Pt and AlN for STS Multiplex	48
Table 13: Etch rates and etch time of SiO ₂ , Pt and AlN for STS Multiplex.....	51
Table 14: Deposition rates and time of different layers for SPIDER	61
Table 15: Parameters for coating of LOR and AZ 1512 in ACS200.....	64
Table 16: Calculated stress values for individual layers and the overall stress measured by Toho Technology FLX 2320-S	72

Chapter 1: Introduction

1.1. Background

MEMS has become a hallmark technology for the 21st century. The advancement in MEMS technology has opened new doors for many emerging applications in the field of smart sensors and actuators. MEMS stands for Micro Electro Mechanical Systems. As the name implies, it refers to the integration of miniaturized electrical and mechanical elements into micro scale system. The critical dimensions of MEMS devices can vary from well below one micron to few millimeters [1]. MEMS technology has potential to revolutionize industrial and consumer products by incorporating Integrated Circuits (IC) batch processing techniques with micromachining processes. It offers the possibility of integration of mechanical, electromechanical, electrochemical and optical components along with the signal processing control circuitry on a single chip to produce smart sensing devices [2]. The basic components of MEMS smart system consist of mechanical microstructures, microsensors, microactuators and microelectronics as shown in Figure 1. Microsensors and microactuators are categorized as transducers that convert energy from one form to another. Microsensors are used to detect any change such as pressure, thermal, chemical or electromagnetic, in the physical environment of the system and convert it into a readable electrical signal. The electrical signal can be a change in voltage, current or resistance, etc. Microelectronics makes a decision on the basis of information provided by the sensing element and signal the microactuators to react and perform mechanical motion in order to bring some specific changes in the physical environment of the system [3].

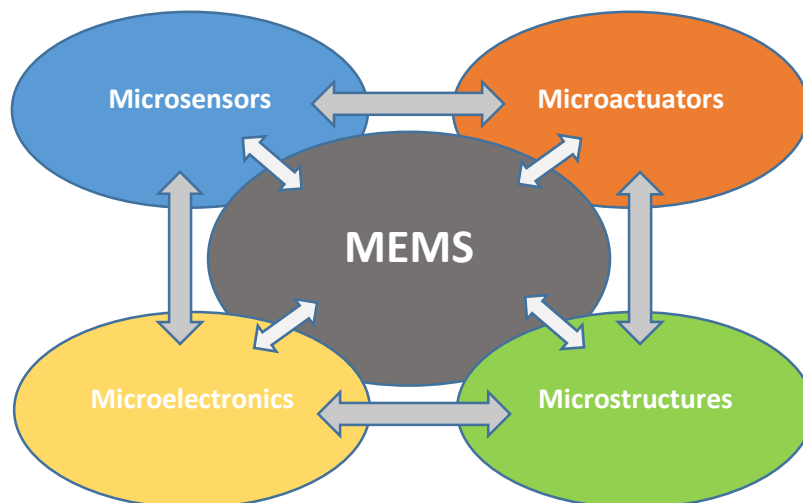


Figure 1: Components of MEMS smart system

The research on MEMS started in early 1960s but it took 20 to 30 years for the first MEMS device to be commercially available. Micromachined nozzles for inkjet printers and accelerometers for

airbag system were first few commercial applications of MEMS devices. In 1980s, the advancement in MEMS technology has seen a very rapid growth due to the introduction of new microfabrication processes derived from well-established semiconductor Integrated Circuit (IC) manufacturing. These processes include lithography, thin film deposition and different wet and dry etching techniques. There are many mature MEMS devices available in the market, which are incorporated into bigger systems to provide commodities for our daily life [4].

In the today's world, the technological boom of the Internet of Things is entirely dependent on accurate and reliable sensors for data gathering. In such an industry, the need for miniaturization is essential and the demand for smart microsystems is ever growing. MEMS devices have huge impact on microsystems industry due to their small size, high reliability and low cost [5]. MEMS devices can be used in various technological fields including telecommunication, data storage, medical, automotive and environmental monitoring. Table 1 shows some of the commercial applications of MEMS devices.

Table 1: Commercial MEMS based applications [1]

Applications	Examples
Sensors	Pressure sensor, bio-metric sensor, IR sensor, motion sensor
Resonators	Inertial sensor, gyroscope, accelerometer
Actuators	Motor, drive
Audio	MEMS Microphone
Printer	3D printer, ink-jet printer using piezoelectric and thermal bubble ejection
Bio-MEMS	Fluid acceleration for micro-cooling, lab on chip, μ -TAS (biosensor etc)
Micropump	Electroactive polymer, active microfluidic handling or analysis
Optics	Optical switches for data communication, MEMS micro-mirrors
Energy Harvest	Micro power generators based on piezoelectric, electrostatics and electromagnetics
Display	Projection display, reflective display, tactile display

In 1959, the physicist Richard Feynman gave a visionary talk in an American Physical Society meeting at Caltech entitled as "There's Plenty of Room at the Bottom" [6]. This talk was about the direct manipulation and arrangement of atoms by the help of nanoscale machines. At that moment, it did not get enough attention but later his ideas laid the foundation of nanotechnology. Nanotechnology is a field of science that deals with the inspection and manipulation of individual atoms and molecules with the dimension of 1 to 100 nanometers [7]. The ideas floated by Richard Feynman decades ago, are now transformed into well-established fields of technology such as electron and ion beam fabrication, molecular beam epitaxy, nanoimprint lithography, atom-by-atom manipulation and micro/nanoelectromechanical systems (M/NEMS) [8].

NEMS is one step ahead of MEMS in terms of miniaturization, device efficiency and low cost. The devices such as resonance mass sensors are greatly affected by the dimensions of the mechanical sensing element. The sensitivity and the quality factor can be improved by scaling down the dimensions and mass of the sensor [9][10].

1.2. MEMS/NEMS Resonator

Resonator is a mechanical structure which vibrates at a particular frequency with relatively greater amplitude. This particular frequency is called the resonance or natural frequency of the system. MEMS resonators are miniaturized devices having resonating mechanical elements such as cantilever, double clamped beam or a membrane that oscillates at resonance frequency upon excitation. Excitation stimulus can be voltage, current or force. MEMS resonators have found their way in consumer industry as a part of different sensing devices such as mass, pressure and gas sensors. The readout parameter for a resonance sensor can be changed in resonance frequency, quality factor, vibration amplitude and phase which are directly affected by the axial forces, added mass, change in damping, material properties and magnitude of driving force. Figure 2 summarizes different types of parameters that can be detected by a MEMS resonant sensor and its corresponding output [11].

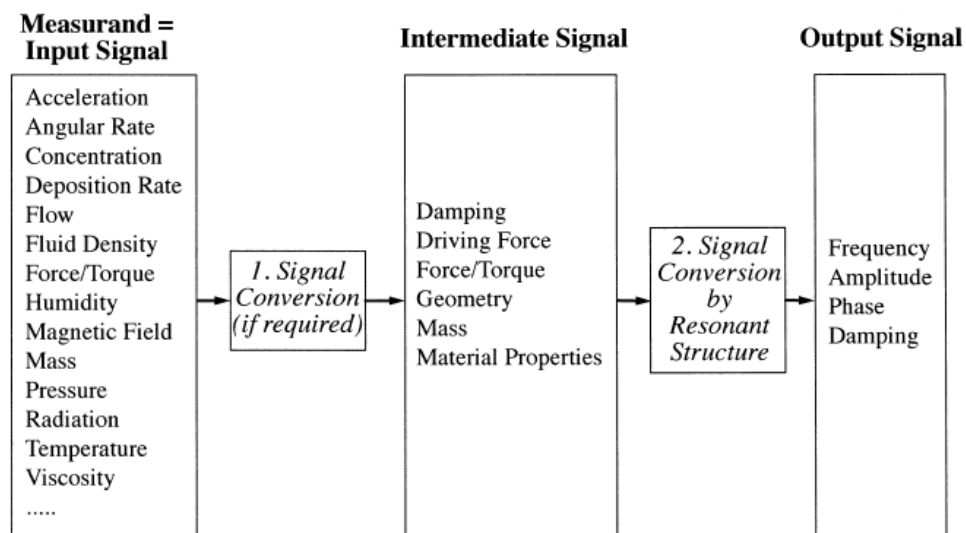


Figure 2: Application areas of MEMS resonators

1.3. Microcantilever Beam Resonator

Microcantilever is a most common type of MEMS resonator. Cantilever is a mechanical beam which is anchored at one end and free to move at the other end. Over the past few years, microcantilevers have gain a lot of attention due to high sensitivity in different sensing applications. Pressure sensor, chemical sensor and mass sensor are few examples where the

magnitude of beam deflection or change in resonant frequency of the beam is used to measure the change in the physical environment of the device depending upon the mode of operation [12].

1.3.1. Modes of Operation

Sensors based on microcantilevers can be operated in dynamic mode or static mode. In dynamic mode of operation, the change in resonance frequency of the beam is measured. Microcantilever based mass sensors can be operated in dynamic mode where the change in resonance frequency gives the measure of mass absorbed on the surface of the cantilever as shown in Figure 3A. In dynamic mode, the cantilever is excited close to its resonance frequency. When the additional mass is attached to the surface of cantilever it shifts the resonance frequency. Frequency of the cantilever reduces as the amount of absorbed mass increases. The change in resonance frequency Δf_{res} due to absorbed mass Δm is given by equation 1 [13][14].

$$\Delta f_{res} \approx -f_0 \frac{\Delta m}{2m_0} \quad (1)$$

where f_0 is the natural frequency and m_0 is the initial mass of the cantilever.

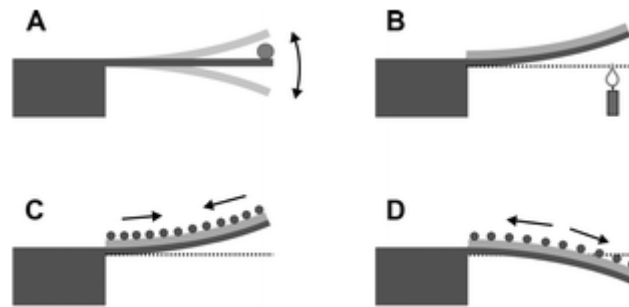


Figure 3: Cantilever sensor modes of operation: (A) dynamic mode detecting mass changes on the cantilever by changes in resonance frequency; (B) bimetallic mode detecting temperature changes by a static bending due to different thermal expansion of the metal layer and silicon cantilever; (C) static mode where asymmetrical molecule absorption cause tensile stress, results in bending the cantilever upwards; (D) static mode where asymmetrical molecule absorption cause compressive stress, results in bending the cantilever downwards [15]

In static mode of operation, bending of the cantilever is continuously monitored for the detection of any change in the external measurands. Deflection of the cantilever beam can be caused by the variation in surface stress, pressure or temperature. Most of the bio-sensors operate in fluid environment where the dynamic mode of operation cannot be used because quality factor is drastically reduced due to the viscous damping of the fluid [16]. So sensing is done by using beam deflection. One side of the cantilever is coated with monolayer of bio-receptors in order to attach selective molecules from the fluid whereas the other side is kept inert. This creates an

asymmetrical stress on the surface which deflects the cantilever [17]. Depending on the type of stress generated, the cantilever beam will bend upwards or downwards. In case of compressive stress, the cantilever bends downwards whereas it bends upwards for tensile stress as shown in Figure 3C and 3D. The magnitude of beam deflection gives the amount of change in surface stress which gives an indication regarding the amount of molecules attached on the surface. Stoney's formula is one of the most commonly used equation that relates beam deflection with the change in surface stress and the beam dimensions as shown in equation 2 [15].

$$\Delta\sigma = \frac{Et^2}{3(1-\nu)L^2}\Delta z \quad (2)$$

Where $\Delta\sigma$ is the change in surface stress between top and bottom surface of the cantilever, Δz is the cantilever deflection, E is Young's modulus, ν is Poisson ratio and L and t are the length and the thickness of the beam respectively.

1.3.2. Commonly used methods of resonator excitation and detection principles

Resonant sensor not only consists of a mechanical resonating part but it also needs an excitation source that forces the mechanical part to vibrate and a detector element to detect these vibrations. Figure 4 shows the basic components of a resonant sensor, which consists of a mechanical part, excitation source, detector and feedback control circuitry. The purpose of feedback circuitry is to ensure that resonator maintain the desired resonance mode even when the resonance frequency changes as the result of change in the measurand [18].

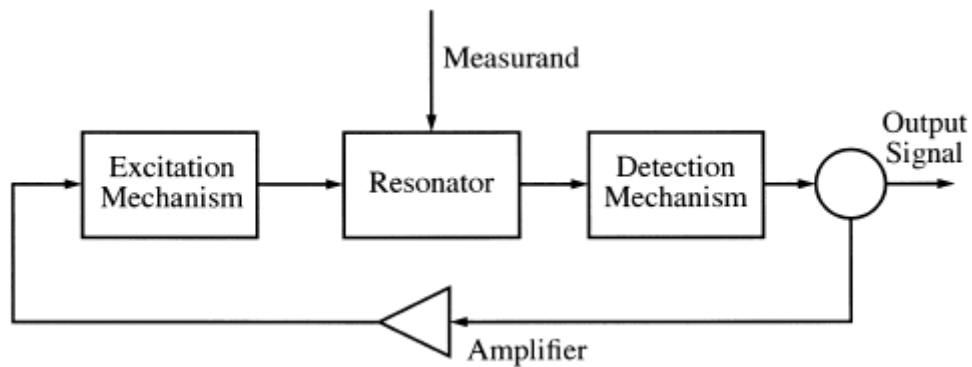


Figure 4: Block diagram of a resonant sensor

There are six most commonly used excitation techniques along with their corresponding detection methods in order to investigate vibrations of a resonator structure.

- a. Electrostatic excitation and capacitive detection: This technique requires two electrodes place very close to each other to make a parallel plat capacitor where one electrode is the part of cantilever beam as shown in Figure 5(a). The two electrodes are separated by an air gap. When an alternating voltage is applied to the electrodes, the generated

electrostatic force will have a pulling effect resulting in the deflection of the cantilever beam. The detection technique also makes use of the same electrodes. The vibration of the beam changes the distance between the electrodes resulting in the change in capacitance that can be used to detect vibration of the beam. This excitation technique is very effective where resonator oscillates in vacuum in order to avoid air damping [19].

- b. Dielectric excitation and capacitive detection: This technique is very similar to the above mentioned technique except that a very thin layer of dielectric layer is sandwiched between two electrodes where one electrode is the part of the cantilever beam as shown in Figure 5(b). AC voltage creates electrostatic force which laterally deforms the dielectric thin film. This deformation generates a bending moment in the beam. Vibrations cause the area between the plates to change resulting in change in capacitance, which is used to detect beam vibration [20].
- c. Piezoelectric excitation and detection: This technique makes use of a piezoelectric material such as ZnO or AlN for excitation and detection of beam vibrations. When voltage is applied across piezoelectric material, it undergoes physical deformation which is used to excite resonators. The top surface of the beam is deposited with a pair of electrodes where piezoelectric material is sandwiched in between as shown in Figure 5(c). When an AC voltage is applied to the electrodes then stress is generated in the piezoelectric layer resulting in bending of the cantilever. The reverse piezoelectricity can be used for detection of beam vibration. Vibrating beam cause physical deformation of the piezoelectric layer that generates electric field across it and by measuring this electric field, the magnitude of vibration can be measured [21].
- d. Resistive heating excitation and piezoresistive excitation: In this technique, excitation is done using heat pulses. Properly selected part of the cantilever is exposed to the heat pulses which generates local expansion of material resulting in beam deflection. The local expansion of the material is achieved by heating up the integrated diffused resistor or polysilicon resistor as shown in Figure 5(d). The detection mechanism also makes use of the same polysilicon resistor to detect vibrations of the cantilever. Polysilicon is a very good piezoresistive material. Resistivity of a piezoresistive material changes as a material undergoes physical deformation. Deflection of the beam forces the integrated piezoresistor to deform physically resulting in the resistance change and when this piezoresistor is connected with the voltage source then change in resistance changes the voltage drop across the piezoresistor that can be used to detect beam vibration [22].

- e. Optical heating and detection: This technique requires a laser source for excitation and an optical detector for detection. The surface of resonator is exposed with periodically activated laser beam and the light absorbed from the laser beam is used to generate thermal stress needed for the excitation of the cantilever beam as shown in Figure 5(e). An optical arrangement is used for the detection of vibrations. There are two different optical detection techniques; interferometric and amplitude modulation. Interferometric detection use interference fringe pattern to detect and measure the magnitude of beam displacement. Optical detection in general is the most commonly used detection technique because it doesn't require any extra arrangement integrated on the resonator beam [23].
- f. Magnetic excitation and detection: Magnetic excitation is easily achieved by Lorentz force due to the interaction of surrounding magnetic field with the electric current passing through the resonating structure as shown in Figure 5(f). The magnetic detection uses reverse principle of magnetic excitation where the vibrating beam (conductor) in the presence of magnetic field generate induced voltage. Normally H shaped resonators are used for this technique where one beam is responsible for excitation and other for detection [24].

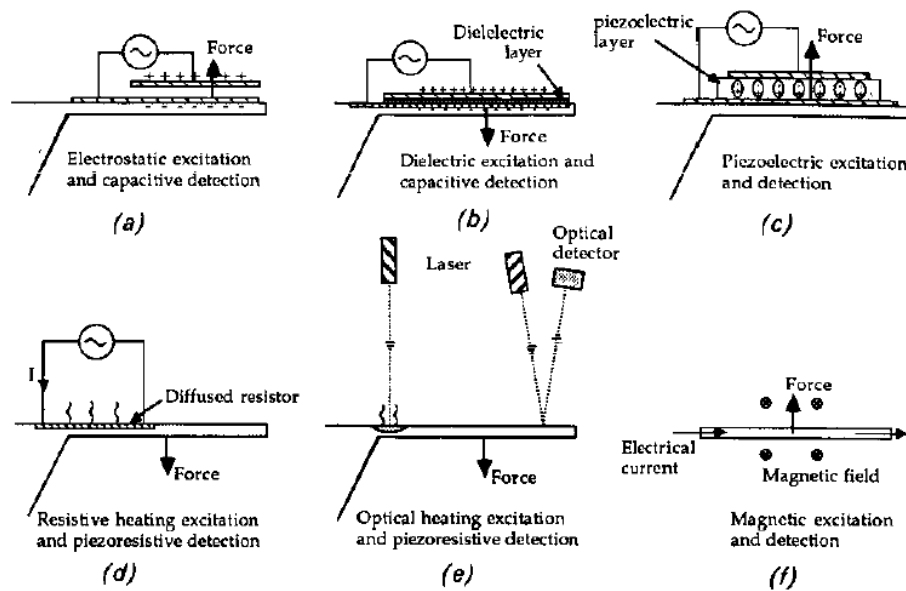


Figure 5: Different excitation and detection techniques for microcantilever resonators [18]

1.3.3. Applications of Microcantilever Resonators

Resonators are used today in most of the MEMS devices such as inertial sensors, bio sensors, chemical sensors, pressure sensors and energy harvesters. Cantilever is one of the simplest and commonly used resonator structure. Below are a few application areas of MEMS resonators.

1.3.3.1. Mass sensor

Microcantilever based mass sensors are used to detect minimal changes in mass attached to the surface of the cantilever. Due to the simple geometry of cantilevers, extreme miniaturization and enhanced mass sensitivity can be achieved. MEMS mass sensors have the capability to detect mass changes even below picogram level [25]. The detection is based on the change in resonance frequency or stress induced bending. In static mode, sensing is done due to the change in surface stress generated as the mass is attached on the surface of the cantilever whereas sensing in dynamic mode depends on the change in resonance frequency [26]. Dynamic mode of operation for mass sensing is more preferable due to sensitivity and long term stability. By using the same principle, there are many different applications where MEMS mass sensors can be used to investigate different types of molecules or gases present in the surrounding environment [27].

1.3.3.2. Chemical Sensor

Chemical sensors have found many applications in environmental monitoring for the detection and quantification of potentially dangerous gasses [28] and in biomedical applications [29]. Current methods for the detection of chemical contamination are gas/liquid chromatography and mass spectroscopy, which are relatively expensive and time consuming. On the other hand, MEMS chemical sensors are cheaper, faster and can be integrated with wireless communication circuitry for rapid response. The basic components of a MEMS chemical sensor consist of a sensitive layer which binds with molecules of interest from the surrounding environment as shown in Figure 6. This sensitive layer can be a polymer for chemical sensing and antibodies for bio-chemical sensing. It is very important that sensitive layer should have very high affinity for the molecules of interest and very low affinity for other substances. The second main component of a MEMS chemical sensor is a transducer that detects the binding of molecules with the sensitive layer and convert it into a readable signal that can be processed by signal processing unit and later can be used by other devices in the system [30].

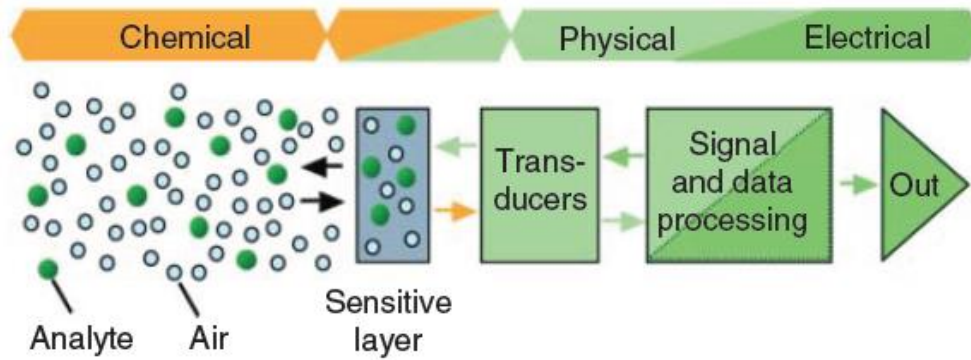


Figure 6: Basic components of a chemical sensor

Figure 7 shows a silicon based microcantilever where mesoporous silica sensing layer is deposited at the tip for TNT vapor detection [31].

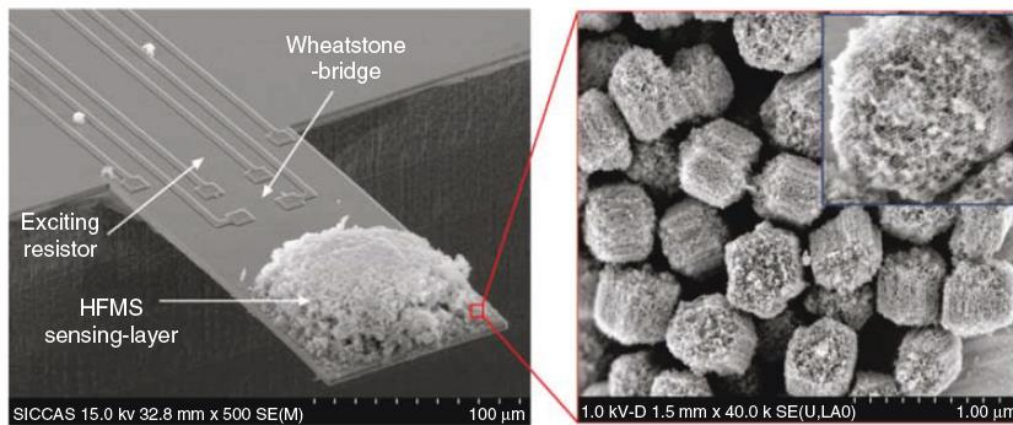


Figure 7: SEM image of silicon-based resonant cantilever with hexafluoro-2-propanol functionalized mesoporous silica sensing film [31]

1.3.3.3. Biosensor

MEMS based biosensors are used for the detection and quantification of different biological organism such as cells, proteins, viruses and nucleic acids. These are highly sensitive and label free devices capable of monitoring growth rate of individual bacteria, weighting single cell and biomolecule, protein immobilization and detection of pathogens and parasites in food matrices and water sources [32].

Biosensor based on resonating mechanical structure such as cantilever is the most commonly employed technique due to high mass sensitivity and miniaturized design [33]. In order to detect cells, viruses, pathogens and other biomolecules, it is essential to do the biological functionalization of the cantilever surface with recognition molecules called bio-recognition agents. These special molecules should have very high affinity and selectivity for target biological

molecules and very low affinity for other substances. Functionalization of sensor surface consists generally of a three step process [34].

- i. *Preparation*: First the cantilever surface needs to be prepared for the immobilization of bio-recognition agent. This is achieved by the chemical modification of cantilever surface in order to create a reactive layer, which is used to hold bio-recognition molecules.
- ii. *Immobilization*: Second the immobilization of bio-recognition molecules needs to bind specific target molecules.
- iii. *Passivation*: Thirdly, bare reactive parts on the cantilever surface need to be passivated for preventing unwanted absorption of molecules which could lead to potentially false sensor response.

Biosensors are operated in static and dynamic mode. In static mode, analyte binding with the surface causes the bending of cantilever beam whereas, in dynamic mode, the resonance frequency of the cantilever is changed due to the binding of target molecules [35]. Microcantilevers are available in single layer and multilayer geometry. Multilayer geometry consists of an active layer (PZT, AlN) for self-actuation and electrodes for providing excitation. Multilayer geometry does not require additional hardware for actuation and detection. Such devices are suitable for remote or field measurements [36]. Figure 8 shows PZT based self-sensing cantilever where tip of the cantilever is coated with bio-receptors for analyte binding.

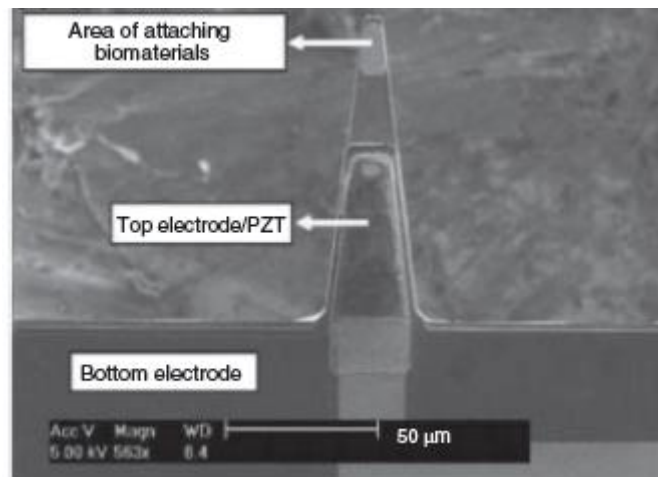


Figure 8: PZT based self-sensing microcantilever [36]

1.3.3.4. Pressure Sensor

MEMS pressure sensor is among the very few early MEMS devices that uses a suspended membrane or a resonating structure such as cantilever for pressure measurements. The variation of air pressure causes the bending of membrane and cantilever which is detected by using different detection mechanism. The most commonly used detection techniques include piezoelectric, piezoresistive and optical detection techniques [37]. Microcantilevers as resonating

structures have been the focus of studies for many years. Microcantilever sensors can be used to detect the variation of surrounding pressure due to the change in resonance frequency or change in damping conditions [38]. In changing pressure environment, a vibrating cantilever beam behaves like a damped oscillator where the damping is the function of surrounding pressure [39]. The damping is caused by the interaction of surrounding gas or fluid molecules with the cantilever surface which leads to the dissipation and eventually the resonance frequency and the Q factor of the cantilever is degraded. By detecting this change in resonance frequency and quality factor the surrounding pressure can be measured [40].

Chapter 2: Multilayer Piezoelectric NEMS Resonator

2.1. Piezoelectricity

Piezoelectricity defines the ability of certain materials to develop electric charge in response to the applied mechanical stress. Piezoelectricity provides a transduction mechanism to convert electrical energy into mechanical motion. One of the unique property of piezoelectric materials is to have converse effect. Converse piezoelectric effect is generation of strain in response to applied electric field.

The piezoelectric effect is generated due to the occurrence of dipole moment in crystals. Crystals of piezoelectric material (quartz, PZT, AlN etc.) are electrically neutral under no external force. These crystals don't have to be symmetrical but the atoms are arranged in such a way that positive charges in one place cancel the effect of negative charges in the nearby place. When piezoelectric material is squeezed or stretched or it comes under the influence of any type of physical force, the structure gets deformed which leads to the unbalance between positive and negative charges causing electrical charge to appear. Similarly, when an external electrical field is applied, strain is induced in the crystals and atoms have to rearrange themselves in order to release this strain resulting in physical deformation [41].

2.1.1. Piezoelectric Coefficients

Piezoelectric coefficients create a link between electrical stimulus and mechanical response or vice versa. They are used to quantify the volume change when electric field is applied on piezoelectric material or it gives an indication of direction of polarization of piezoelectric material when it is subject to external stress. Each coefficient, as a second-rank tensor, is described by its two subscripts. First subscript represents the direction of polarization whereas the second subscript represents the direction of induced stress. By convention, direction along X, Y and Z is represented by subscript 1, 2 and 3 respectively and shear about axis X, Y and Z is represented by the subscript 4, 5, or 6 respectively as shown in Figure 9.

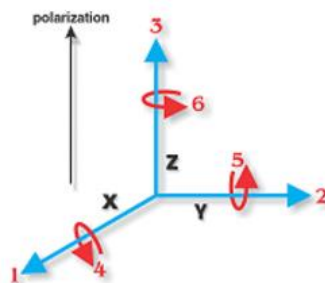


Figure 9: Direction of forces affecting a piezoelectric element

There are different types of piezoelectric coefficients such as piezoelectric voltage coefficient (g_{33}, g_{31}, g_{15}), dielectric constant ($\epsilon_{11}^T, \epsilon_{33}^S$), elastic compliance (s_{11}^E, s_{33}^D) and electromechanical coupling factor (k_{33}, k_t, k_{31}, k_p) but for the scope of this report the piezoelectric charge coefficients (d_{33}, d_{31}, d_{15}) will be further discussed.

2.1.2. Piezoelectric Charge Coefficients

Piezoelectric charge coefficients are also called d constants that relate mechanical strain induced in the material to the applied electric field. The constant's units are expressed in meters per Volts (equation 3). Table 2 gives a brief description about the different piezoelectric charge coefficients.

$$d = \frac{\text{Strain development}}{\text{Applied electric field}} \quad (3)$$

Table 2: Piezoelectric charge coefficients

d constants	Description
d_{33}	Induced polarization along z-axis per unit stress applied along z-axis or Induced strain in the direction of z-axis per unit electric field applied in the direction of z-axis.
d_{31}	Induced polarization along z-axis per unit stress applied along x-axis or Induced strain in the direction of x-axis per unit electric field applied in the direction of z-axis.
d_{15}	Induced polarization along x-axis per unit shear stress applied along y-axis or Induced shear strain in the direction of y-axis per unit electric field applied in the direction of x-axis.

2.2. Proposed design of Multilayer Piezoelectric Resonator

Multilayer piezoelectric cantilevers are self-actuating and self-sustaining resonators that do not require any external excitation mechanism. Multilayer stack consists of active layers which are responsible for actuation and passive layers dedicated for bonding or voltage biasing of active layers. Such devices are also refer as multimorphs depending on the number of active layers involved in actuation. Multilayer resonators are particularly popular as actuators in many MEMS devices such as accelerometers, atomic force microscopy, micro-robots and energy harvesters.

In this report our main focus will be on unimorph cantilevers where only one active layer is responsible for actuation. Aluminum nitride (AlN) is used as an active layer due to its good piezoelectric properties and platinum is used as passive layer. In the proposed design, a multilayer cantilever consists of 50nm ultra-thin layer of aluminum nitride, which is sandwiched

between two 25nm ultra-thin layers of platinum as shown in Figure 10. It has been experimentally proven that the presence of seed layer under bottom platinum layer helps the columnar growth of aluminum nitride active layer with enhanced piezoelectric coefficients [42].

Platinum layers act as electrodes which are used to apply voltage across piezoelectric layer (AlN). Presence of voltage generates an electric field that causes thin film to undergo physical deformation. The seed layer offset the neutral axis of the multilayer cantilever from the central plane of active layer. As a result the longitudinal strain generated in piezoelectric layer due to the inverse piezoelectric effect creates a transverse moment in the cantilever and forces the beam to deflect [43][44]. Equation 4 shows a direct relationship between the strain induced in the beam and the applied electric field.

$$\varepsilon = d_{31}E_z \quad (4)$$

where

ε is the piezoelectric longitudinal strain, d_{31} is the piezoelectric coefficient and E_z is the vertical component of electric field

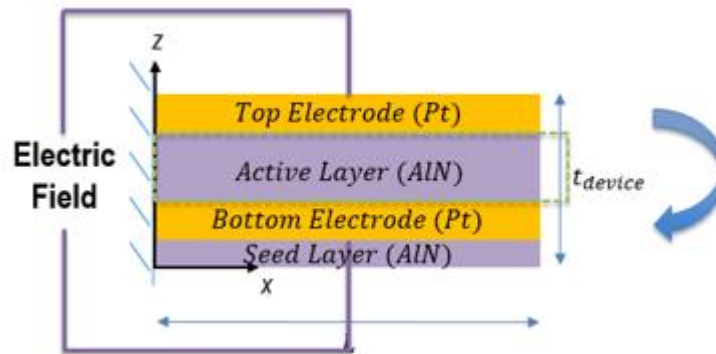


Figure 10: Block diagram of Multilayer Piezoelectric Resonator

2.3. Aluminum nitride material characterization

Aluminum nitride is commonly used in surface micromachined resonators where ultra-thin piezoelectric layer of few microns is required [45]. AlN grows in the wurtzite structure preferentially with c-axis orientation which is desirable for good piezoelectric properties. In order to achieve high piezoelectric coupling and low losses, it is essential that AlN grows in the form of vertical columnar grains perpendicular to the substrate surface [46]. The orientation of AlN grains highly depends on the deposition technique, deposition conditions and on the substrate. C-axis preferentially orientated AlN thin films can be synthesized by different deposition techniques such as chemical vapor deposition (CVD), molecular beam epitaxy, ion beam deposition, pulsed laser ablation deposition and reactive RF magnetron sputtering. However reactive magnetron

sputtering is the most favorable choice for deposition of AlN films due to reproducibility, low cost and low deposition temperature requirement (300-450 °C) which also makes it compatible with Integrated Circuit (IC) fabrication [47].

2.3.1. DC Pulsed reactive magnetron sputtering for AlN thin films

Reactive sputtering is a physical vapor deposition (PVD) process for deposition of thin films by sputtering the material from target and depositing it on the substrate. Sputtering of target material is done by the bombardment of high energy ions or atoms of some gas especially inert gas such as argon. Some additional gases are also introduced in the chamber along with argon which chemically react with the material sputtered from the target either to achieve certain doping or deposit a thin film of new chemical compound on the substrate as shown in Figure 11 [48].

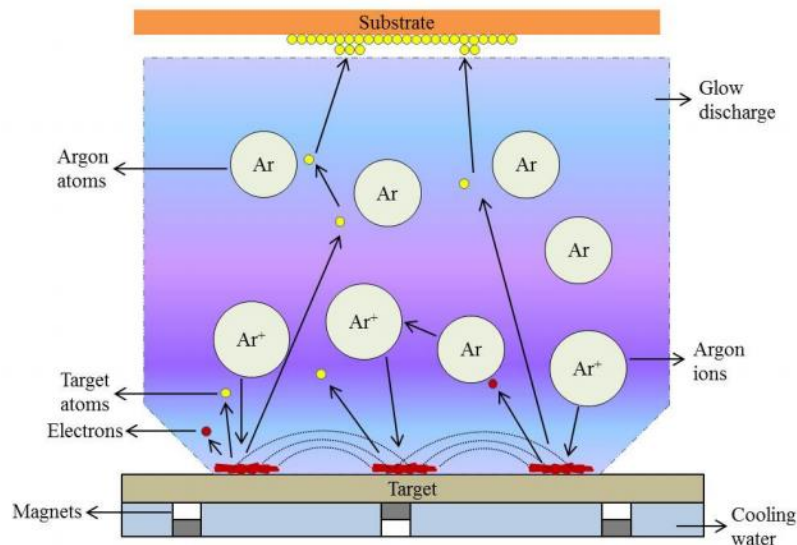


Figure 11: Schematic diagram illustrating the basic components of a magnetron sputtering system [49]

DC pulsed reactive magnetron sputtering is used to achieve well-textured AlN thin films by sputtering the aluminum target with the mixture of high energy argon and nitrogen ions. The ratio of argon and nitrogen introduced in the chamber, pressure, power, temperature and substrate potential highly affects the growth quality AlN crystals. 99.999% pure aluminum disk is used as a target. Aluminum sputtered due to heavy bombardment of argon ions undergoes a chemical reaction with the ionized nitrogen present in the plasma under high temperature in order to generate polycrystalline AlN thin film on the substrate [50][51].

Magnetron sources are widely used for high deposition rates and lower operating voltage where plasma is maintained by either RF or DC power. In magnetron sputtering system, strong magnetic

field is generated near the target area which causes the electrons to spiral along the magnetic flux line near the target. This arrangement is used to confine plasma in front of the target area in order to intensify the bombardment of ions. As a result, a highly dense plasma is achieved [49]. Pure DC approach for sputtering of dielectric material is not possible due to charging of the target. Charge buildup on insulator target hinders the flow of incoming argon ions and eventually terminates the glow discharge. In order to tackle this problem, DC pulsed sputtering is used for the sputtering of dielectrics to prevent arc formation by neutralizing the surface charge [52]. In the normal mode of operation, a positive (reverse) voltage pulse is applied after every sputtering pulse. The positive pulse tends to discharge the charge buildup on the insulator target surface by attracting electrons to neutralize the positive charge and prevent the occurrence of arc formation as shown in Figure 12.

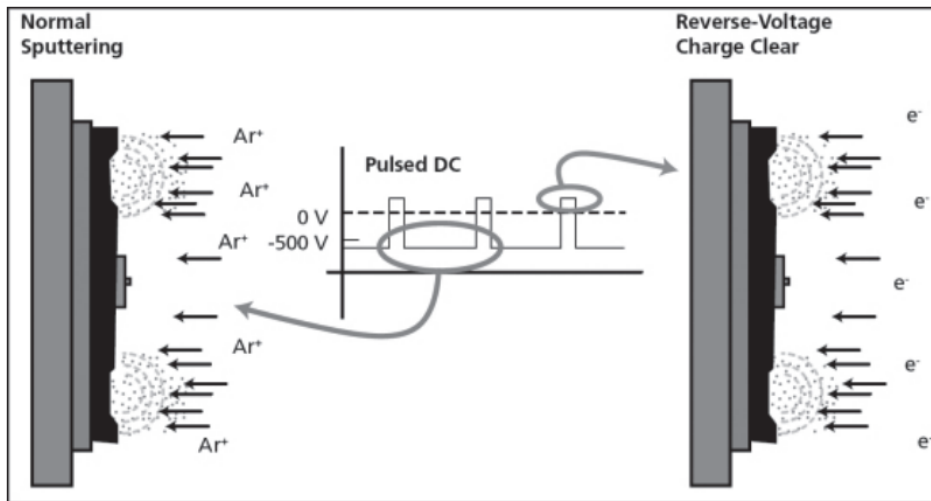


Figure 12: Basic mechanism of Pulsed DC magnetron sputtering. Positive pulse reverse the potential on the target and attracts electrons in order to neutralize the positive charge buildup on the insulator surface [52]

2.3.2. Effect of deposition conditions on AlN growth

Properties of AlN film related to crystal structure, orientation and chemical composition are greatly dependent on the deposition conditions. DC pulsed magnetron sputtering is used for AlN thin film growth and the deposition parameters such as substrate temperature, pressure, argon/nitrogen gas ratio and film thickness are very critical in achieving low stress and high piezoelectric coefficients in AlN thin films.

2.3.2.1. Substrate Temperature

Rate of deposition of AlN thin film is dependent on the substrate temperature. As the substrate temperature increases, the density of ions and gases present close to substrate reduces. As a result, the sputtered aluminum atoms are less likely to be scattered due to collisions with other atoms and ions present in the plasma. Due to reduce scattering, most of the sputtered Al atoms arrive at the substrate and contribute in increasing the deposition rate. However, reduction in density of gases and ions also reduces the number of nitrogen ions that fall on the substrate surface to react with the Al to form AlN. Hence in the beginning, the deposition rate increases as the substrate temperature increases until it reaches a threshold limit and then deposition rate starts reducing with the increase in temperature as shown in Figure 13.

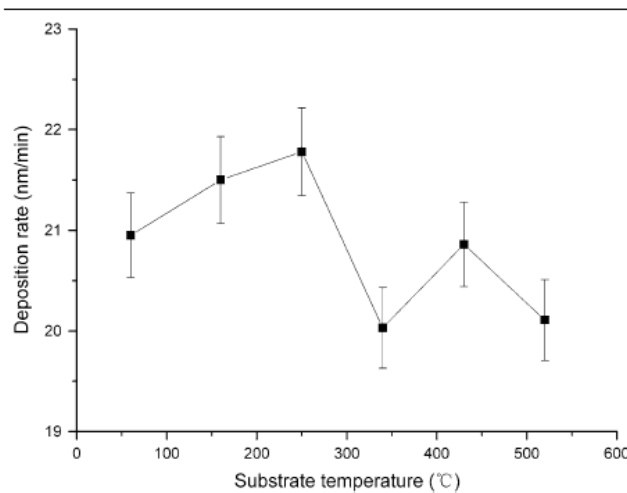


Figure 13: Rate of deposition of AlN film as function of substrate temperature [53]

Quality of AlN crystals increases with the increase of substrate temperature [54]. Best results are achieved at high temperatures. Structure of AlN grown at different temperatures is shown in Figure 14. AlN deposited at high temperature has very a uniform columnar structure and intensity of grain boundary is relatively low as compared with the AlN deposited at lower temperature.

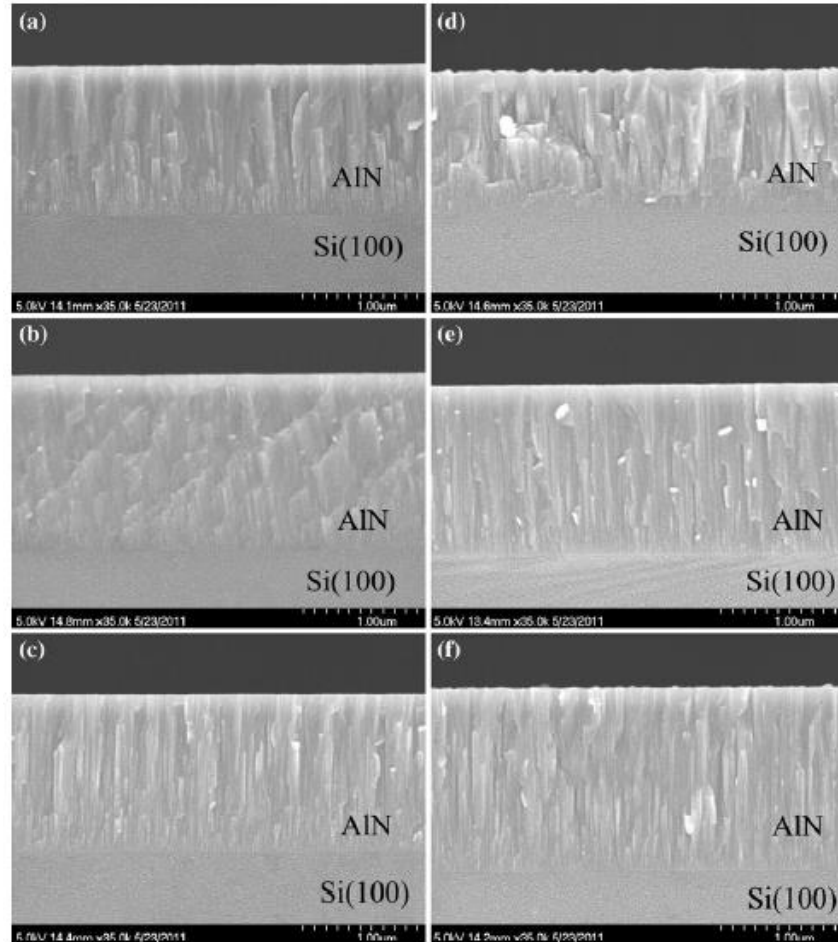


Figure 14: SEM cross-sectional view of AlN thin films deposited at different substrate temperatures of (a) 60 °C (b) 160 °C (c) 250 °C (d) 340 °C (e) 430 °C (f) 520 °C [53]

2.3.2.2. Argon/Nitrogen flow rates

Rate of deposition of AlN film is also dependent on the flow rates of argon and nitrogen gases introduced in the chamber. Argon ions bombard the target surface and sputter target material which later react with nitrogen ions to form AlN film on the substrate. In reality both nitrogen and argon ions bombard the target surface but atomic mass of argon is much higher than nitrogen so the maximum momentum is transferred by the argon ions and argon ions have maximum contribution in sputtering the target material [55]. So as the flow rate of nitrogen is increased, rate of deposition is reduced mainly due to the low momentum transfer by nitrogen ions as compared with argon ion and consequently the energy of sputtered atoms reduces which leads to the gradual fall in the growth rate of AlN film as shown in Figure 15.

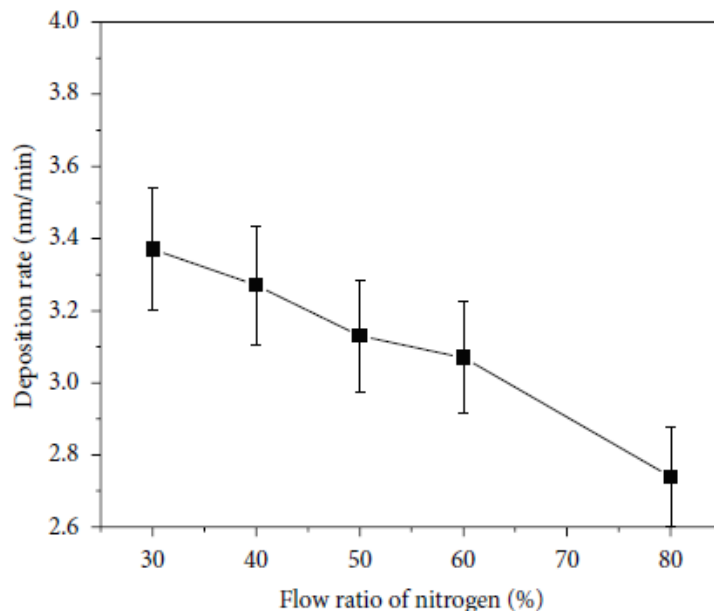


Figure 15: AlN film deposition rate for different nitrogen flow rates [55]

Figure 16 & Figure 17 show the effect of Ar/N₂ flow rates on the residual stress and the piezoelectric coefficient d_{33} in the AlN film grown on three different metals. A steep transition from compressive to tensile stress is obtained by varying the Ar/N₂ flow rates. When the ratio of $\frac{1}{4}$ is maintained the stress in the film is close to zero. Similarly, the highest piezoelectric coefficient is achieved for platinum when the same $\frac{1}{4}$ ratio is maintained.

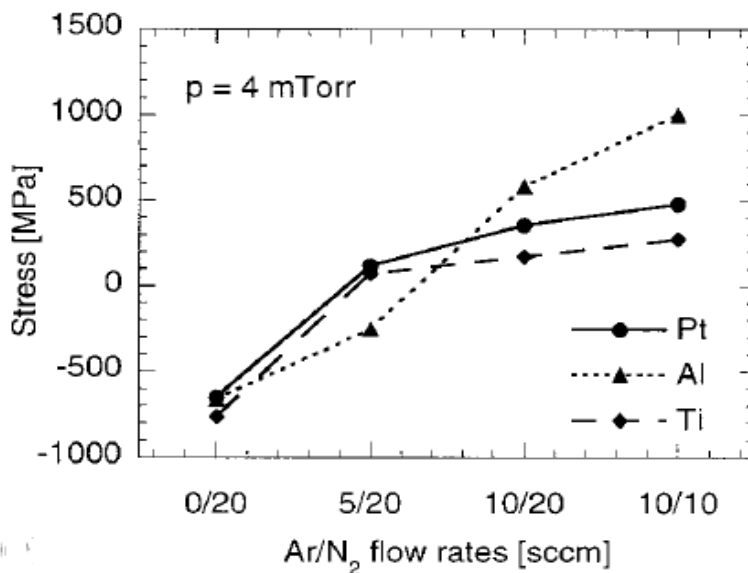


Figure 16: Residual stress in AlN grown on Pt, Al and Ti as a function of gas flow rates [56]

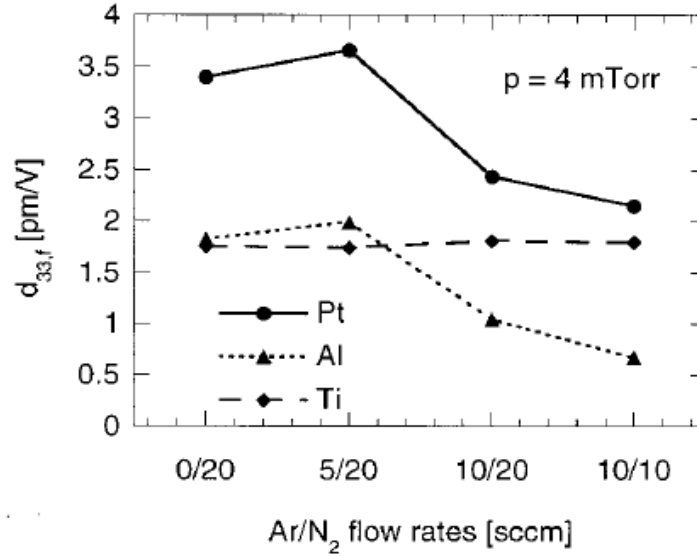


Figure 17: Piezoelectric coefficient d_{33} of AlN grown on Pt, Al and Ti as a function of gas flow rates [56]

2.3.2.3. Sputtering Pressure

Sputtering pressure is another important parameter that is used to control the preferred orientation of AlN film [57], minimize residual stress and enhance piezoelectric coefficient [58]. Reduction in pressure, reduces the rate of deposition of AlN film due to the small quantity of ionizable atoms and molecules but it increases the directionality of sputtered atoms and helps in growth of an AlN film with enhanced piezoelectric properties. Figure 18 shows piezoelectric coefficient d_{33} as a function of sputtering pressure for a fix Ar/N₂ flow rate. The piezoelectric coefficient d_{33} gradually increases when the sputtering pressure reduces due to the increased mobility of adatoms induced by the higher bombardment energy.

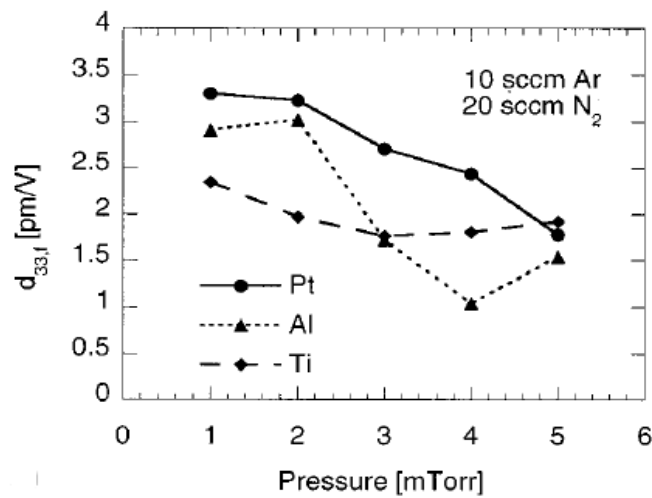


Figure 18: Piezoelectric coefficient d_{33} of AlN grown on Pt, Al and Ti as a function of sputtering pressure [56]

Figure 19 shows the effect of sputtering pressure on the residual stress generated in the AlN film. A steep transition from tensile to compressive stress is observed with the increase in pressure due to the bombardment of growing layer with the high energy plasma species. Bombardment energy depends on the collisions among atoms and ions before they reach the substrate. At low pressure, accelerated ions suffer few collisions in the plasma and their interaction with substrate surface is almost perpendicular. Due to the high directionality of ionic bombardment, higher residual stress is generated [59]. Sputtering pressure should be controlled very carefully in order to achieve low stress and high piezoelectric response. The energy of the ions should be high enough to grow well-textured AlN film but not too high that the bombardment deteriorates the crystal quality.

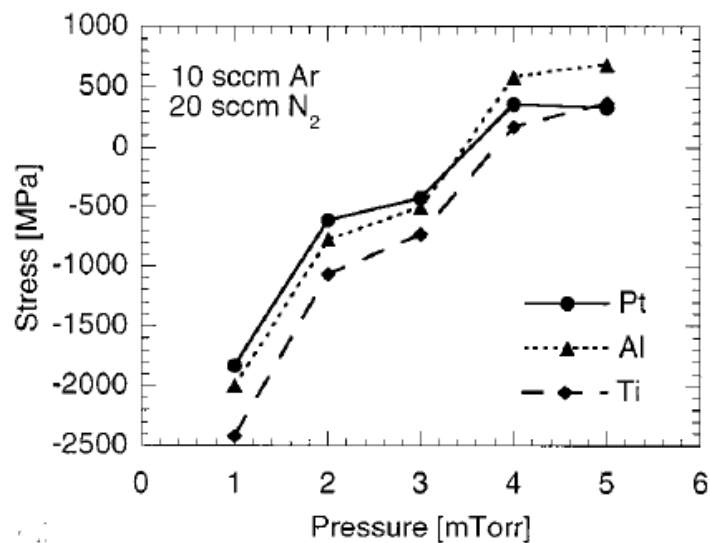


Figure 19: Residual stress of AlN grown on Pt, Al and Ti as a function of sputtering pressure [56]

2.3.3. Platinum electrode layer for AlN thin film growth

Quality of AlN film is greatly influenced by the nature of the electrode material. Among other metals (Al, Ti etc.) platinum gives the best results in term of low residual stress and high piezoelectric coefficient as shown in Figures 16, 17, 18 & 19. Platinum with (111) orientation is favorable for the growth of (0002) oriented AlN film. AlN is deposited on top of the platinum which serves as the bottom electrode. Bottom platinum electrode not only helps to grow well textured c-oriented AlN films but it is also used to apply voltage across piezoelectric (AlN) layer. For thick AlN films, the residual stress contribution from platinum electrode is only dependent on the deposition conditions rather than the material itself [60]. The AlN in-plane lattice constant is 12% larger than the Pt-Pt distance on the (111) plane which is not an issue for the thicker AlN films. Figure 20 shows a steep transition from compressive to tensile stress as the thickness of

the AlN film increases. The large compressive stress at small thicknesses is very likely due to the lattice mismatch between platinum and aluminum nitride layers.

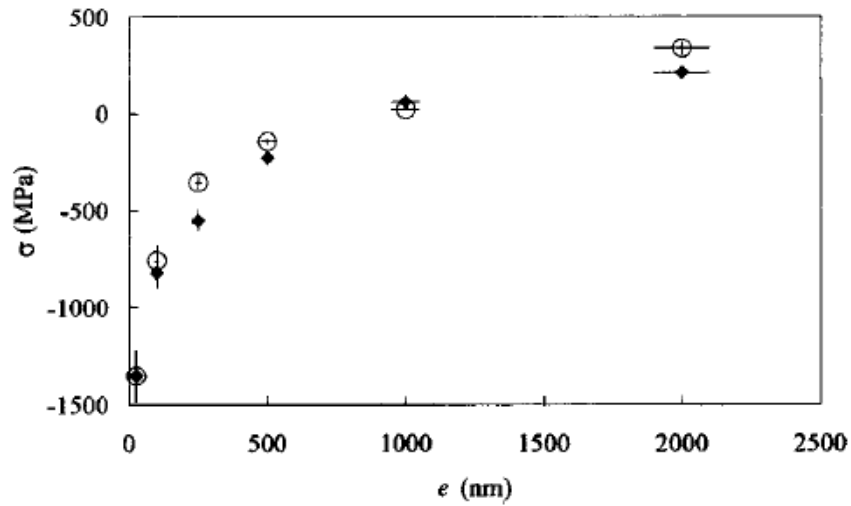


Figure 20: Measured residual stress (solid diamond) and stress derived from out-of-plane strain (XRD-open circles) as a function of AlN thin-film thickness [60]

Figure 21 shows the quality of AlN film grown on top of two different nucleation layers. Platinum grows a well texture columnar structure of AlN film as compared with the AlN grown on top of silicon dioxide layer [61]. In this project, platinum was used as electrode layer for the growth of AlN film and later both the platinum layers (top and bottom) was used for biasing of active (AlN) layer.

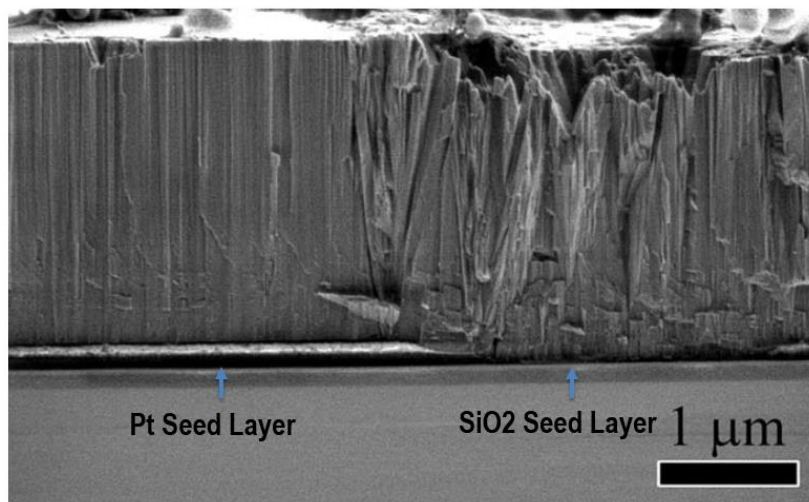


Figure 21: Cross section of an AlN film. The left side shows the film grown on (111)-oriented Pt and the right side shows the growth on thermal SiO₂ [61]

2.4. Optimization of AlN deposition parameters

Characterization of AlN film was one of the critical tasks of this project. Without a well grown columnar structure it is not possible to achieve the required piezoelectric response necessary for the actuation of a cantilever beam. In order to find the appropriate deposition conditions for maximizing the piezoelectric coefficient d_{33} and minimizing the residual stress in the AlN film, different test wafers were deposited with multilayer stack as shown in Figure 10 with different deposition conditions listed in Table 3. In this way, the influence of substrate temperature, power and Ar/N₂ flow rates on the properties of 50 μ m AlN films was investigated. X-ray diffraction (XRD) tool was used to check the crystallinity of AlN thin films and a stress analyzer tool (Toho Technology FLX 2320-S) was used to obtain the in-built stress measurements.

Table 3: Test wafers deposited with different deposition conditions for AlN film growth

Wafer #	Oxide Thickness (nm)	Ar/N ₂	RF Power (W)	T (°C)	FWHM	Stress (MPa)
53814	200 nm SiO ₂	10/40	1500	350	2.58	-1233.55
53809	200 nm SiO ₂	0/50	1500	350	3.29	-1485.87
53808	200 nm SiO ₂	10/40	1500	350	2.78	-1601.28
54023	200 nm SiO ₂	0/50	1500	350	2.88	-1820.04
53860	200 nm SiO ₂	10/40	1500	300	1.79	-1079.25
53877	200 nm SiO ₂	10/40	1500	300	2.59	-791.08
53883	200 nm SiO ₂	0/50	1500	300	2.81	-998.64
53103	295 nm SiO ₂	10/40	1500	200	2.02	-1081.84
53102	295 nm SiO ₂	10/40	1500	200	2.86	-1862.36
52434	295 nm SiO ₂	0/50	1500	200	2.94	-1759.87
52436	295 nm SiO ₂	10/40	1500	200	1.84	-1105.26
55145	295 nm SiO ₂	10/40	1000	300	4.55	-1024.68
55146	295 nm SiO ₂	0/50	1000	300	3.54	-1297.9
53112	295 nm SiO ₂	10/40	1250	300	1.91	-1004.48
53111	295 nm SiO ₂	10/40	1250	300	3.07	-1450.03
53110	295 nm SiO ₂	0/50	1250	300	2.97	-1232.04

A series of conduction tests were performed on the test wafers in order to find out the resistance between the top and bottom electrodes. Ideally, the resistance should be very high preferably in G/MOhms because AlN is an insulator material which is sandwiched between two platinum layers serving as top and bottom electrodes. Mechanical probe station (SuessMicrotec PM8) was used to accurately probe both the platinum layers using the two probe method and Agilent parameter analyzer (Series 415x) was used to record resistance measurements. Resistance measurements give an indication about the quality of AlN thin film. Having low resistance (~ KOhms) between the electrodes shows the presence of pinholes or fractures in the AlN layer causing the current

to leak and short circuit the electrodes. Short circuiting of electrodes does not allow to develop a strong electric field across piezoelectric (AlN) layer which is necessary for the actuation causing the device to fail.

In order to measure the resistance between the top and bottom platinum layers, test structures were fabricated on the test wafers as shown in Figure 22. The test structures consist of an array of squares fabricated on the center and all the four sides of the wafer. Wafer was deposited by all the four layer (top Pt, AlN, bottom Pt, seed layer) and was etched down in inductively coupled plasma in order to expose bottom platinum layer. The detail fabrication process will be explained in chapter 4. Figure 23 shows the final results of fabrication of test structures where squares serve as the contact pads for probing the top platinum layer and ground was used to probe the bottom platinum layer.

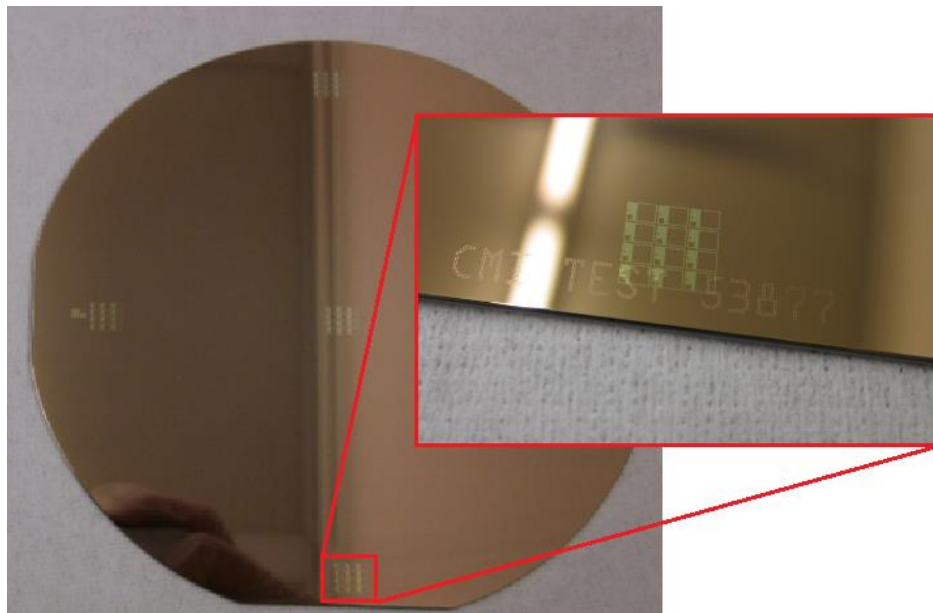


Figure 22: Fabricated test structures for resistance measurements

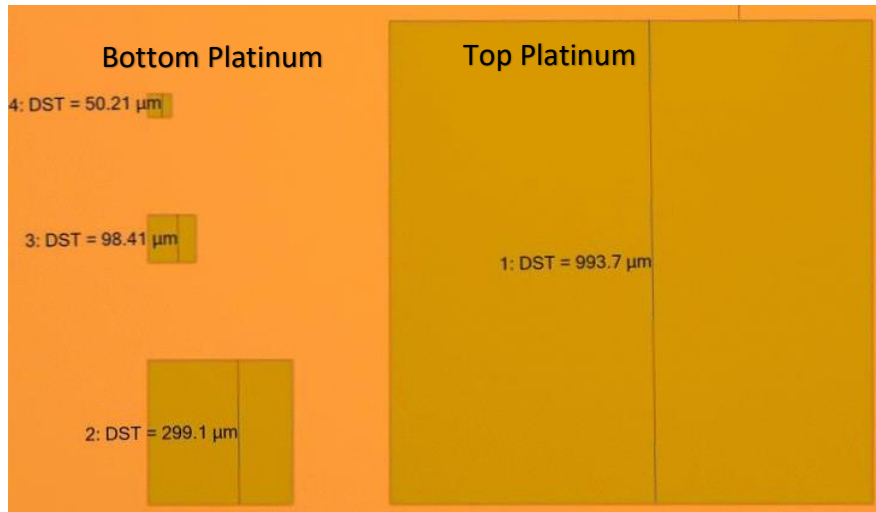


Figure 23: Top and bottom platinum contact pads for resistance measurements

All the test wafers listed in Table 3 were thoroughly tested in order to find the best deposition conditions based on FWHM, residual stress and the resistance between the electrodes. Relatively best results were achieved when AlN was deposited at 300 °C, 1500W and Ar/N₂ flow rate of 10/40. Three new wafers (63673, 63674 and 63675) were deposited with the same deposition parameters for AlN film. These were further used for the fabrication of multilayer cantilevers.

Chapter 3: Finite element analysis of multilayer piezoelectric resonators

ANSYS workbench 17.0 was used for the finite element modelling of different resonator structures including cantilevers and doubly clamped beams. FEM simulations were used to predict the frequency response of resonators for different geometrical configurations and loading forces. The proposed design consists of five different layers joined together to form a single body as shown in Figure 24. Two 25nm of platinum layers were used to apply DC bias across 50nm of aluminum nitride (active) layer. Presence of 15nm of aluminum nitride as a seed layer does not have significant effect on the simulation results but it was essential for the well textured growth of active layer. High stress Silicon nitride layer was used at the bottom in order to add tensile stress in the structure.

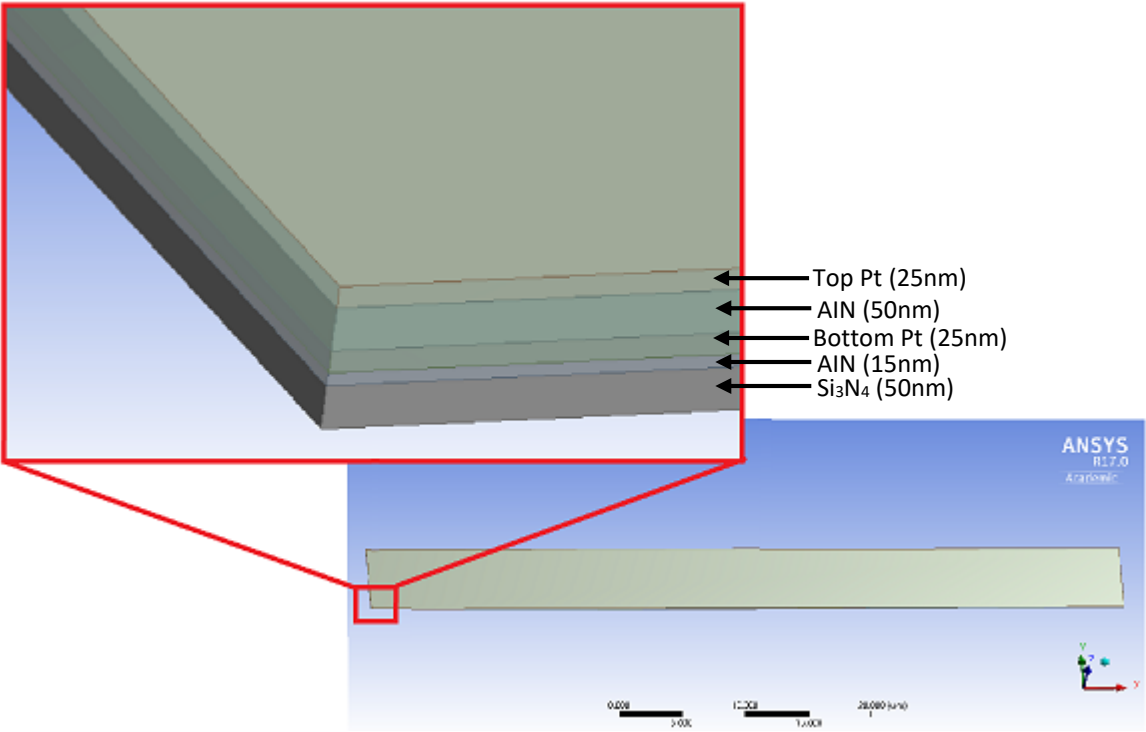


Figure 24: Structural geometry of proposed cantilever design

Table 4 lists down the material properties of different layers that were used in the FEM simulations.

Table 4: Material properties for FEM

Material	Density (Kg/m ³)	Young's Modulus (GPa)	Poisson's Ratio
AlN	3230	345	0.3
Pt	21440	170	0.39
Si ₃ N ₄	3184	265	0.27

3.1. Structural Analysis

Structural analysis was done to find out the cantilever beam deflection and the stress generated due to voltage excitation. Cantilevers of different lengths were simulated in order to study the effect of change in length on the deflection of the beam. First a multilayer beam of 60μm length was designed, meshed and boundary conditions were applied. One end of the beam was fixed for the cantilevers whereas both the ends were fixed for the simulation of double clamped beams. 2V was applied across piezoelectric (AlN) layer and the design was simulated for the total deformation as shown in Figure 25.

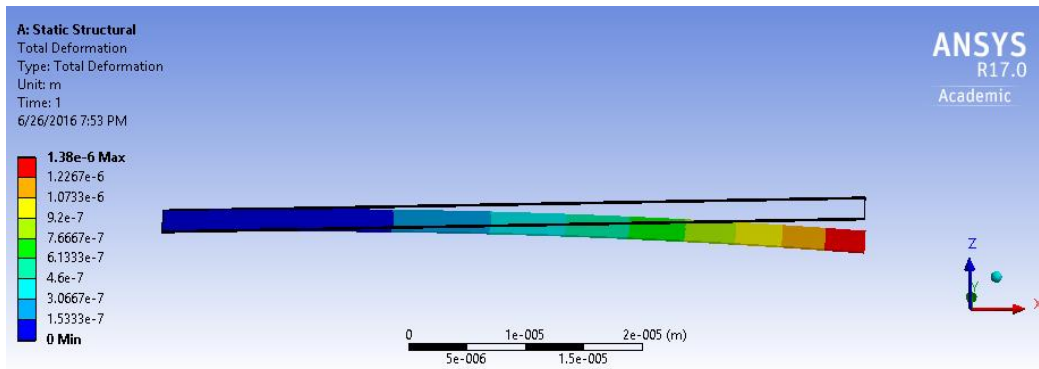


Figure 25: Deflection of the cantilever beam under the influence of 2V

Generation of bending moment in the cantilever structure is directly proportional to the applied voltage across piezoelectric layer. According to equation 4, the piezoelectricity causes the longitudinal strain to develop in the active layer due to applied electric field. As the applied voltage increases, the electric field generated across piezoelectric layer also increases which ultimately enhances the stress induced in the structure. The generation of asymmetrical stress in the structure gives rise to the bending moment, which causes beam deflection. Figure 26 and its corresponding data set in Table 5, shows the direct relationship between the applied voltage and the deflection of cantilever for three different beam lengths. Similarly, the bending of the cantilever beam is proportional to the beam length because the moment is the product of force and distance from the reference point. As the beam length increases the deflection of the cantilever also increases as shown in Figure 27; the corresponding data set in provided in Table 6. All the beams were simulated at 2V with the constant width of 6μm.

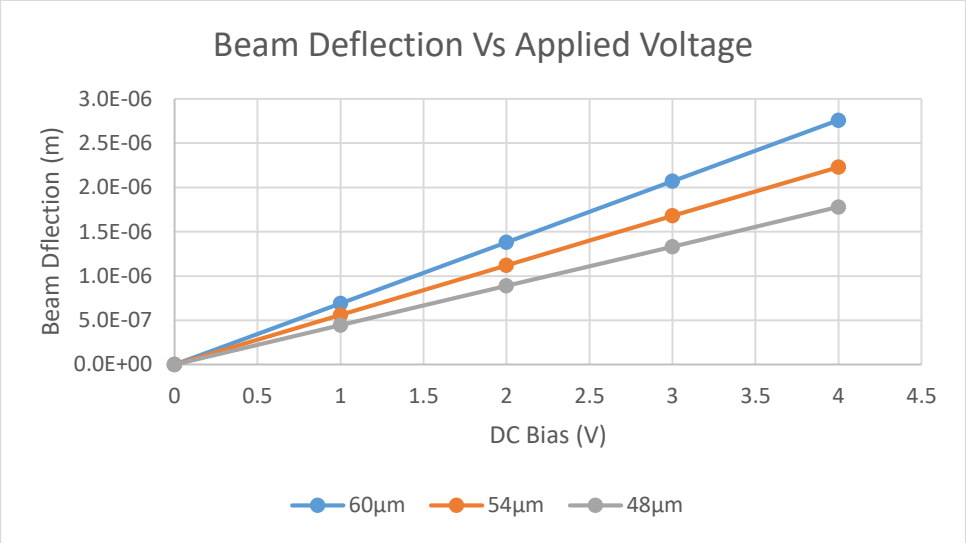


Figure 26: Relationship between cantilever bending and applied potential for three different beam lengths

Table 5: Simulated results of cantilever deflection expressed in microns for different applied voltages

DC Bias (V)	60µm	54µm	48µm
0	0	0	0
1	0.69	0.56	0.45
2	1.4	1.1	0.89
3	2.1	1.7	1.3
4	2.8	2.2	1.8

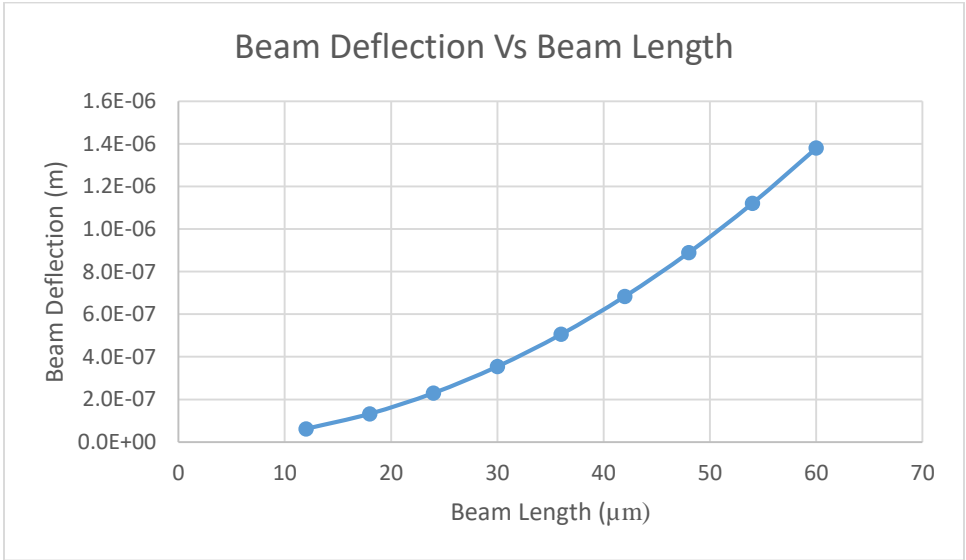


Figure 27: Deflection of cantilever for different beam lengths

Table 6: Data set for cantilever deflection expressed in microns for different beam lengths

Length (μm)	Deflection (μm)
60	1.4
54	1.1
48	0.89
42	0.68
36	0.51
30	0.35
24	0.23
18	0.13
12	0.062

3.2. Modal Analysis

Modal analysis was carried out to find the resonance frequency and the mode shapes of cantilever for different lengths. The effect of applied voltage on the change in resonance frequency was also studied. Resonance frequency is inversely proportional to the square of length of the beam as shown in equation 5. The same behavior was achieved when a $6\mu\text{m}$ wide cantilever was simulated over the range of different lengths to find out the resonance frequency of the first mode as shown in Figure 28 and in its corresponding data set in Table 7.

$$f_{res} = \frac{(1.875)^2}{2\pi} \sqrt{\frac{EI}{\rho AL^4}} \quad (5)$$

where E is Young's Modulus, I is moment of inertia, ρ is material density, A is area of cross section and L is the length of the cantilever beam.

Stress generated in piezoelectric layer due to applied voltage also changes the resonance frequency of the vibrating structure. Application of surface stress induces an axial force along the length of the beam and the cantilever vibrates with the shifted resonance frequency [62]. Pre-stress analysis of the cantilever was done in order to find the shift in resonance frequency due to applied voltage. First the stress in the cantilever due to applied voltage was simulated and then the generated stress was used as an input parameter for the modal analysis to calculate the resonance frequency of the prestressed cantilever beam. Table 7 lists the shift in resonance frequency values for different beam lengths at 5V.

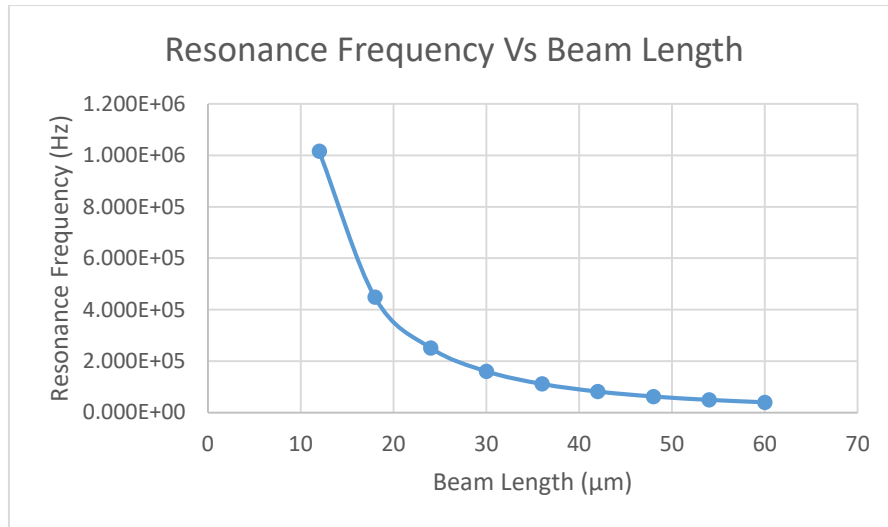
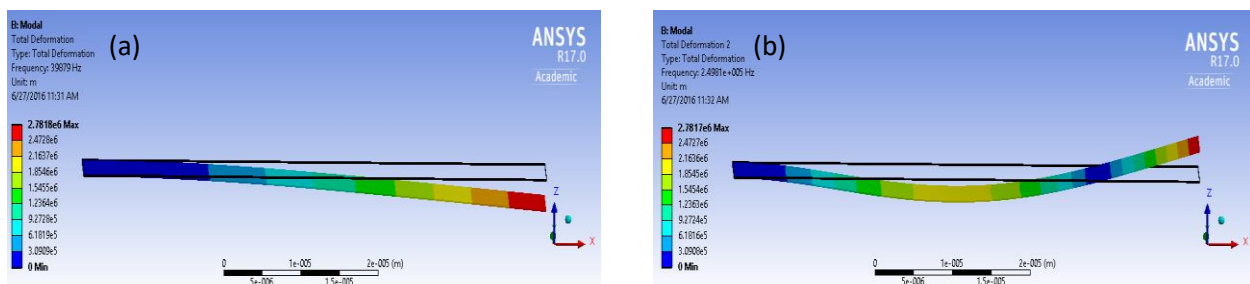


Figure 28: Reduction in first modal resonance frequency of the cantilever with increase in beam length

Table 7: Data set for the first modal resonance and prestressed resonance frequencies for different beam lengths

Beam Length (μm)	Resonance Frequency (Hz) f_{res}	Prestressed Frequency (Hz) f_{pre}	Frequency Shift (Hz) $f_{pre} - f_{res}$
60	3.988E+04	4.33E+04	3.40E+03
54	4.926E+04	5.12E+04	1.91E+03
48	6.240E+04	7.00E+04	7.59E+03
42	8.159E+04	8.19E+04	3.32E+02
36	1.112E+05	1.13E+05	1.42E+03
30	1.605E+05	1.06E+05	-5.44E+04
24	2.514E+05	2.03E+05	-4.88E+04
18	4.487E+05	4.35E+05	-1.38E+04
12	1.016E+06	1.01E+06	-3.15E+03

Figure 29 shows the first three mode shapes of 60x6 μm cantilever beam under no loading force.



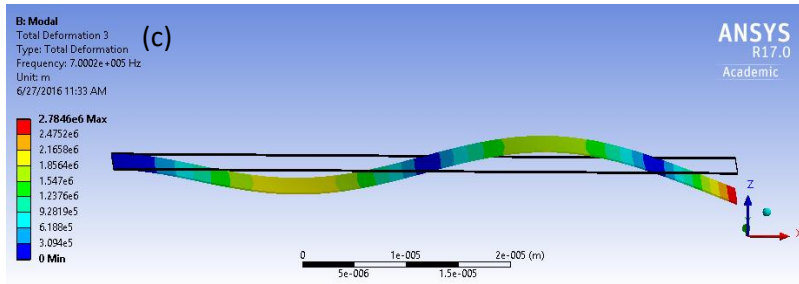


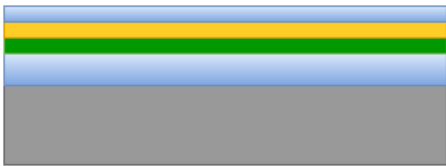



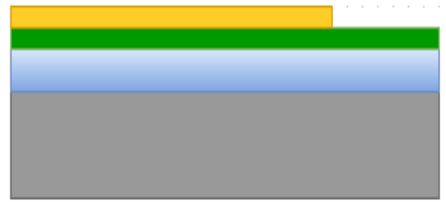


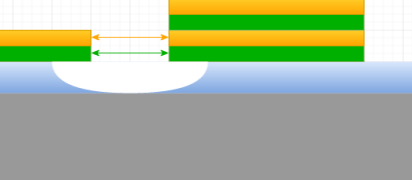

Figure 29: First three mode shapes of a 60x6 μ m cantilever under no loading force; (a) f_{res} of first mode is 39879 Hz; (b) f_{res} of second mode is 2.4981e+5 Hz; (c) f_{res} of third mode is 7.0002e+5Hz

Chapter 4: Fabrication

Device fabrication was carried out in the EPFL Cleanroom. Two different process flows were implemented in order to achieve the desired results. In the first process flow, a bottom-up approach was implemented. First only the seed and bottom platinum layers were deposited, patterned and etched and afterwards the other two layers (AlN and top Pt layer) were deposited and processed according to the first process flow. Unfortunately, the desired electrical insulation between the top and the bottom platinum layers was not achieved due to the generation of high fences on the sides of the bottom platinum layer. In order to tackle this problem, a new process flow was implemented with a top-down approach where all the four layers (seed, bottom Pt, AlN and top Pt layers) were deposited at once and etched downwards. The desired electrical insulation between the top and bottom platinum layers was achieved which ultimately led to the successful fabrication of multilayer cantilevers and doubly clamped beams.

In this chapter, the first process flow will be explained in detail along with the basic operation of the machines used for the fabrication but the second process flow will be explained briefly except the steps which have not been already discussed in the first process flow.

4.1. First Process Flow

<p>(a) Multilayer deposition of AlN, Pt and SiO₂</p> 	<p>(f) Dry Etching of SiO₂, Pt & AlN in STS</p> 
<p>(b) Photolithography of Bottom Pt Layer</p> 	<p>(g) Photolithography of Devices</p> 
<p>(c) Dry Etching of SiO₂ & Pt in IBE</p> 	<p>(h) Dry Etching of Pt & AlN in STS</p> 
<p>(d) Multilayer deposition of AlN, Pt & SiO₂</p> 	<p>(i) Structure Releasing</p> 
<p>(e) Photolithography of Top Pt Layer</p> 	

Note:

The arrows indicate that AlN/Pt layers are connected out of present section plane.

Legend:



SiO₂ Layer



AlN Layer



Pt Layer



Photoresist Layer

4.1.1. Mask Design

CleWin 4 was used to design the proposed mask. The designed mask consisted of four layers. Figure 30 shows the first and second mask layers that were used to pattern the bottom and top platinum layers respectively. After patterning the bottom platinum layer, it was etched down to the seed layer. So the light blue rectangle in Figure 30(a) represents a rectangular structure of bottom platinum layer on the wafer which consisted of two layers (bottom Pt and seed layer) whereas all the area around this structure was etched down to the seed layer. After this, the next two layers (AlN and top Pt layer) were deposited and patterned with the second mask layer. The top platinum layer was etched down to the bottom platinum layer and the squares of second mask layer on top of first mask layer in Figure 30(b) represents the whole layer stack (seed, bottom Pt, AlN and top Pt layers) on the wafer whereas the other squares were later used to make contact pads for top platinum layer.

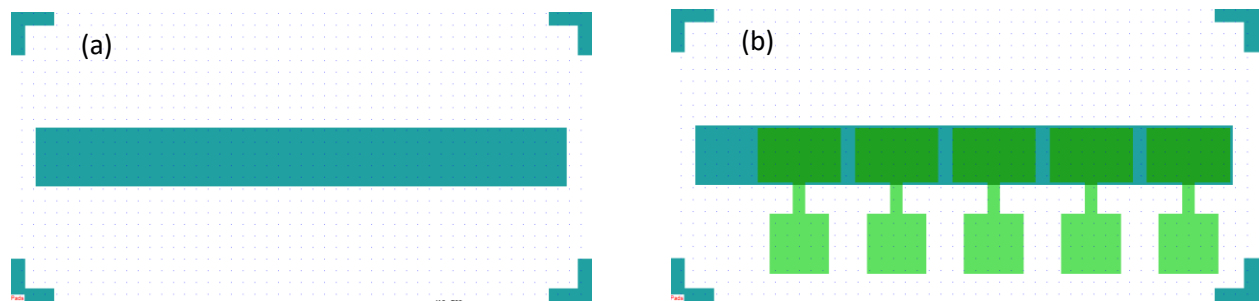


Figure 30: (a) First mask layer for patterning of bottom platinum layer; (b) Second mask layer for patterning of top platinum layer

The third mask layer was the device layer which consisted of cantilevers and clamp-clamp beams of different dimensions as shown in Figure 31(a). The dimensions of the devices ranges from $2 \times 1 \mu\text{m}$ to $50 \times 5 \mu\text{m}$. The devices were patterned only on the four layers stack squares and were etched down all the way till the surface of the wafer in order to make the openings which were later used for releasing the devices. Figure 31(b) shows the fourth mask layer that was used to make contact pads for top and bottom platinum layers. As different top platinum squares are on the same bottom platinum layer so only one contact pad was enough to provide electrical potential to all the devices whereas different top platinum squares had their separate contact pads for providing potential to the top platinum layer.

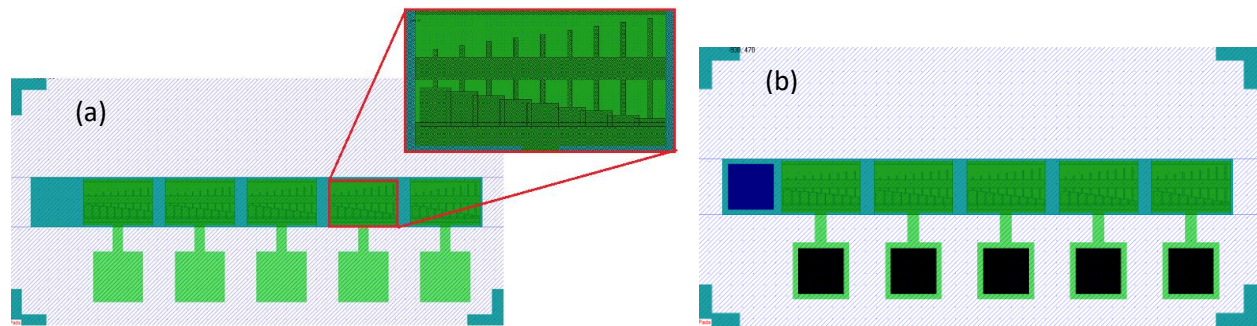


Figure 31: (a) Third mask layer for patterning of devices on top platinum layer; (b) Fourth mask layer for patterning of contact pads

Alignment marks were used on both the edges of the wafer to accurately align different layers as shown in Figure 32.

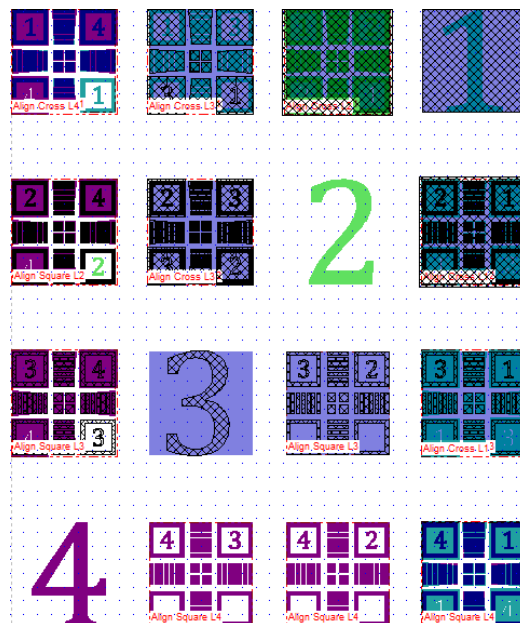


Figure 32: Alignment marks

4.1.2. Experimental Work

(a) Multilayer deposition of AlN, Pt and SiO₂:

A batch of three 4'' p-type wafers (62528, 62529 & 62531) was used to deposit 15nm of AlN seed layer, 25nm of Pt bottom layer and 50nm of SiO₂ layer. These wafers were already thermally oxidized with 295nm of SiO₂ layer. A sputtering tool (SPIDER) was used for deposition of all the layers at once. SPIDER is a magnetron sputtering tool consists of four chambers used for the thin film deposition of metal and dielectric materials. Figure 33 shows the wafer after deposition of

all the layers. It must be noted that the silver color appears due to the presence of 25nm thick Pt layer. The deposition rates were already optimized. Table 8 shows the deposition rates of AlN, Pt and SiO₂ and the time of deposition that was required to achieve the desired thicknesses.



Figure 33: Appearance of silver color after Pt layer deposition

Table 8: Optimized deposition rates for SPIDER

Layers	Deposition rate	Required Layer Thickness	Deposition Time
AlN	50nm/min	15nm	18sec
Pt	250nm/min	25nm	6sec
SiO ₂	20nm/min	50nm	2min 30sec

As explained in chapter 2, the deposition conditions for AlN and Pt were already optimized after carefully analyzing the crystallinity and residual stress of AlN deposited on different test wafers. Table 9 lists down only the most critical deposition parameters for AlN, Pt and SiO₂ films.

Table 9: SPIDER Deposition parameters for AlN, Pt and SiO₂ films

Layers	Temperature (°C)	Power (W)	Ar/N ₂ flow rate
AlN	300	1500	10/40
Pt	300	680	15/0
SiO ₂	32	900	98/0

(b) Photolithography of Bottom Pt Layer:

A photolithography system for coating and development (ACS200 GEN3) was used to coat 0.6 μm thickness of AZ ECI 3007 positive photoresist. ACS200 is a fully automatic photoresist processing system that involves adhesion promotor, coating, soft baking, development and special thermal treatments (6 hotplates and 3 cool plates). A separate exposure tool Maskless Aligner (MLA 150) was used to expose AZ ECI 3007 photoresist. MLA 150 is a direct laser writing tool that does not need a physical mask but only a design file (gds or cif) for exposure. The tool is equipped with 405nm laser diode for only h-line photoresist ($\lambda=405\text{nm}$). Dose (mJ/cm^2) and defocus are the two main important parameters that depend on the thickness of photoresist and the reflectivity of bottom layers. Dose controls the intensity of laser beam and defocus define the location of camera focus. Both parameters were optimized with the help of dose test in order to achieve good exposure results.

The silicon wafers were pretreated with vapor HDMS (Hexamethyldisilazane) for better photoresist adhesion and coated with 0.6 μm AZ ECI 3007 photoresist in ACS200. The exposure dose test was done over the range of doses from 100 mJ/cm^2 to 160 mJ/cm^2 and defocus from -3 to +3. The results were visualized under microscope and for dose 130 mJ/cm^2 and defocus -3. The structures were well-defined and photoresist was properly exposed. The wafers were then exposed in MLA 150 with the first mask layer as shown Figure 34. After exposure, wafers were developed in ACS200 and photolithography results were analyzed under microscope.

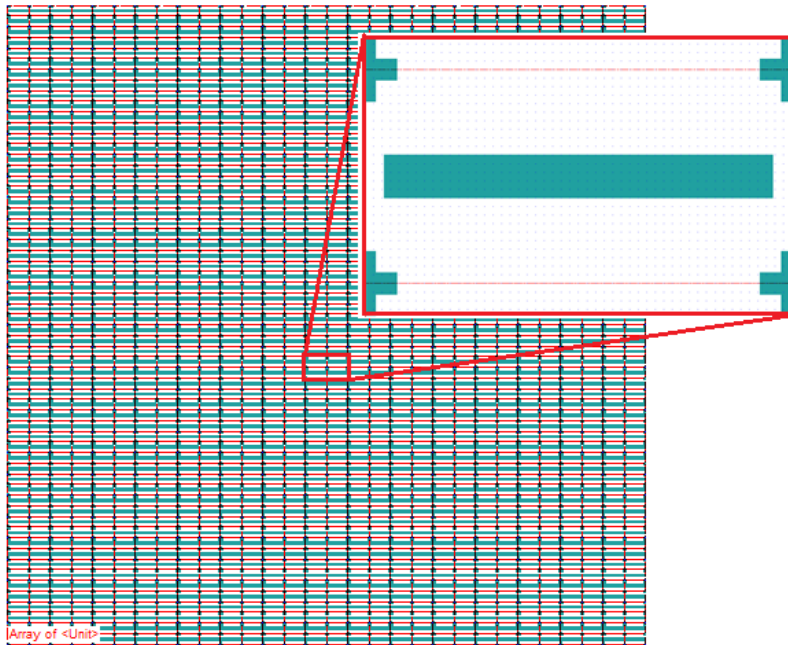


Figure 34: First mask layer to pattern bottom Platinum layer electrode

(c) Dry Etching of SiO₂ & Pt in IBE:

Ion Beam Etcher (Nexus IBE350) was used to etch the unprotected parts of wafer by the bombardment of high energy argon ions. Only the top two layers (SiO₂ and Pt) were etched and the etching was stopped when the seed (AlN) layer was exposed. Table 10 shows the etch rates of SiO₂ and Pt for Nexus IBE350 and the total required etch time.

Table 10: Approx. etch rates of SiO₂ and Pt for Nexus IBE350

Layers	Approx. Etch Rate	Layer Thickness	Estimated Etch Time	Actual Etch Time
SiO ₂	55nm/min	50nm	55sec	47sec
Pt	71nm/min	25nm	21sec	17sec

The available etch rates were not properly optimized so the etching was done in multiple small steps and the actual etch time was much less than the estimated etch time. After every step, the resistance of the top layer was measured by digital multi-meter in order to find out whether the platinum layer has been etched away completely or not. Platinum is a very good conductor whereas the underneath AlN is an insulator material so the resistance in ohms indicated the presence of Pt layer whereas the resistance in M/GOhms indicate the start of AlN layer. Secondly, platinum is silver in color and AlN is purple. At the end of etching the whole wafer was turned purple except the areas protected by photoresist as shown in Figure 35 which also gives an indication for the termination of etching.

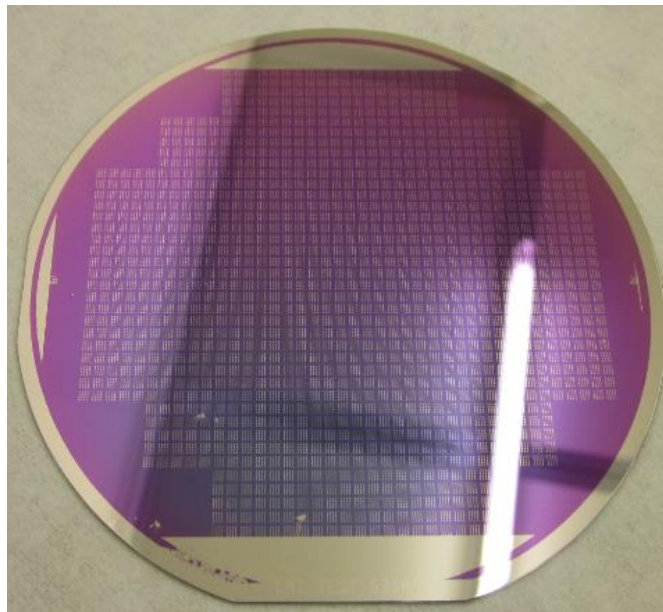


Figure 35: Appearance of purple color gives an indication of complete etching of top layers and shows that underneath AlN layer has been exposed

Once the etching was done, the photoresist and oxide was stripped off and the wafers were prepared for the deposition of next layers. The stripping of photoresist was carried out in high frequency oxygen plasma (Tepla GIGAbatch) and wet etching at 70°C in Shipley Remover 1165 (UFT Resist Bath). Due to dry etching, the surface of the photoresist gets hard and stripping photoresist in UFT Resist Bath alone takes a lot of time. In order to speed up the removal process, first the wafers were put in high power oxygen plasma for 5 minutes and then were put in UFT Resist Bath for 10 minutes. UFT Resist Bath consists of a dirty and clean bath both having 1165 remover at 70°C. Wafers were put in each bath for 5 minutes and then was rinsed in distilled water properly. SRD was used to dry the wafers. After removing the photoresist, the oxide layer was exposed which also needed to be removed before depositing next layers. Oxide stripping was done in Buffered Hydrofluoric acid (BHF) in Plade wetbench. Etch rate for sputtered oxide in BHF is very high (~500nm/min) so wafers were put in Plade Wetbench for 30s to get rid off 50nm of oxide layer. After etching in BHF, the wafers were rinsed properly and dried in SRD.

(d) Multilayer deposition of AlN, Pt & SiO₂:

Once the bottom platinum electrode was fabricated, again SPIDER was used to sputter 50nm of AlN (active layer), 15nm of Pt (top electrode) and 50nm of SiO₂ layer. SPIDER parameters for deposition of AlN, Pt and SiO₂ films have already been discussed in Table 9. Table 11 shows the deposition rates of AlN, Pt and SiO₂ and the time of deposition that were required in order to achieve the desired thicknesses. The deposition time for 50nm of AlN film is 1 minute but the deposition was carried out in two steps. First AlN was deposited for 50s and then for 10s. Both deposition steps were separated by the duration of 5 minutes. It has been observed that AlN grows in form of small islands of grains and the size of an island depends on the adatom motilities and the wetting angle between the film and substrate [63][64]. As the AlN film grows thicker, islands coalesce into a continuous film but in case of ultra-thin layer there are some gaps left in between the grains resulting in a non-uniform growth of AlN layer and degrades the piezoelectric response. So deposition was done in two step, in the first step the grains were formed and in the second step the material was deposited in between the grains to produce a uniform film.

Table 11: Optimized deposition rates for SPIDER

Layers	Deposition rate	Required Layer Thickness	Deposition Time
AlN	50nm/min	50nm	50sec & 10sec
Pt	250nm/min	15nm	6sec
SiO ₂	20nm/min	50nm	2min 30sec

(e) Photolithography of Top Pt Layer:

Top platinum layer was patterned with the second mask layer as shown in Figure 36. ACS200 was used to coat the wafers with $1\mu\text{m}$ of AZ ECI 3007 and MLA 150 was used as an exposure tool. As the wafers already had the first mask layer patterned on the bottom platinum layer so it was very important to use alignment marks for the alignment of second mask layer with the first layer on the wafer. As MLA 150 does not require any physical mask rather only a mask design file for exposure so X and Y coordinates of alignment marks were very accurately found from the design file and was entered in the program software. The next job was to indicate the physical location of alignment marks on the wafer with the help of a camera and the program automatically aligns the alignment marks of design file and the wafer. Again the exposure dose test was done over the range of doses from 120 mJ/cm^2 to 140mJ/cm^2 and defocus from -4 to -1 and the best exposure results were obtained for dose 130 mJ/cm^2 with defocus of -4 . After exposure, wafers were developed in ACS200. Figure 37 shows alignment marks after the development of wafer.

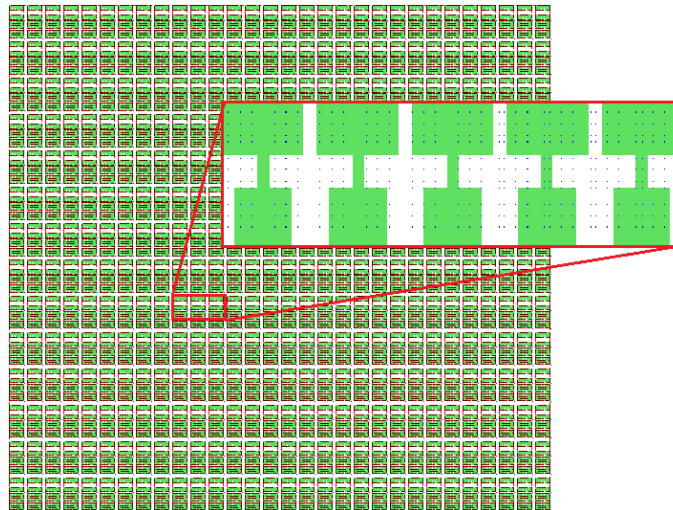


Figure 36: Second mask layer to pattern top Platinum layer electrode

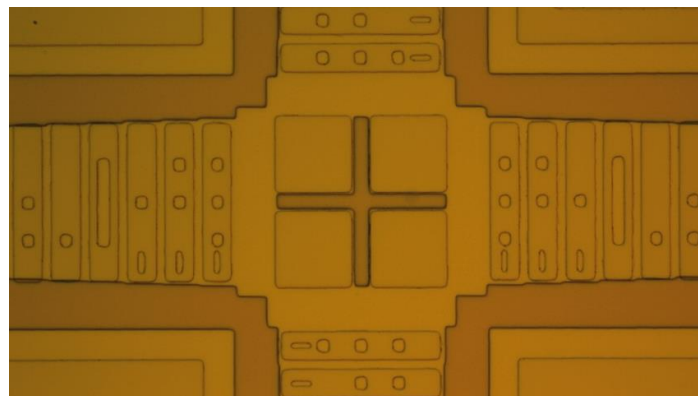


Figure 37: Fitting of plus (+) sign inside the square shows the perfect alignment of second layer with the first layer

(f) Dry Etching of SiO₂, Pt & AlN in STS:

Etching of SiO₂, top Pt and AlN layers till the bottom Pt layer was the most difficult and critical step of this process flow. The dry etching of SiO₂, Pt and AlN was achieved by an inductively coupled plasma system (STS Multiplex) using Cl₂/Ar chemistry. STS Multiplex provides high density and high ion current plasma at low pressure where argon ions bombard the target in presence of chlorine gas. Table 12 shows the etch rates and etch time of SiO₂, Pt and AlN for STS Multiplex. It was essential to stop the etching when the bottom platinum layer was exposed. So in order to achieve that the etching was done in multiple small steps and the resistance of top layer was measured with digital multimeter in every step to get an idea regarding the material of the top surface. End point system was also used to find out the current etching layer. End point systems works with the intensity of light reflected from the surface of the wafer. Pt has high reflectivity than AlN so light reflected by Pt surface has more intensity than AlN which was also used as an indicator to find out the etching layer. The total time required to etch SiO₂, Pt and AlN layers was 2 minutes which was more than the time estimated from the etch rates. As the etching was done in multiple steps, so for every step plasma needs some time to ramp up and reaches its maximum intensity which overall takes longer than etching continuously. Once the etching was done, the photoresist was stripped off and the wafers were ready for patterning of devices.

Table 12: Etch rates and etch time of SiO₂, Pt and AlN for STS Multiplex

Layers	Approx. Etch Rate	Layer Thickness	Estimated Etch Time
SiO ₂	70nm/min	50nm	42.8sec
Pt	27nm/min	15nm	33.3sec
AlN	285nm/min	50nm	10.4sec

(g) Photolithography of devices:

Third photolithographic step was done to pattern devices on the top Pt layer. All three wafers were coated with 1µm of AZ ECI 3007 in ACS200 and were exposed in MLA 150. Exposure dose test was not done for this stage because we already had the optimized MLA 150 exposure parameters from the last photolithography stage. Figure 38 shows the third mask layer, which consists of cantilevers and double clamped beam of variable dimensions. Again alignment marks were used to align the third mask layer with the preceding layers on the wafer. Dose 130 mJ/cm² and defocus -4 was used for exposure and ACS200 was used to develop the wafers.

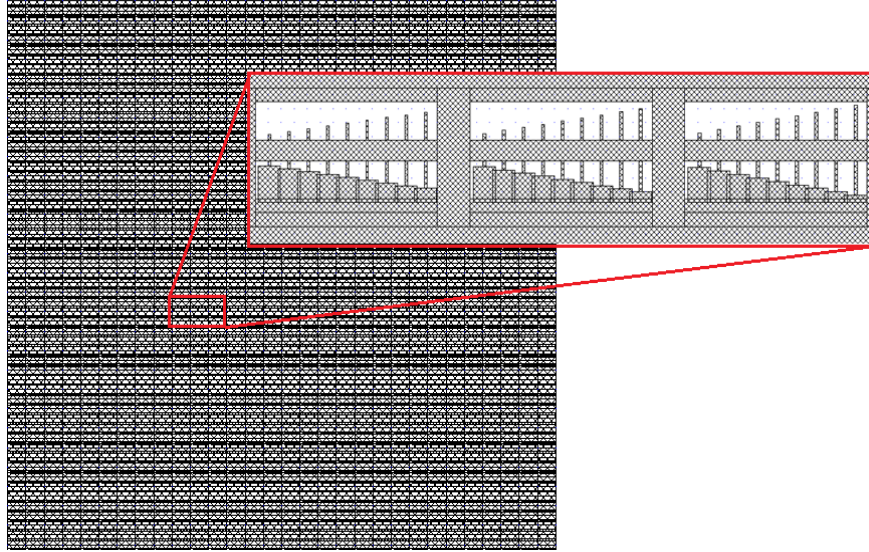


Figure 38: Third mask layer to pattern devices

Figure 39 shows the photolithography results of all the three stages, which includes patterning of bottom Pt layer, top Pt layer and devices. Overall the good photolithography results were achieved due to optimization of exposure parameters at every stage. Figure 40 shows photolithography results of 5 μm wide cantilevers of different lengths. The cantilevers were well defined and there was not any unwanted photoresist remaining near the structures.

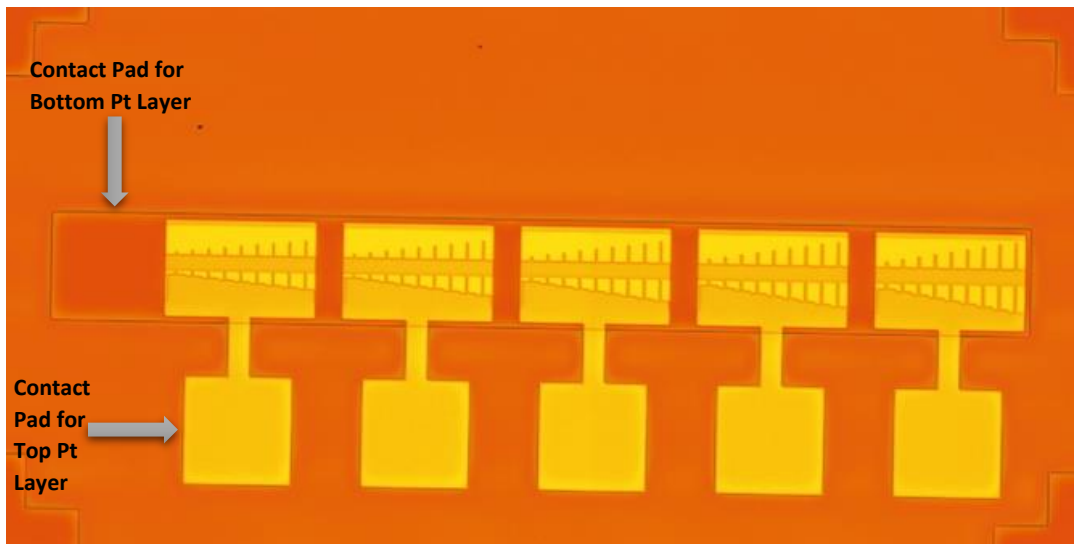


Figure 39: Photolithography results after development of device layer

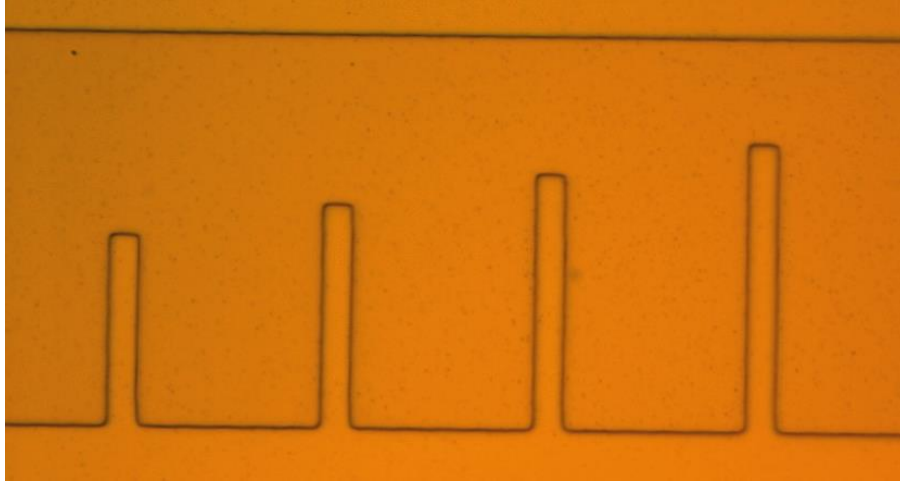


Figure 40: Photolithography results of 5 μm wide cantilevers after development

The minimum feature size that can be achieved with MLA 150 is 1 μm provided that exposure is done with very accurate exposure parameters. Figure 41 shows the exposure results of 1 μm wide cantilevers. The structures are overexposed and the dose 130 mJ/cm^2 needs to be further optimized in order to get well-defined 1 μm wide structures.

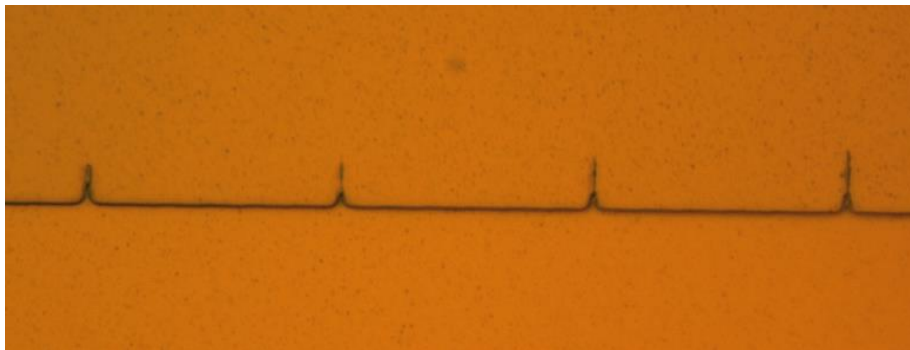


Figure 41: Poor photolithography results for 1 μm wide cantilevers due to overexposure

(h) Dry etching of Pt & AlN in STS:

Once the devices were patterned, the etching was done using STS Multiplex all the way to the surface of the wafer in order to make the openings around the cantilevers and beams. These openings were later used by solvent/gas to etch material from the sides of the structures in order to release them. Table 13 shows the etch rates and etch time of all the layers for STS Multiplex. Total etch time was 2 minutes and 30s which was very close to the estimated etch time of 2 minutes and 25s because etching was done continuously for the whole etch time.

Table 13: Etch rates and etch time of SiO₂, Pt and AlN for STS Multiplex

Layers	Approx. Etch Rate	Layer Thickness	Estimated Etch Time
SiO ₂	70nm/min	50nm	42.8sec
Top Pt	27nm/min	15nm	33.3sec
AlN	285nm/min	50nm	10.4sec
Bottom Pt	27nm/min	25nm	55.5sec
Seed	285nm/min	15nm	3.1sec

The dark brown portion in Figure 42, shows that layers have been etched all the way to the surface of the wafer. It was also verified by spectroscopic reflectometer (Nanospec AFT-6100). Nanospec is used to measure the thickness of single or multilayer stack. Nanospec showed the perfect curving fitting with the reflectance values obtained from the reference silicon wafer and the dark brown portion in Figure 42 which shows the removal of all the Pt and AlN layers.

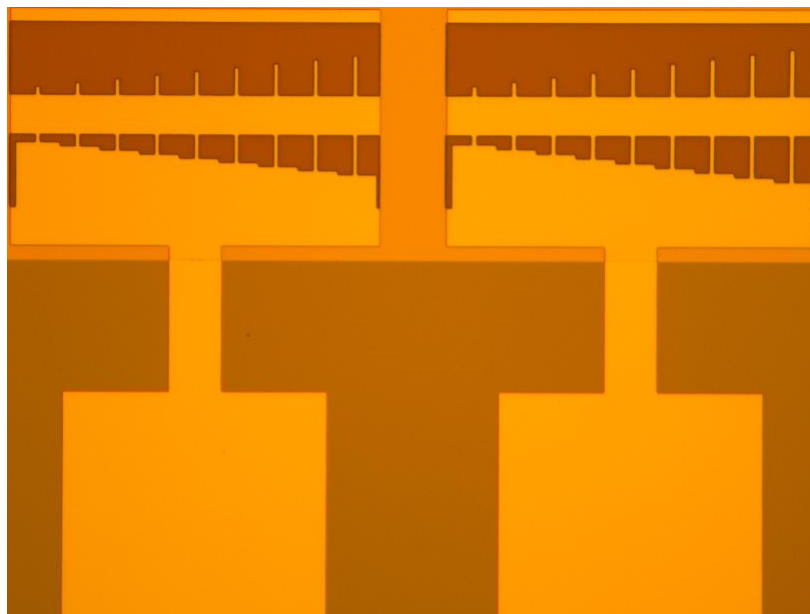


Figure 42: Making of openings for structure releasing

(i) Structure release:

Releasing cantilevers and doubly clamped beams was the last step of this process flow. There were two options for releasing the devices. First was to etch silicon wafer using Bosch process and then use SF₆ gas to etch the material from underneath the structures or to only etch the oxide layer using wet/dry etching. It should be noted that wafers already had a 295nm of thick thermally grown oxide layer and by etching away only this layer from underneath the devices, without etching silicon wafer could also lead to the release of devices. Buffered Hydrofluoric acid

(BHF) was used to etch oxide layer with the etch rate of 77nm/min. After etching in BHF, the wafers were placed in Isopropanol (IPA) for 1 minute in order to remove any trapped water droplets from under the released structures that could possibly cause stiction. Figure 43 & Figure 44 show the SEM images of released cantilevers. Due to the wet etching of oxide layer, most of the cantilevers were suffering from stiction.

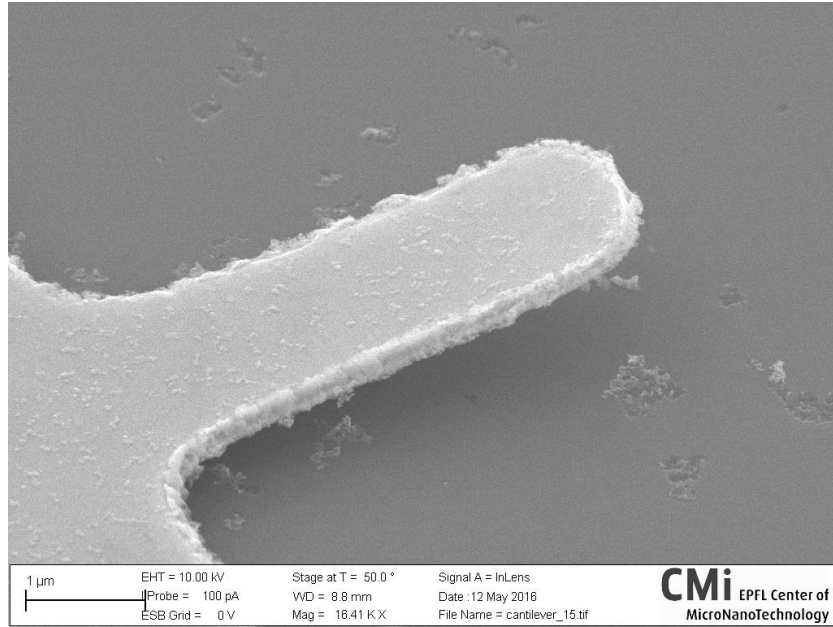


Figure 43: Released cantilever after wet etching of oxide layer

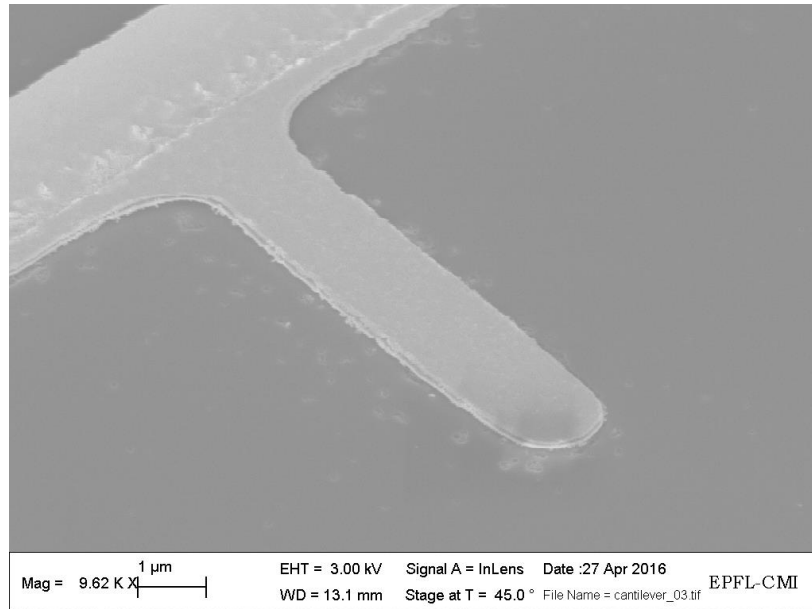


Figure 44: Cantilever suffering from stiction

4.1.3. Discussion

Reactive Ion Etching (RIE) and Ion Beam Etching (IBE) are the most effective techniques for the etching of platinum layer but their major drawback is the redeposition of etched material on the side wall of the trenches especially on the walls of masking (photoresist) layer as shown in Figure 45. The material deposited on the side walls during etching does not remove after stripping off the mask layer and takes the shape of very high aspect ratio structures commonly called as fences.

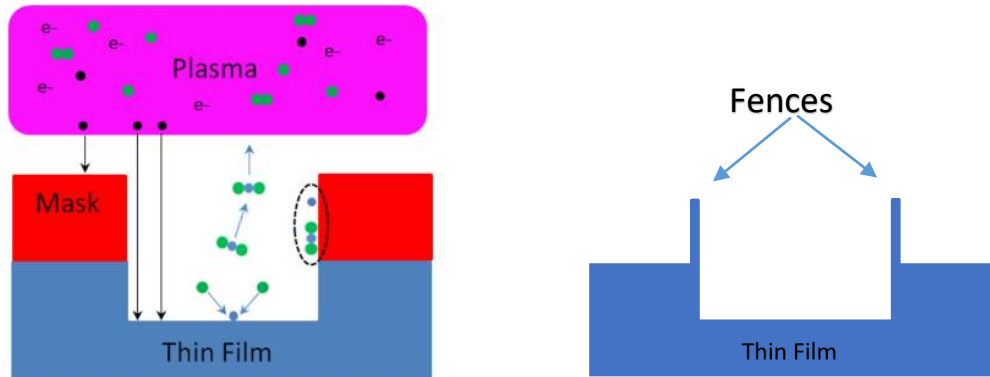


Figure 45: Processes involved in dry etching and formation of fences due to redeposition of etched material on the side walls

Formation of fences in microfabrication is a very well-known problem that could possibly lead to the failure of the MEMS devices. Depending on the thickness of mask layer and the duration of etching the height of fences can vary from 10's of nm to few 100 nm. These fences have negligible effect on the device performance if the thickness of layers are in microns but in our case the layers are in nanometer scale which drastically increases the chances of failure due to extremely high fences. Figure 46 shows a very high fence on the side of platinum layer with is due to redeposition of material during etching in IBE.

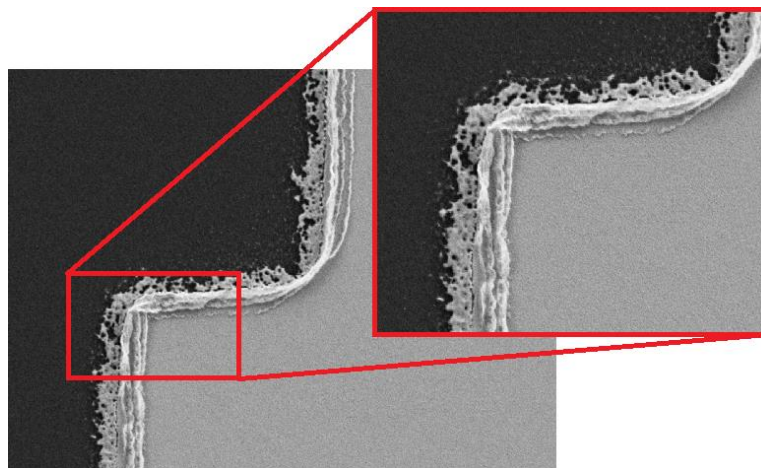


Figure 46: Formation of high fence on the edge of platinum layer after dry etching

4.1.3.1. Possible causes for device failure

As discussed earlier, the electrical insulation between the top and bottom platinum layers was essential for the functionality of multilayer piezoelectric cantilevers. Unfortunately, the desired electrical insulation between the top and bottom platinum layers was not achieved which led to the failure of the devices. The possible reasons for the device failure could be poor growth of AlN film or the presence of high fences on the bottom platinum layer. Both the platinum layers were separated by 50nm thick layer of AlN which is an insulator material and it should not let current to flow through it. Presence of pin holes or fractures in the AlN film can cause leakage current to flow through it and leads to the short circuiting of platinum electrodes.

Another possible reason for the conduction between the top and bottom platinum layer is the presence of fences on the bottom platinum layer due to etching in IBE. We believe that the possible point of failure is the crossover region where top platinum layer step over to the bottom platinum layer as shown in Figure 47. Fences at the edge of bottom platinum layer disrupts the uniform growth of AlN and top platinum layers at the crossover region as shown in Figure 48. The fences from the bottom platinum layer are high enough to pinch all the way through the top platinum layer causing conduction.

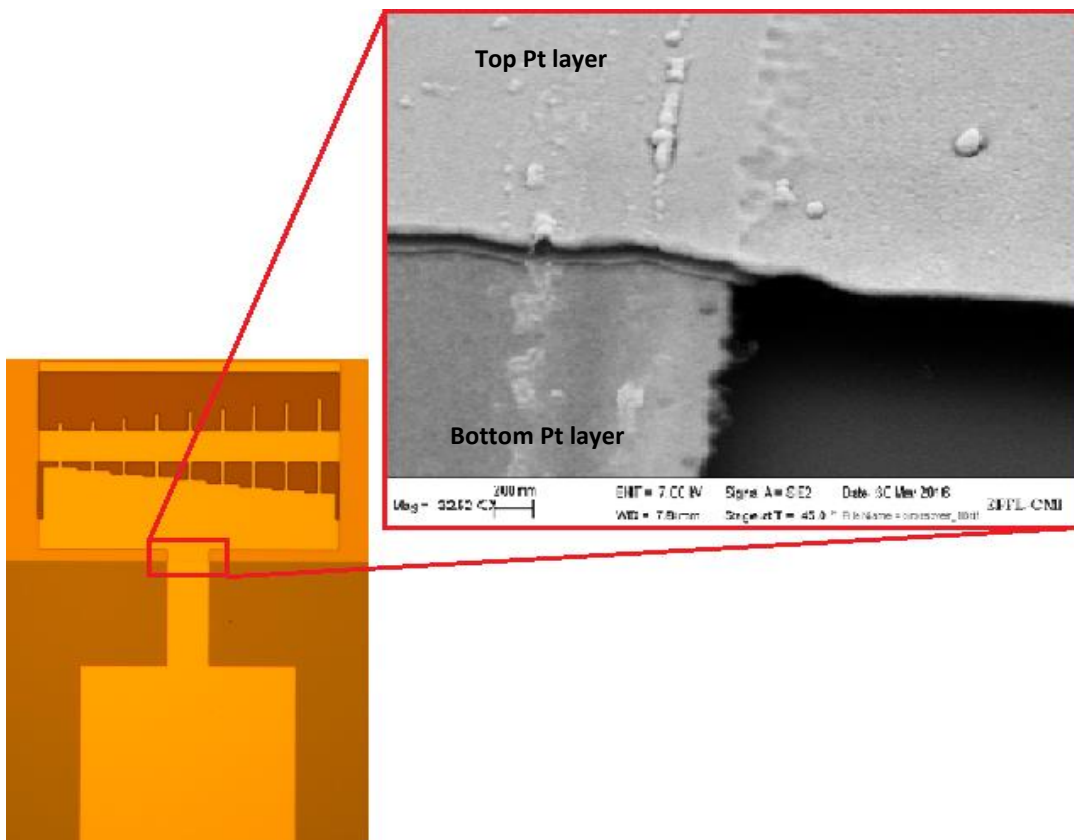


Figure 47: SEM image shows the possible region of failure where top Pt layer step onto the bottom Pt layer

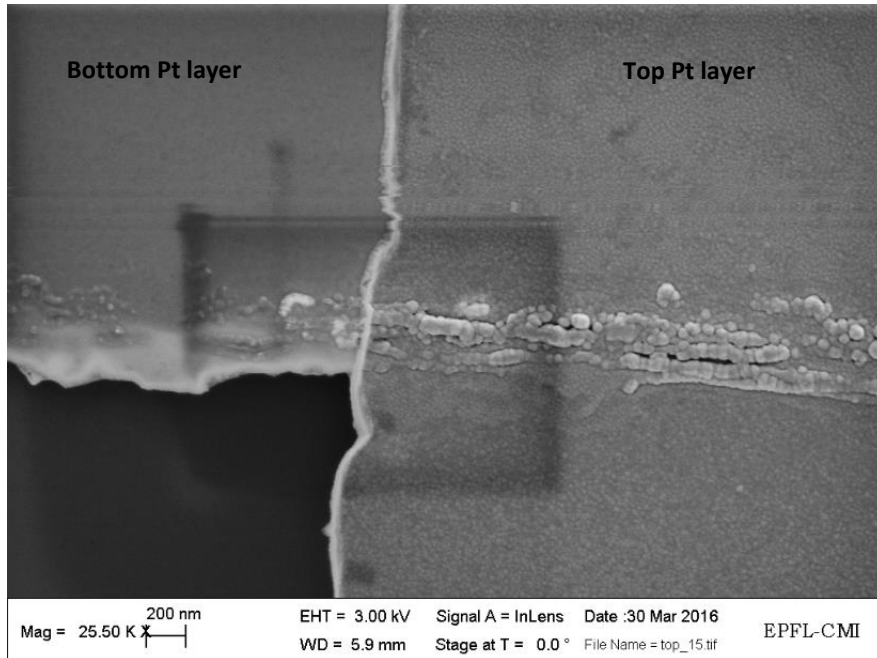


Figure 48: SEM image showing fences of bottom Pt layer that are visible on the top Pt layer

Redeposition of unwanted material during etching of top platinum layer in STS can possibly be another reason for conduction between the platinum layers. The fences from the top platinum layer can fall down on the bottom platinum layer or unwanted material deposition due to dirty chamber can lead to the conduction between the platinum layers, if the deposited material contains any metallic components as shown in Figure 49.

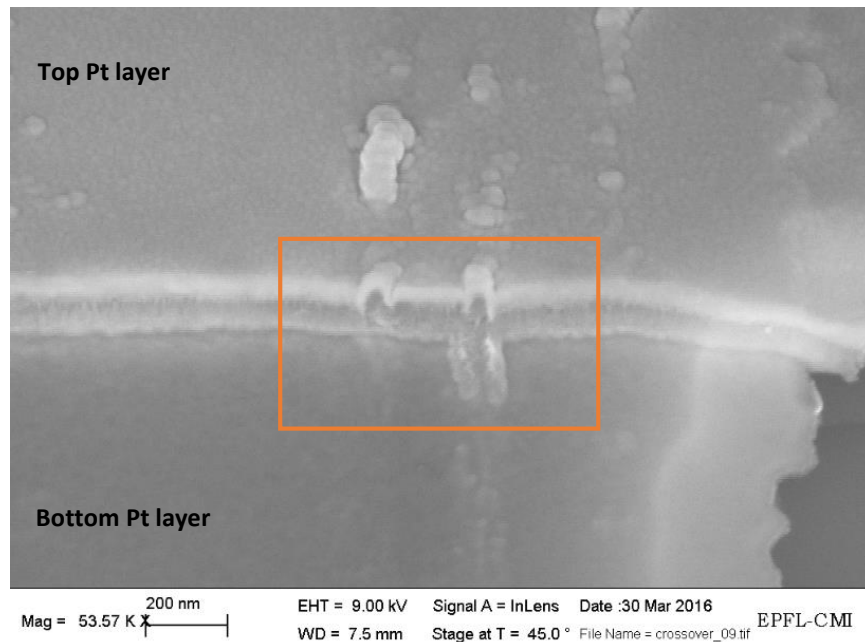


Figure 49: SEM image showing unwanted material connecting top and bottom platinum layers

4.1.3.2. *Methods Implemented*

Multiple methods were implemented to tackle the problem of conduction between platinum layers caused due to the presence of high fences at the bottom platinum layer. Some of them are explained below. At the end, we had to modify the process flow to achieve electrical insulation between the platinum layers.

(a) Ultrasound Treatment:

Ultrasound baths are used for cleaning of wafers by removing any unwanted material particles. Shock waves provide sound energy to cleaning solution that physically removes the particles even at the deepest or least accessible places. However, high power ultrasound treatment can damage the fragile parts of the wafer. After etching in IBE, wafers were put in ultrasound bath for 5 minutes in order to make the fences to fall down from the sides of bottom platinum layer due to the physical force of ultrasound and washed away in the bath solution. It was observed that ultrasound treatment did not have any significant effect on the fences.

(b) Etching in STS Multiplex:

Etching in IBE is a pure physical process where the high energy argon ions bombard the target and remove the material. STS is a Reactive Ion Etching (RIE) system where chemically reactive plasma is used to etch the material. Fences were expected to be avoided by etching platinum layer in STS due to reactive etching but it was observed that it wasn't possible to completely avoid the formation of fences even by STS. Fences generated by STS were smaller than IBE but high enough to possibly cause the device failure as shown in Figure 50.

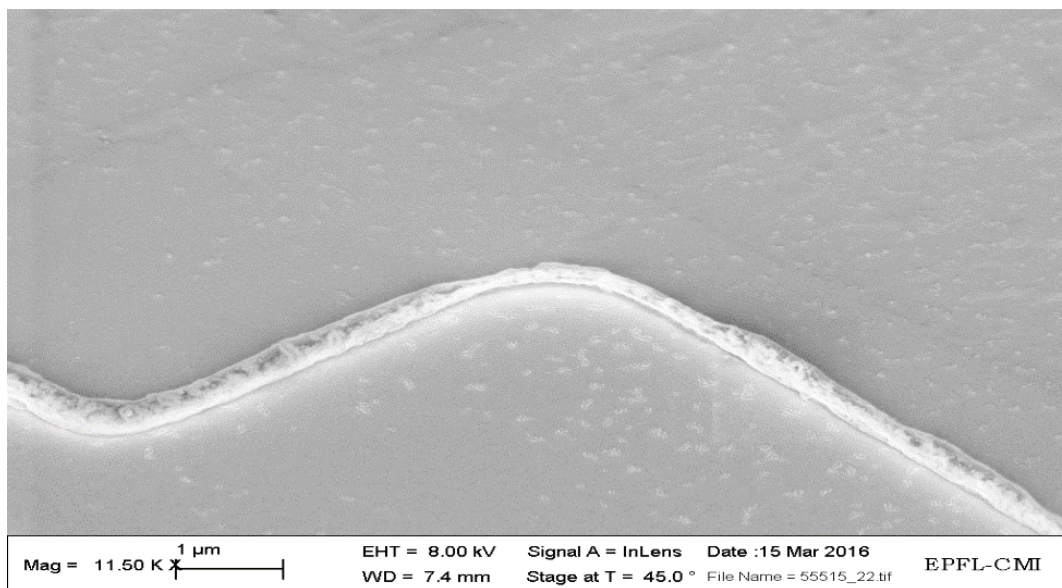


Figure 50: Formation of fences after etching platinum layer in STS

(c) Wet Etching in Aqua Regia:

Aqua Regia is a very strong acid which consists of a mixture of three volumes of hydrochloric acid and one volume of nitric acid used for the etching of noble metals such as Au, Pt etc. Wet etching of platinum was done in aqua regia to avoid the formation of fences. Although wet etching is an isotropic techniques and gives poor control over the etching process of multilayer structures but still the bottom platinum layer on one of the wafer was etched using aqua regia with silicon dioxide as a mask layer. It was observed that after sometime oxide mask started to get cracked and etched out along with platinum as shown in Figure 51.

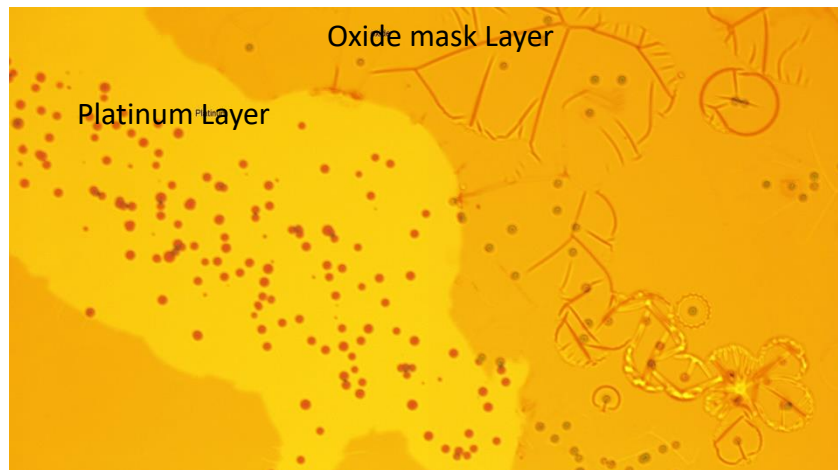
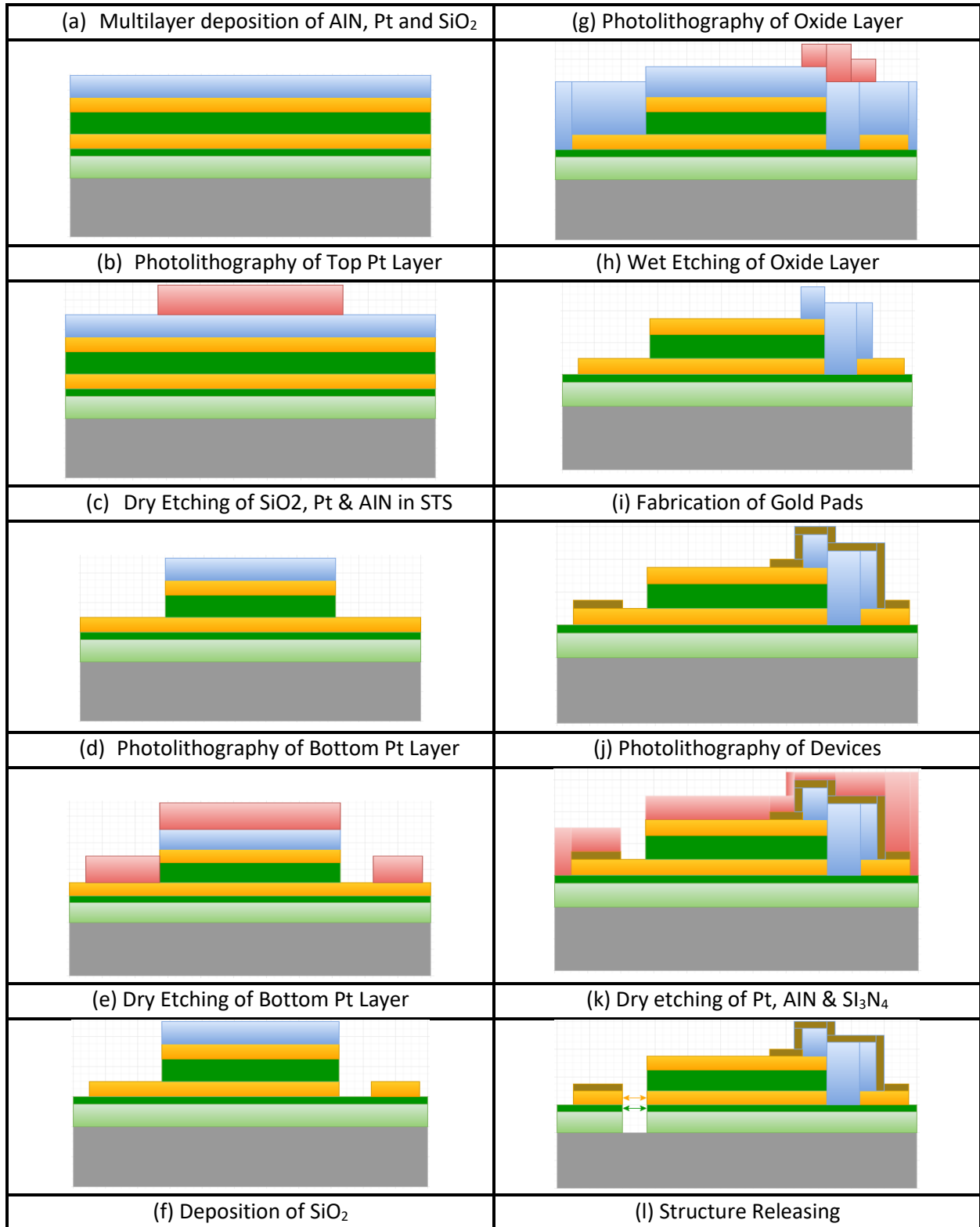


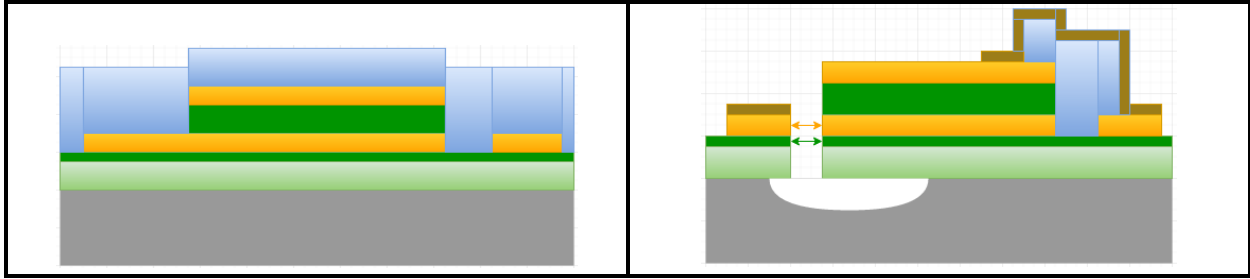
Figure 51: Underneath Pt layer has been exposed after unwanted etching of mask layer

(d) Modification in process flow:

Maintaining electrical insulation when the top platinum layer step's over the bottom platinum layer was a very challenging step of this process flow. In order to avoid this step, the process flow was modified by developing SiO₂ bridges that connected the top platinum layer with its contact pad and later gold lines were fabricated by using lift off to make the electrical connection between top platinum layer and its contact pad by passing over the oxide bridge. In this way the desired electrical insulation between the platinum layers was achieved and cantilevers/double clamped beams were successfully fabricated.

4.2. Second process flow





Note:

The arrows indicate that AlN/Pt layers are connected out of present section plane.

Legend:



SiO₂ Layer

AlN Layer

Pt Layer

PR Layer

Si₃N₄ Layer

Gold Layer

4.2.1. Mask Design

CleWin 4 was used to design the proposed mask. The designed mask consisted of five layers. Figure 52 shows the first and second mask layers that were used to pattern the top and bottom platinum layers respectively. After patterning the top platinum layer with the square pattern shown in Figure 52(a), the area around squares was etched down to the bottom platinum layer and the squares on the wafer represents the whole layer stack (seed, bottom Pt, AlN and top Pt layers). After this, the bottom platinum layer was patterned and etched down to the seed layer. The squares in second mask layer were used to pattern the contact pads for the top platinum layer.

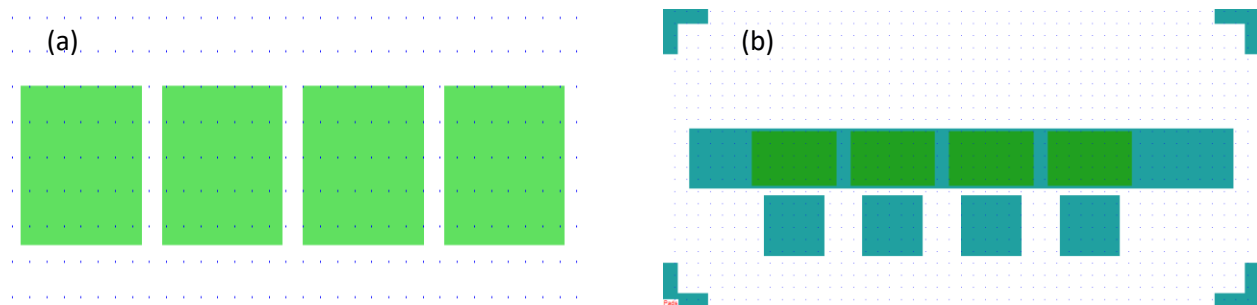


Figure 52: (a) First mask layer for patterning of top platinum layer; (b) Second mask layer for patterning of bottom platinum layer

The third mask layer was used to fabricate SiO₂ bridges between the top platinum layer and its contact pads as shown in Figure 53(a). SiO₂ bridges were not only used as structural material to support gold lines but also to avoid unwanted electrical connection between the gold lines and

bottom platinum layer. Figure 53(b) shows the fourth mask layer that was used to make contact pads for top and bottom platinum layers. As different top platinum squares are on the same bottom platinum layer so only one contact pad on bottom platinum layer was enough to provide potential to all the devices whereas different squares had their separate contact pads for providing potential to top platinum layer.

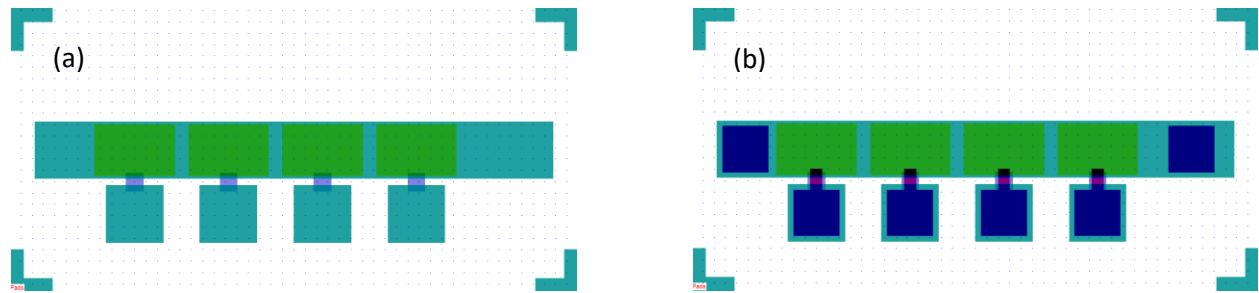


Figure 53: (a) Third mask layer for patterning of SiO₂ bridges; (b) Fourth mask layer for patterning of contact pads

The fifth mask layer was the device layer which consisted of cantilevers and clamp-clamp beams of different dimensions as shown in Figure 54. The dimensions of the devices ranges from 2x1 μ m to 50x5 μ m. The devices were patterned only on the four layers stack squares and were etched down all the way till the surface of the wafer in order to make the openings which were later used for releasing the devices.

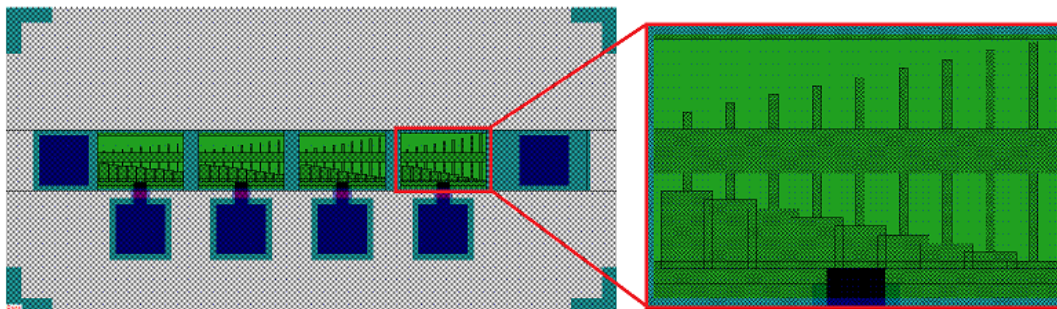


Figure 54: Fifth mask layer for patterning of devices on top platinum layer

4.2.2. Experimental work

(a) Multilayer deposition of AlN, Pt and SiO₂:

Three 4'' wafers (63673, 63674 & 63675) were used for the fabrication of this process flow. These wafer were already coated with 50nm of high stress silicon nitride layer in order to minimize the overall compressive stress in the structure. The wafers were coated with the whole layer stack

including seed (AlN) layer, bottom Pt layer, active (AlN) layer, top Pt layer and oxide layer. A sputtering tool (SPIDER) was used to deposit all the layers in one run with the deposition parameters mentioned in Table 9. Table 14 shows the optimized deposition rates and the time required to achieve the desired thicknesses.

Table 14: Deposition rates and time of different layers for SPIDER

Layers	Deposition rate (nm/min)	Required Layer Thickness (nm)	Deposition Time (s)
AlN (seed)	50	15	18
Pt (bottom)	250	25	6
AlN (active)	50	50	50 & 10
Pt (top)	250	25	6
SiO ₂	20	50	150

(b) Patterning of top and bottom Pt layers:

After deposition, the wafers were coated with 1µm of AZ ECI 3007 positive photoresist and was exposed with MLA 150 tool. Figure 55 shows the first mask design layer that was used to pattern top platinum layer. The area around the patterned squares was etched down to the bottom platinum layer by using STS Multiplex. The etching was done in multiple steps for the duration of 95s until bottom platinum layer was exposed. The photoresist was stripped off and a new layer of 1µm AZ ECI 3007 was coated for the patterning of bottom platinum layer using second mask layer as shown in Figure 56. Again STS multiplex was used to etch the bottom platinum layer down to the seed layer.

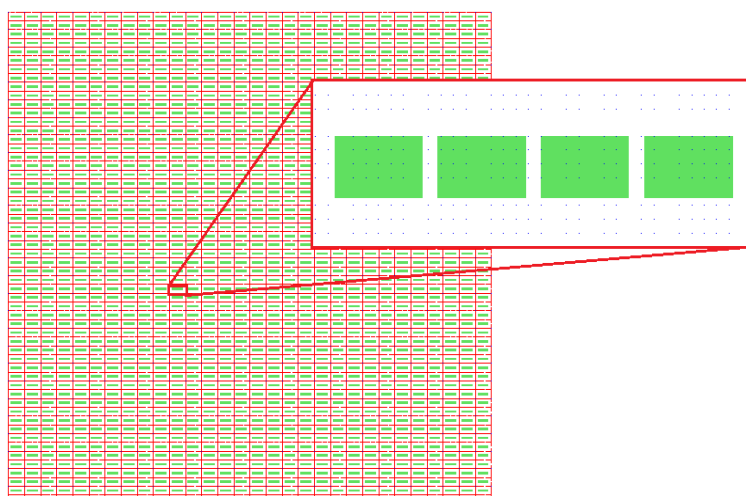


Figure 55: First mask design layer to pattern top Pt layer

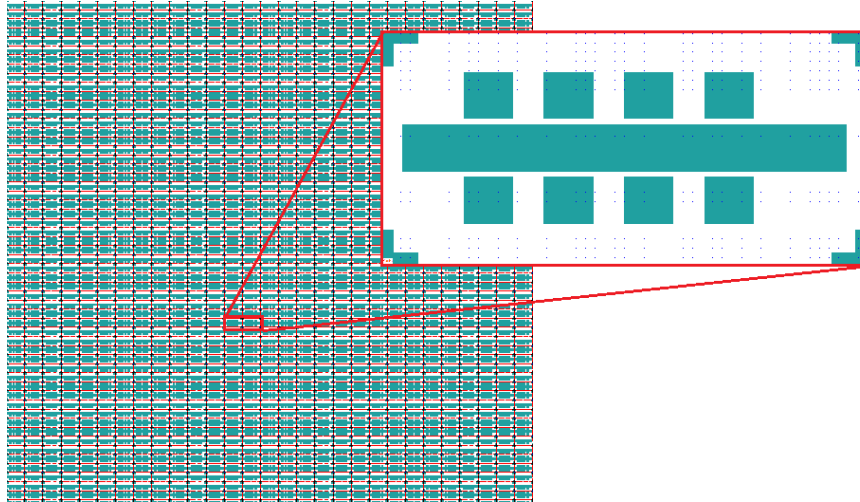


Figure 56: Second mask layer for patterning of bottom Pt layer

(c) Fabrication of SiO₂ bridges:

Fabrication of SiO₂ bridges was the most critical step of this process flow. The purpose of SiO₂ bridges was to make a path between the top platinum layer and its contact pads. 100nm of SiO₂ layer was deposited by SPIDER and patterned by MLA 150. Figure 57 shows the third mask layer, which was used to pattern oxide layer. Buffered hydrofluoric acid (BHF) was used to etch the unprotected areas of oxide layer and at the end of etching, 65x60μm dimension of oxide patches were left in between the top platinum layer and its contact pads as shown in Figure 58. Later gold lines were fabricated to make an electrical connection between the top platinum layer and its contact pads.

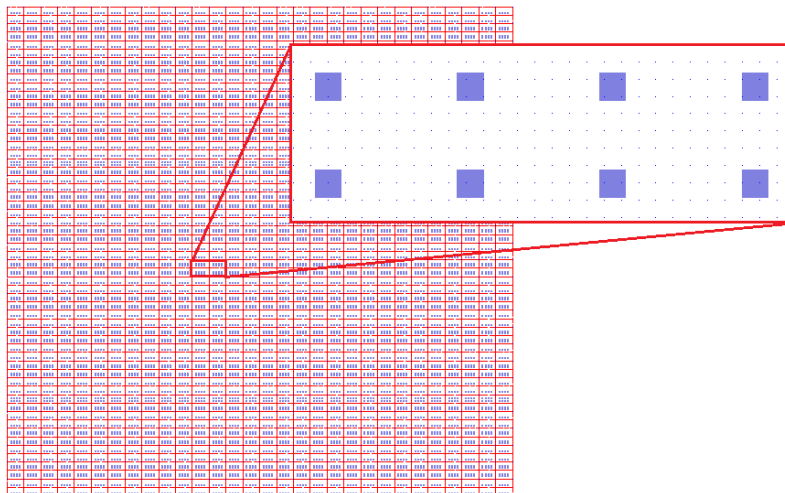


Figure 57: Third mask layer for patterning of SiO₂ bridges

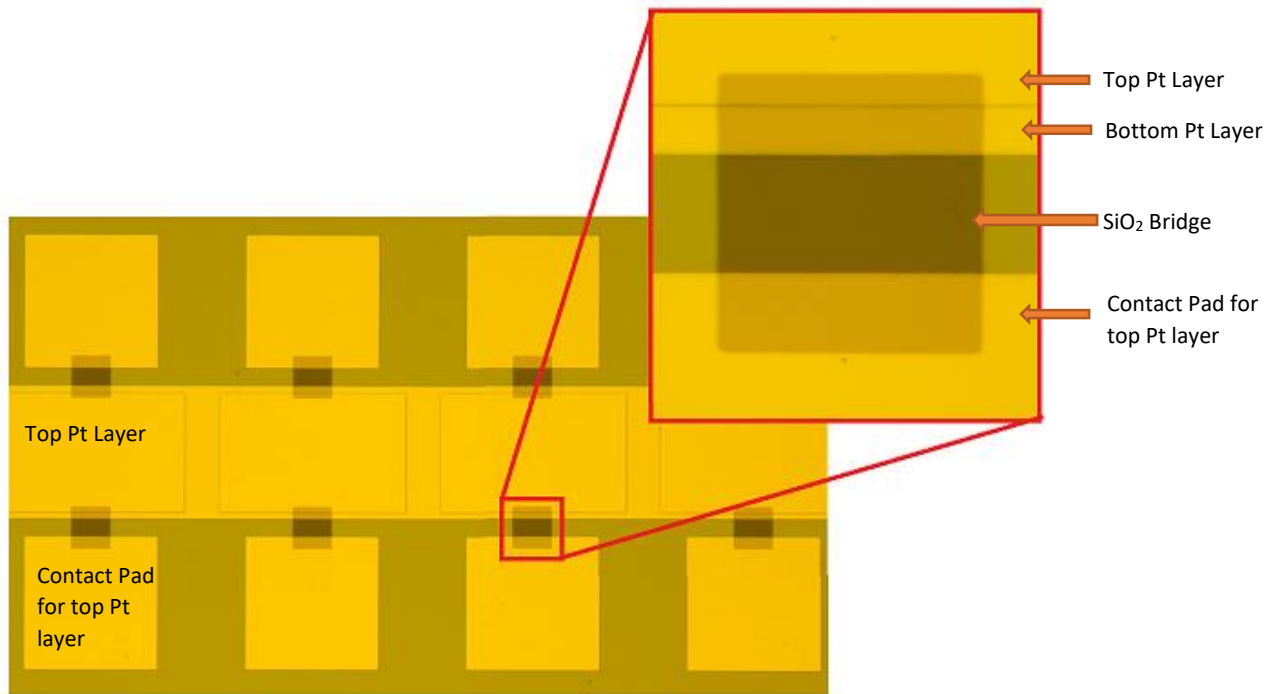


Figure 58: Fabrication of SiO₂ bridges for electrical insulation between different layers

The purpose of SiO₂ bridges was to act not only as a structural support to hold the gold lines but also to provide complete electrical insulation between the gold lines and bottom platinum layer. In Figure 58, SiO₂ bridges are passing over the bottom platinum layer and then connecting with the top platinum layer. If the bridges get broken at the crossover point, then there is a very high probability that gold line will get in contact with the bottom platinum layer and will cause short circuiting of top and bottom platinum layers. So it is essential to have well defined and uniform oxide bridges. Figure 59 shows few examples of poor oxide bridges due to over etching of SiO₂ layer in BHF. Broken bridges can be seen from the sides which could possibly leads to the conduction between top and bottom platinum layers.



Figure 59: Broken SiO₂ bridges due to over etching of SiO₂ layer in BHF

(d) Fabrication of gold contact pads:

Gold contact pads were used to probe the top and bottom platinum layers. Contact pads were fabricated by using gold lift off and wire bonded to the terminals of PCB where the voltage was supplied for biasing of platinum layers. Lift off is a process of creating structures of a target material on the substrate by using sacrificial material layer. First an inverse pattern is created on the sacrificial layer in order to make openings for the target material to reach the substrate surface and then whole wafer is deposited by the target material. The target material is deposited on top of sacrificial layer except in the regions where the sacrificial layer was etched away. By removing the sacrificial layer, the target material on top of sacrificial layer is also lifted off and washed away with the sacrificial layer and well defined structures of target material are left on the substrate. LOR is a high resolution resist which is used either as sacrificial layer or as an undercut layer in the lift off process. Figure 60 illustrates the steps involved in the lift off process.

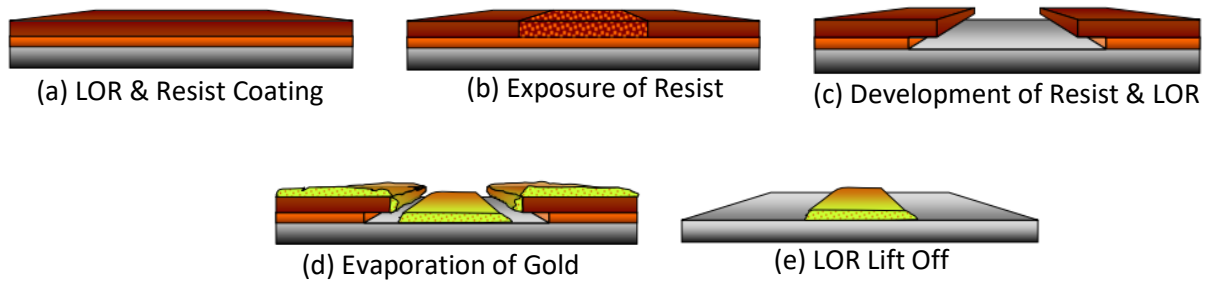


Figure 60: Illustration of the liftoff process

The wafers were first coated with bi-layer of LOR and AZ 1512 resist in ACS200. Table 15 shows the coating parameters that were used to coat 0.48 μm of LOR 5A and 1.1 μm of AZ 1512 HS positive photoresist in ACS200. LOR is not a photosensitive resist, so in order to pattern LOR a separate photosensitive resist (AZ 1512) was used. MLA 150 was used to expose the bi-layer resist with dose 65mJ/cm² and defocus of -6. Figure 61 shows the fourth mask layer which consists of contact pads and the gold lines for connecting top platinum layer with its contact pads.

Table 15: Parameters for coating of LOR and AZ 1512 in ACS200

Resist Type	Spin Speed (rpm)	Cure Time (mm:ss)	Achieved Thickness (μm)
LOR 5A	4500	04:10	0.48
AZ 1512 HS	6000	02:00	1.1

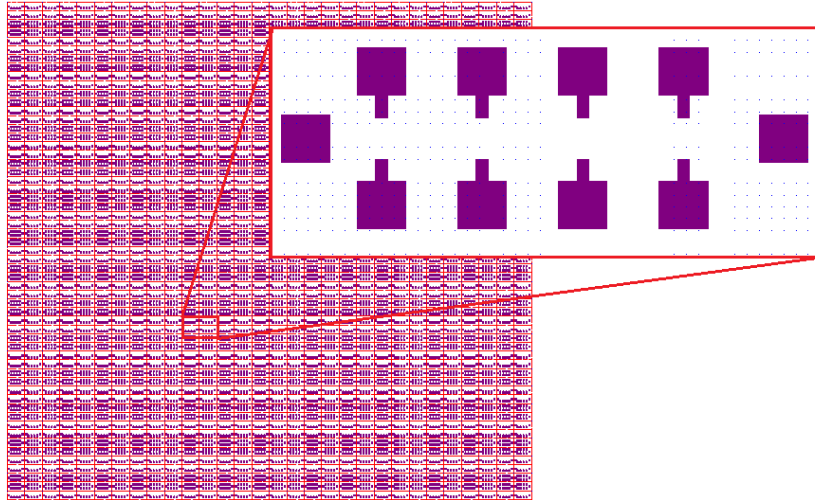


Figure 61: Fourth mask layer for patterning of gold contact pads

Development of photosensitive resist makes an opening for the etching solution to attack LOR and etch it away. Undercuts in LOR layer was observed due to isotropic etching. AZ 426 MIF solution was used for the development of both the resist layers. After development, baking was done at 100 °C for 2 minutes to improve the stability of photoresist. Figure 62 shows the photolithography results where contact pads have desired openings in the LOR layer for gold deposition.

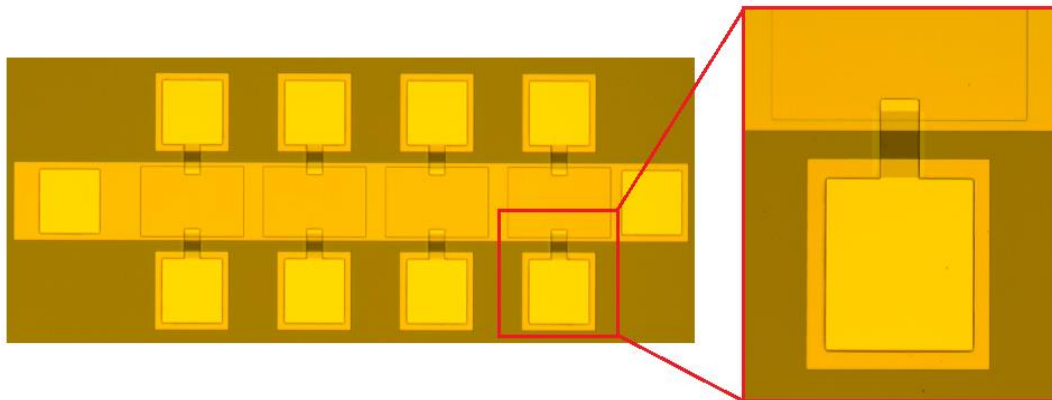


Figure 62: Photolithography of contact pads for gold deposition

100nm of gold layer was deposited on the wafers by using an evaporation tool (Leybold Optics Lab 600H). Lab 600H uses e-beam evaporation where electron beam is used to evaporate the metal. A high energy electron beam is directed towards the crucible containing gold. The kinetic energy of the electrons is converted into heat upon impact to evaporate gold. Distance between the source and target is very important for liftoff process. The distance of 1.010m was maintained between the source and target in order to maintain angle at 90° between the wafers and the incident flux. Figure 63 shows the surface of wafer after gold deposition.

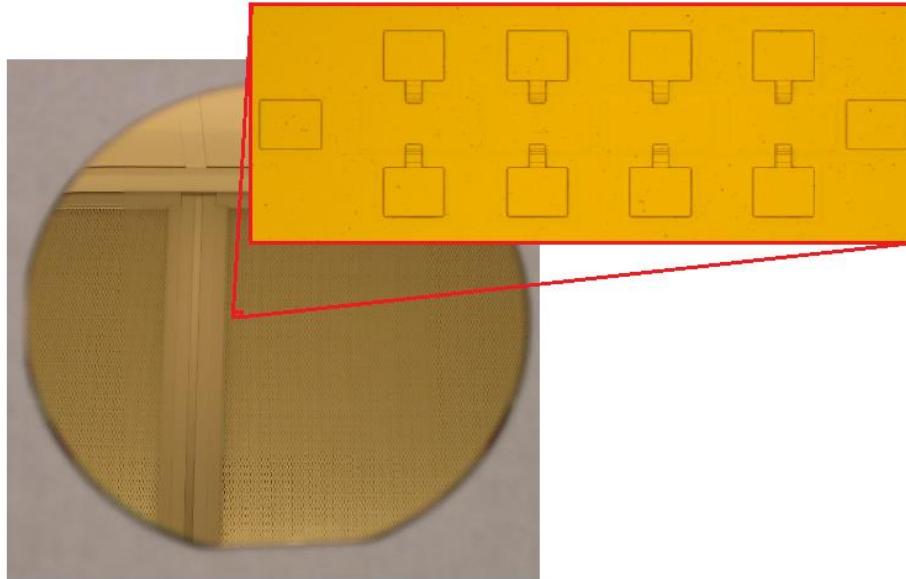


Figure 63: After 100nm of gold deposition

After the deposition of gold, Plade Solvent wet bench was used to remove the remaining LOR to produce well-defined gold pads on the wafer. Plade Solvent wet bench consists of two lift off baths containing NMP (Remover 1165) for dissolving LOR. Ultrasonic wave generator was used in one of the bath to speed up the stripping process. Wafer were put in ultrasonic bath for 5min and then left for the whole day in the static bath. After the completion of gold lift off, the wafers were put in isopropanol (IPA) solution for 1min and rinsed properly in water. Figure 64 & Figure 65 shows gold pads and the gold lines passing over the oxide bridges and connecting with the top platinum layer.

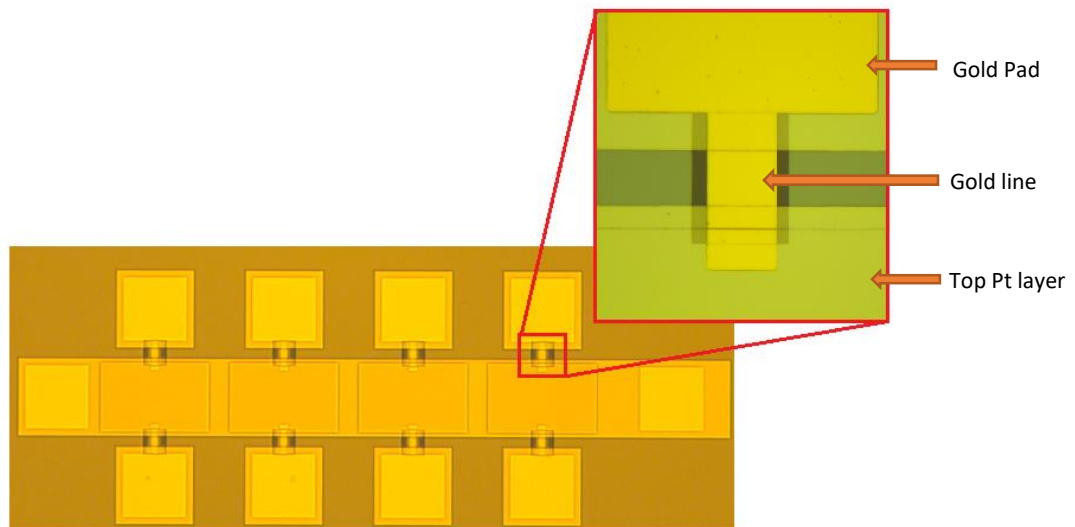


Figure 64: Fabrication of gold pads and lines for the electrical connection with the top Pt layer

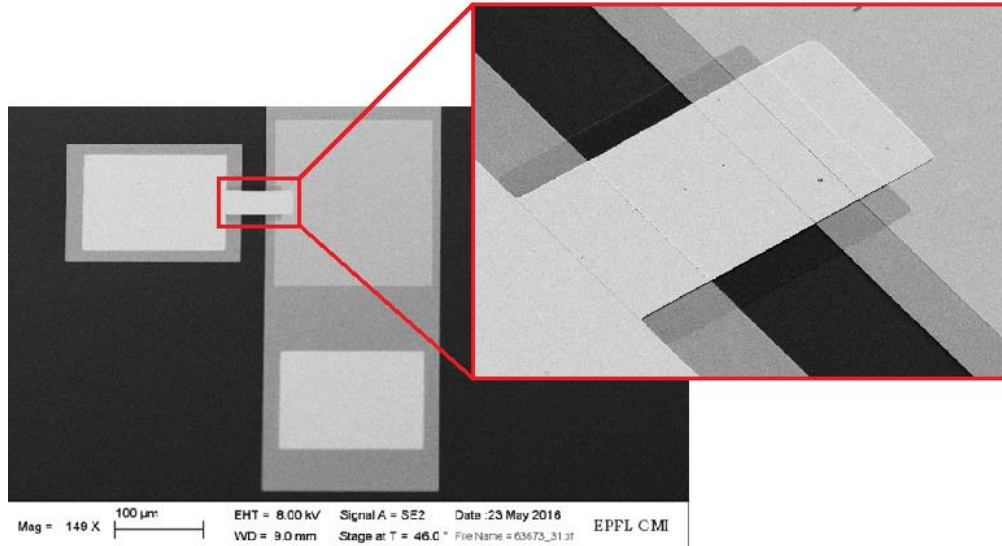


Figure 65: Gold line passing over the oxide bridge

(e) Fabrication and release of devices using BOSCH process:

The fourth and the last photolithographic step was done for the patterning of cantilevers and doubly clamped beams of different lengths. Exposure parameters were carefully optimized in order to get well-defined structures. MLA 150 was used with does $112\text{mJ}/\text{cm}^2$ and defocus of -8 for the exposure of fourth mask layer as shown in Figure 66. Once the devices were patterned, the etching was done using STS Multiplex all the way to the surface of the wafer in order to make the openings around the cantilevers and beams for releasing the structures.

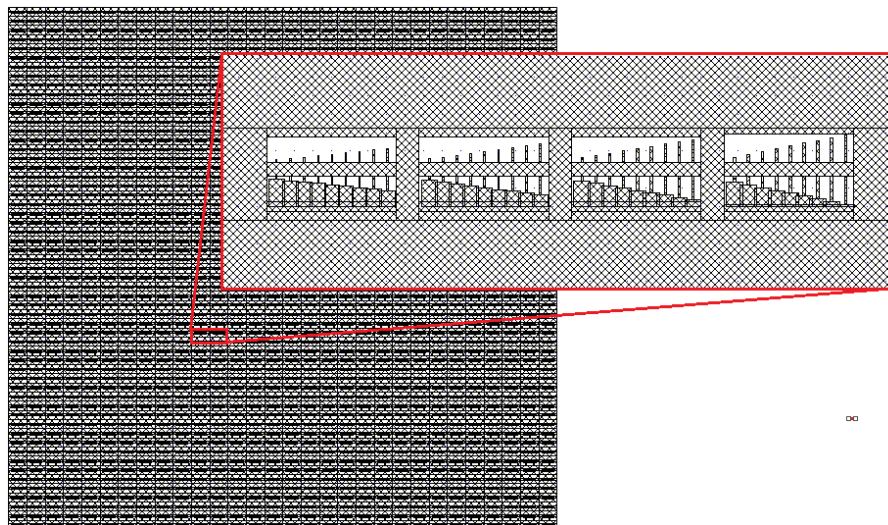


Figure 66: Fourth mask layer for the patterning of devices

Once the devices were etched all the way to the wafer surface, the next step was to etch the silicon. Alcatel 601E was used to etch silicon anisotropically using Bosch process. Alcatel 601E is a Deep Reactive Ion Etching (DRIE) system which uses fluorine based chemistry to etch silicon along with fluorocarbon plasma for side wall passivation. Sulphur hexafluoride (SF_6) gas was used for the isotropic etching of silicon whereas side wall passivation was done using Octafluorocyclobutane (C_4F_8) gas. A complete etch process cycles between etching and passivation multiple times in order to achieve deep and vertical etch profiles.

Silicon was etched by using Bosch process in Alcatel 601E for 3 minutes with the etch rate of $5\mu\text{m}/\text{min}$ in order to make $15\mu\text{m}$ deep cavities inside the wafer. Figure 67 shows devices after etching silicon using Bosch process. At this stage, the structures were not released because the Bosch process etches silicon anisotropically and there was still some silicon left underneath the structures.

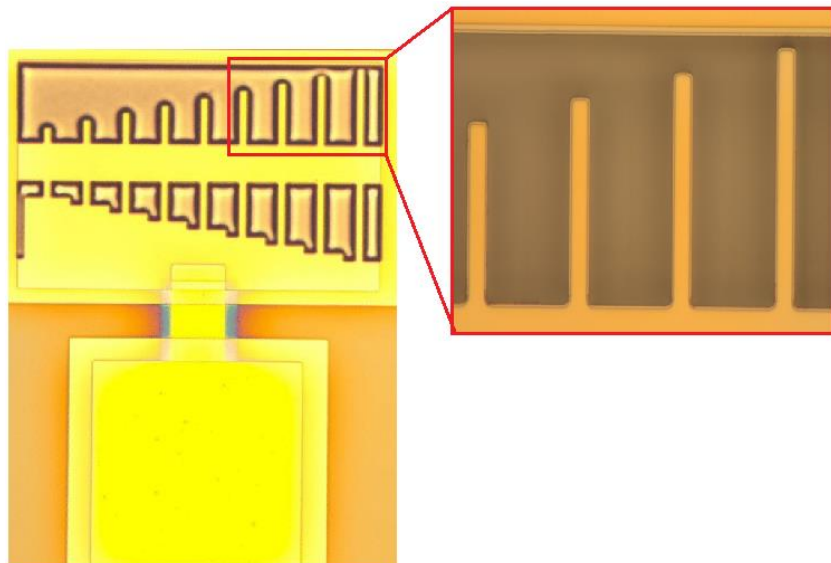


Figure 67: Anisotropic etching of silicon using Bosch process

Once the cavities were made around the cantilever and beams, SF_6 gas was used to isotopically etch silicon from underneath the structures. SF_6 etches silicon with the etch rate of $6\mu\text{m}/\text{min}$ in Alcatel 601E. The widest cantilever/beam was $6\mu\text{m}$ which requires approximately 30s to etch the underneath silicon because gas etches from all the sides. The etching was done for 1 minute in order to fully release the structures as shown in Figure 68.

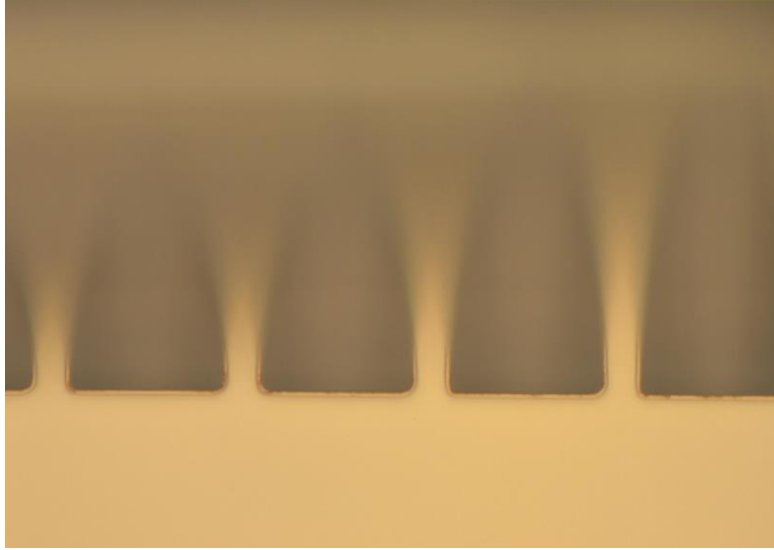


Figure 68: Cantilever tips are out of focus due to bending downwards

Figure 69 & Figure 70 shows SEM images of the cantilevers and double clamped beams. The structures are completely released and the cavity is deep enough to refrain cantilever tips from touching the ground.

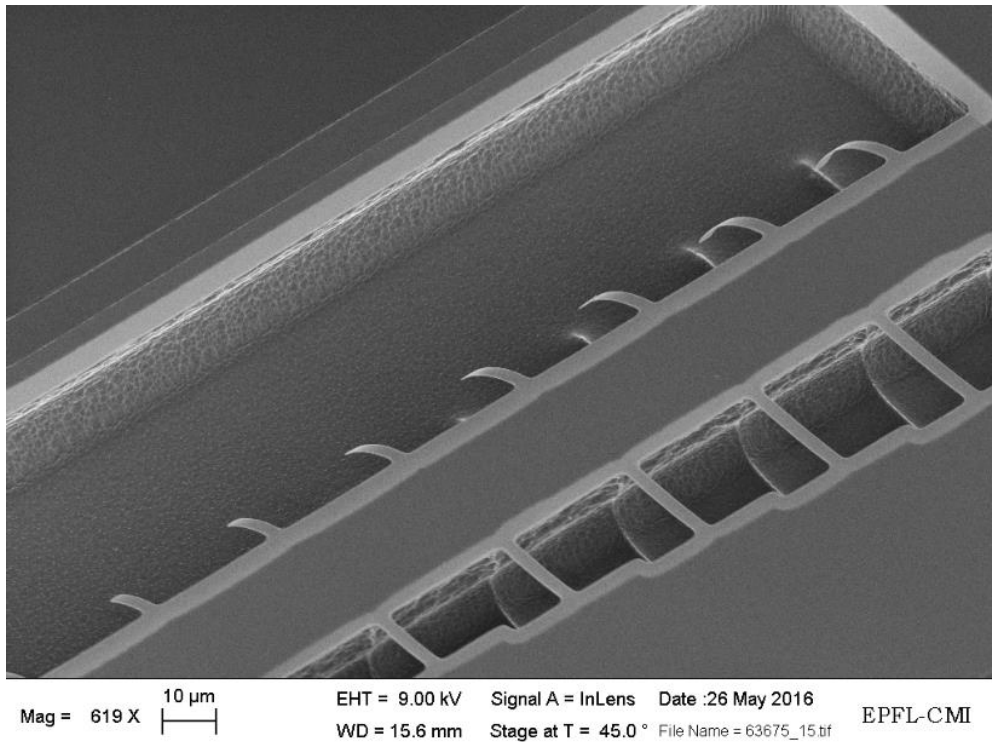


Figure 69: SEM image showing etched cavity and released cantilevers and doubly clamped beams

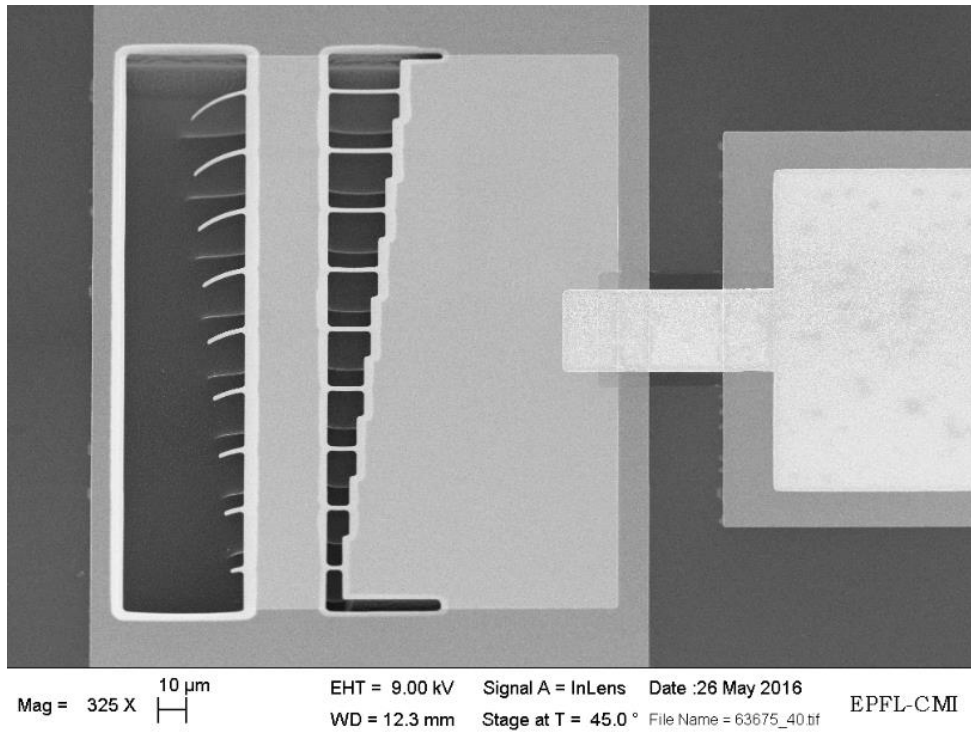


Figure 70: SEM image of released devices

The light grey color on the edges of the anchored platform is due to the over etching of silicon from underneath the platform as shown in the Figure 71.

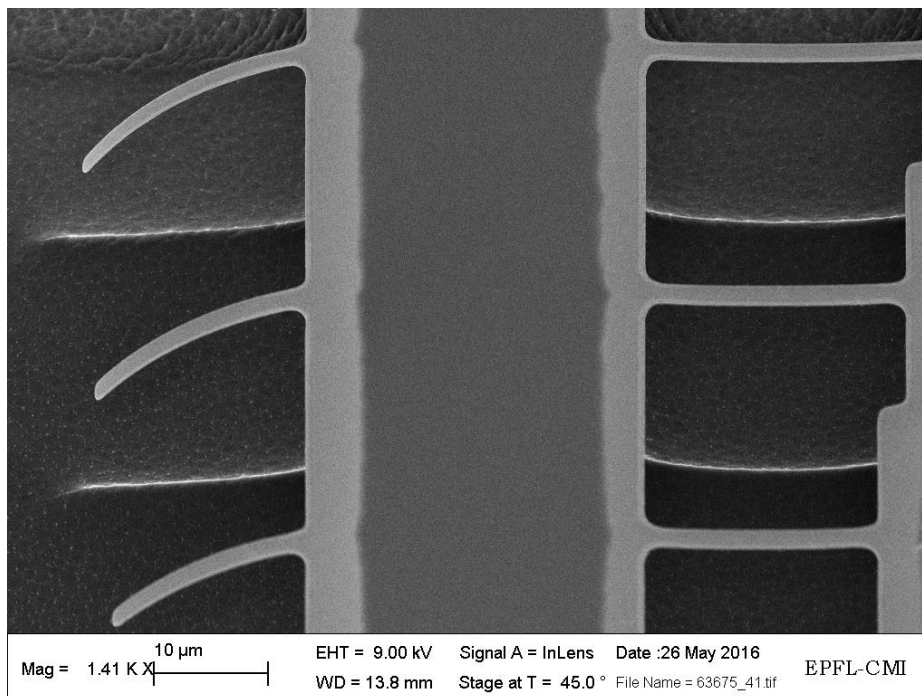


Figure 71: Over etching of silicon from underneath the anchored platform

4.2.3. Discussion

Generation of residual stress during thin film deposition is a well-known phenomenon. It is very important to control the factors that generate residual stress since it has huge influence on the mechanical properties of the material. Large residual stresses are generated during film deposition due to intrinsic or thermal stress produced by the mismatch between thermal expansion and contraction of the film and the substrate. Intrinsic and extrinsic are the main two types of stresses generated in the films. Intrinsic stress is generated due to defects or dislocations in the films, whereas extrinsic stress comes from the adhesion of film to the substrate. During film deposition, extrinsic stress is generated due to the difference in coefficient of thermal expansion or the lattice misfit between the substrate and the film.

A stress measurement tool (Toho Technology FLX 2320-S) was used to measure the residual stress generated during deposition of a multilayer stack of thin films. FLX 2320-S determines stress by measuring the change in curvature of the wafer before and after the deposition of a thin film. The difference in curvature is used to calculate stress by using Stoney's equation.

$$\sigma = \frac{E_s}{6(1 - \nu_s)} \frac{h_s^2}{h_f} \left(\frac{1}{R} - \frac{1}{R_0} \right) \quad (6)$$

where E_s is the Young's modulus, ν_s is the Poisson's ratio, h_s and h_f are thicknesses of the substrate and the film, and R and R_0 are the radius of curvature of the substrate after and before deposition, respectively.

A laser beam is directed on the surface with a known spatial angle in order to measure the curvature of the wafer. The reflected beam is detected by a position-sensitive photodiode, and the surface of the wafer is scanned in order to record the geometry of the film, as shown in Figure 72. Table 16 shows residual stresses generated during thin film deposition in SPIDER and the effective stress value measured from Toho Technology FLX 2320-S.

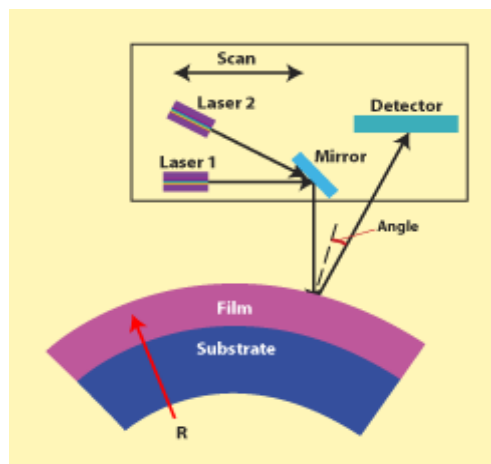


Figure 72: Working principle of Toho Technology FLX 2320-S

Table 16: Calculated stress values for individual layers and the overall stress measured by Toho Technology FLX 2320-S

Layers	Thickness (nm)	Stress (MPa)
Silicon nitride	50	1127.40
Seed AlN Layer	15	-4016.3
Bottom Pt Layer	25	786.068
Active AlN Layer	50	-1268.92
Top Pt Layer	25	786.07
Overall Effective Stress	165	-169.80

The downwards bending of the cantilevers can be explained due the presence of overall compressive stress in the structures. The same behavior was simulated using ANSYS Multiphysics. The multilayer cantilever beam of 60x6 μ m dimensions was simulated under the influence of material stress without apply any force or voltage across the piezoelectric layer. Figure 73 shows the simulation results of bending of the cantilever due to the presence of overall compressive stress.

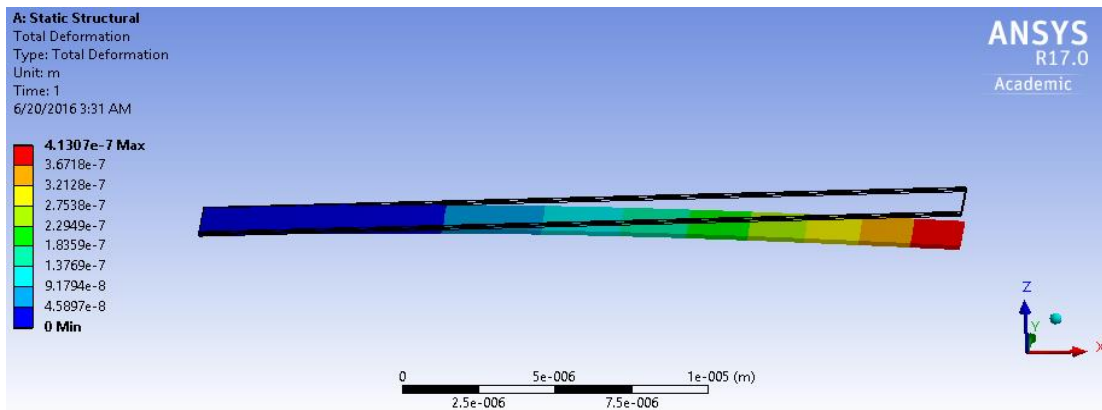


Figure 73: Simulation of cantilever with material stress in ANSYS Multiphysics

By implementing this process flow, we were successfully able to solve the problem of conduction between top and bottom platinum layers. Rigorous testing was done using probe station in order to measure the resistance between the platinum layers and the resistance always stayed in G/Mohms range. However, it was expected to have high compressive stress in the structures due to ultra-thin films. Use of silicon nitride (Si_3N_4) layer instead of thermal oxide on the surface of wafer was to intentionally introduce tensile stress in the structure in order to reduce the overall compressive stress. With the further optimization of SPIDER deposition parameters for AlN films and by implementing techniques like thermal annealing can help in further reducing the overall

stress in the structures. Figure 74 shows the SEM image of multilayer piezoelectric NEMS resonators.

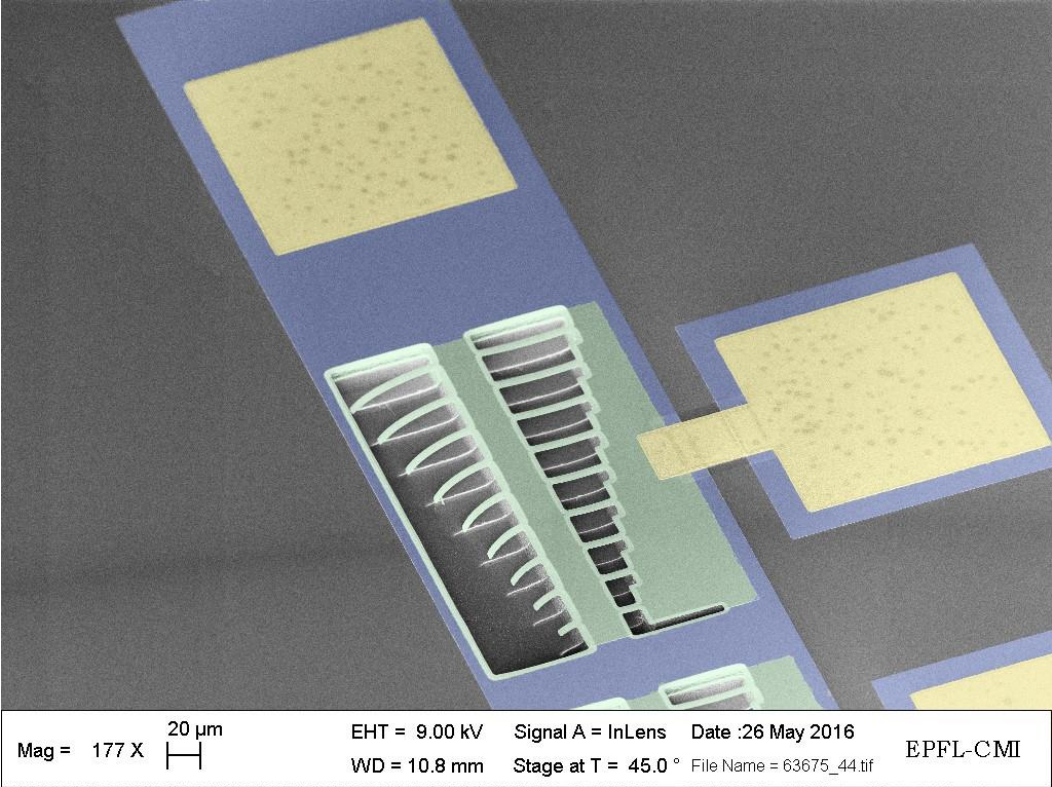


Figure 74: Fabricated multilayer piezoelectric resonators

4.3. Resonance frequency measurements

After the successful fabrication of devices, the wafers were cleaved into small chips of 1.5x1.5cm dimensions. A PCB was specially designed for mounting the chips and providing voltage to the contact pads of top and bottom platinum layers. Silver paste was used to fix the chips on PCB and wire bonding was done to make electrical connection between the contact pads of the PCB and the platinum layers as shown in Figure 75. PCB terminals were used to provide DC or AC signal for the DC or AC analysis of the devices respectively.

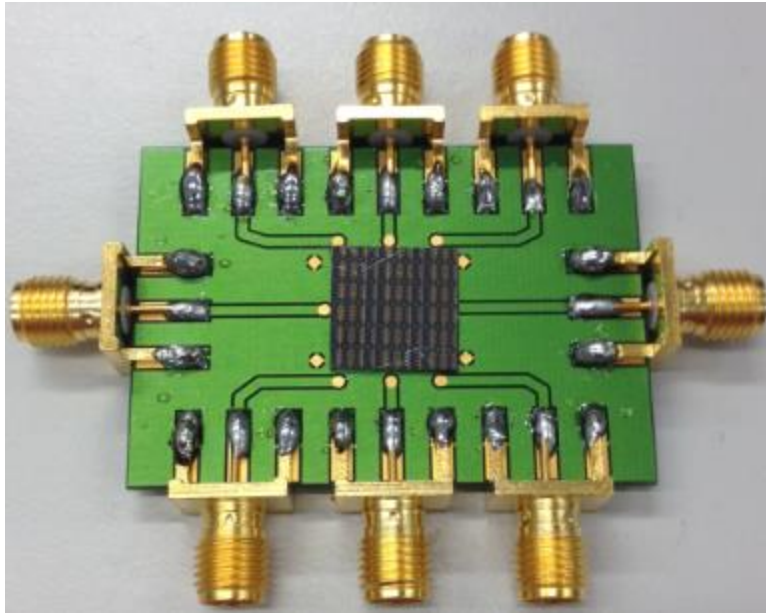


Figure 75: PCB mounted and wirebonded with the chip for providing voltage signal to the resonators

Laser Vibrometer MSV-400 was used to measure the frequency of the resonating devices. MSV-400 is a non-contact vibration measuring device based on the principle of Doppler shift where a laser beam is directed on the surface of the vibrating device and the resultant amplitude and resonance frequency is measured with the help of fringe patterns generated due to the interference of laser beam reflected from the surface of the device and the beam reflected from the reference mirror. It consists of Laser Doppler vibrometry for measuring out of plane vibrations and stroboscopic video microscopy for measuring in-plane displacement parallel to the surface of the device.

After wire bonding, the devices were provided with an AC signal of 10mV and the resonance frequency was measured. Figure 76 shows the measured frequency response of 60x6 μ m cantilever. The maximum vibration amplitude was achieved at 400 KHz which dictated the resonance frequency of the cantilever. It must be noted that only the resonance frequency of longest cantilevers was measured because as the cantilever length reduces the resonance

frequency increases and in our case most of the cantilevers had resonance frequencies shifted in MHz range and MSV-400 cannot measure vibrations higher than 1 MHz.

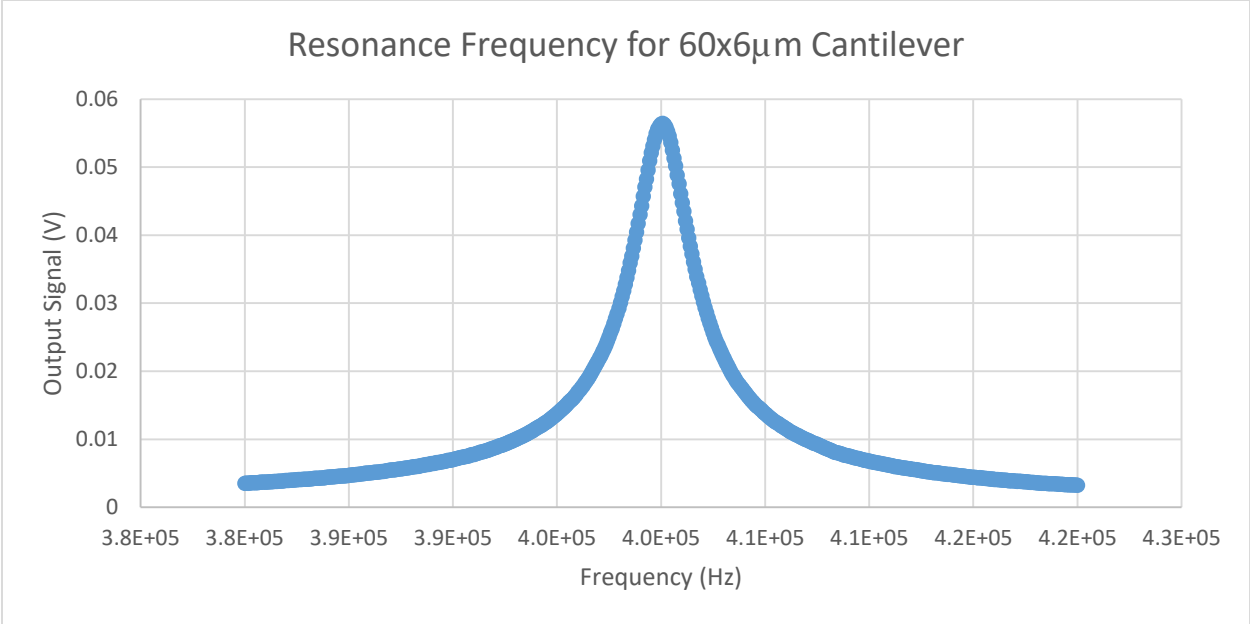


Figure 76: Resonance frequency of 60µm long cantilever measured with Laser Vibrometer MSV-400

As mentioned in the chapter 3, the generation of stress due to applied voltage shifts the resonance frequency of the beam. Similarly, the presence of material stress also has a significant effect on the natural frequency of the beam. It is believed that the huge difference in the measured and the simulated resonance frequency of 60µm long cantilever is due to the presence of high compressive material stress in the structures and there is also a possibility that the cantilever tip was touching the ground during frequency measurements.

5. Conclusion

Successful fabrication of multilayer piezoelectric NEMS resonators was achieved by the selection of appropriate materials and optimization of different fabrication steps. Two different process flows were implemented for the fabrication of multilayer cantilevers and doubly clamped beams. Maintaining electrical insulation between ultra-thin platinum layers was a huge challenge due to the presence of high fences after dry etching of platinum layers. We believe that the crossover region (Figure 47) where the top platinum layer stepped over the bottom platinum layer was the possible cause of conduction between the platinum layers. This problem was avoided by covering the crossover region with the insulating material such as SiO₂. SiO₂ bridges were fabricated for supporting the gold lines for the electrical connection between the top Pt layer and its contact pad (Figure 65). This way the desired electrical insulation was achieved.

Aluminum nitride thin film was deposited by DC pulsed magnetron sputtering. The quality of AlN crystals and generation of residual stress was highly dependent on the deposition conditions. A complete set of test wafers were prepared in order to find out the appropriate deposition conditions for achieving well textured growth of AlN film. XRD and stress analyzer was used for crystallinity and material stress measurements. Apart from having good piezoelectric properties, AlN should also act as a very good insulating material. 50nm thin film of AlN was sandwiched between top and bottom platinum layers to provide desired electrical insulation. Probe station was used to measure the conduction between the platinum layers. Dielectric breakdown and physical rupturing of the layers due to high electrical stress was experienced during the conduction measurements. It was observed that when the applied voltage was increased more than 5V then due to the generation of high electrical stress the top Pt layer got severely damaged as shown in Figure 77. As the applied voltage exceeded the threshold voltage, the cracks started to appear on the top Pt layer and the insulation resistance between top and bottom Pt layers was abruptly drop to few Ohms.

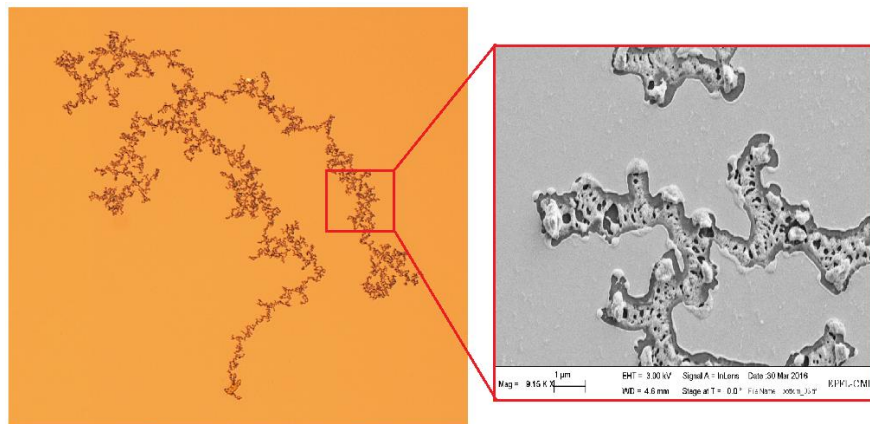


Figure 77: Appearance of cracks on the top platinum layer when voltage was exceeded the threshold limit. SEM image on the right shows the rupturing of layers

Presence of high compressive stress in the AlN layer was responsible for the downwards bending of the cantilever beams. The variation in the resonance frequency of simulated and measured values for 60 μ m long cantilever beam was due to the touching of cantilever tip with the surface of the wafer during resonance frequency measurements. In future, we further need to optimize the deposition parameters for AlN thin film and implement techniques like thermal annealing in order to reduce the overall residual stress in the structures.

6. References

- [1] J. Ma, "Advanced MEMS-based technologies and displays," vol. 37, pp. 2–10, 2015.
- [2] J. Wang and X. Qian, "Application and Development of MEMS in the Field of Aerospace," vol. 643, pp. 72–76, 2014.
- [3] P. F. Partnership, "Prime Faraday Technology Watch An Introduction to MEMS (Micro-electromechanical Systems)," no. January. 2002.
- [4] G. Villanueva, J. Bausells, and J. Brugger, "Grand challenge in N/ MEMS," vol. 1, no. January, 2016.
- [5] X. F. Zha, "MEMS/NEMS Handbook Techniques and Applications," C. T. Leondes, Ed. pp. 2–32.
- [6] R. P. Feynman, "Plenty of Room at the Bottom," no. December, 1959.
- [7] Nanotechweb review, "Quantum-dot TVs seed a bright future," 2015.
- [8] S. Schmid, L. G. Villanueva, and M. L. Roukes, *Fundamentals of Nanomechanical Resonators*. 2016.
- [9] T. Ono, X. Li, H. Miyashita, M. Esashi, T. Ono, X. Li, and H. Miyashita, "Mass sensing of adsorbed molecules in sub-picogram sample with ultrathin silicon resonator," vol. 1240, no. May, 2016.
- [10] L. Nicu, V. Auzelyte, L. G. Villanueva, N. Barniol, and F. Perez-murano, "Chapter 9: Nanoelectromechanical Systems (NEMS)," in *Resonant MEMS—Fundamentals, Implementation and Application*, 1st ed., O. Brand, I. Dufour, S. M. Heinrich, and F. Josse, Eds. Wiley-VCH Verlag GmbH & Co. KGaA, 2015, pp. 203–231.
- [11] O. Brand and H. Baltes, "Micromachined Resonant Sensors - an Overview." pp. 4–14.
- [12] S. K. Vashist, "A Review of Microcantilevers for Sensing Applications," *AZoNano*, 2007.
- [13] J. Lu, T. Ikehara, Y. Zhang, T. Mihara, T. Itoh, and R. Maeda, "High Quality Factor Silicon Cantilever Driven by PZT Actuator for Resonant Based Mass Detection," no. April, pp. 1–6, 2008.
- [14] K. Jensen, K. Kim, and A. Zettl, "An atomic-resolution nanomechanical mass sensor," *Nat. Nanotechnol.*, vol. 3, no. 9, pp. 533–7, 2008.
- [15] J. Fritz, "Cantilever biosensors," no. i, pp. 855–863, 2008.
- [16] S. Schmid, L. G. Villanueva, and M. L. Roukes, "Chapter 2: Quality Factor," in *Fundamentals of Nanomechanical Resonators*, Springer International Publishing Switzerland 2016, 2016, pp. 57–90.
- [17] M. Nordström, S. Keller, M. Lillemose, A. Johansson, S. Dohn, D. Haefliger, G. Blagoi, M. Havsteen-jakobsen, and A. Boisen, "SU-8 Cantilevers for Bio/chemical Sensing; Fabrication, Characterisation and Development of Novel Read-out Methods," pp. 1595–1612, 2008.
- [18] G. Stemme, "Resonant silicon sensors," *J.micromech.Microeng*, vol. 113, pp. 113–125, 1990.
- [19] A. Park, M. Elwenspoek, and J. H. J. Fluitman, "Selective Mode Excitation and Detection of Micromachined Resonators," *Micro Electro Mech. Syst. '92*, 1992.
- [20] M. Elwenspaek, F. R. Blom, S. Bouwstra, T. S. J. Lammerink, F. C. M. Van de Pol, H. A. C. Tilmans,

- T. J. A. Pappa, and J. H. . Fluitman, "TRANSDUCTION MECHANISMS AND THEIR APPLICATIONS IN MICRO MECHANICAL DEVICES," *Micro Electro Mech. Syst. 1989, Proceedings, An Investig. Micro Struct. Sensors, Actuators, Mach. Robot. IEEE*, pp. 126–132, 1989.
- [21] M. I. Younis, *MEMS Linear and Nonlinear Statics and Dynamics*. 2010.
- [22] M. Elwenspoek and R. Wiegerink, "Mechanical Microsensors," 2000, pp. 222–225.
- [23] J. Lee, C. Li, M. Li, C. Chin, S. Li, and P. X. Feng, "Multimode Characteristics of High-Frequency CMOS-MEMS Resonators," pp. 2–4.
- [24] A. L. Herrera-may, L. A. Aguilera-cortés, P. J. García-ramírez, and E. Manjarrez, "Resonant Magnetic Field Sensors Based On MEMS Technology," pp. 7785–7813, 2009.
- [25] T. Ono and M. Esashi, "Mass sensing with resonating ultra-thin silicon beams detected by a double-beam laser Doppler vibrometer," vol. 15, pp. 1977–1981, 2004.
- [26] B. R. Kumar and V. Jyothi, "Analysis of Mass Based Micro Cantilever Using Comsol," *Int. J. Emerg. Technol. Adv. Eng.*, vol. 5, no. 5, 2015.
- [27] K. Park and R. Bashir, "MEMS-BASED RESONANT SENSOR WITH UNIFORM MASS SENSITIVITY," 2009.
- [28] A. Hajjam and S. Pourkamali, "Fabrication and Characterization of MEMS-Based Resonant Organic Gas Sensors," *IEEE Sens. J.*, vol. 12, no. 6, pp. 1958–1964, 2012.
- [29] A. Touhami, "Biosensors and Nanobiosensors : Design and Applications," pp. 374–403.
- [30] L. A. Beardslee, O. Brand, and F. Josse, "Resonant MEMS Chemical Sensors," in *Resonant MEMS–Fundamentals, Implementation and Application*, 2015, pp. 355–390.
- [31] P. Xu, H. Yu, and X. Li, "Functionalized Mesoporous Silica for Microgravimetric Sensing of Trace Chemical Vapors," *Anal. Chem.* 2011, 83, pp. 3448–3454, 2011.
- [32] B. Ilic, D. Czaplowski, M. Zalalutdinov, H. G. Craighead, P. Neuzil, C. Campagnolo, C. Batt, B. Ilic, D. Czaplowski, M. Zalalutdinov, and H. G. Craighead, "Single cell detection with micromechanical oscillators," *J. Vac. Sci. & Technology B*, vol. 2825, no. 2001.
- [33] D. Ramos, J. Tamayo, J. Mertens, M. Calleja, L. G. Villanueva, and a Zaballo, "Detection of bacteria based on the thermomechanical noise of a nanomechanical resonator: origin of the response and detection limits.," *Nanotechnology*, vol. 19, no. 3, p. 035503, 2008.
- [34] J. Kalia and R. T. Raines, "Advances in Bioconjugation," *Curr Org Chem.*, vol. 14, no. 2, pp. 138–147, 2010.
- [35] T. Braun, M. K. Ghatkesar, N. Backmann, W. Grange, P. Boulanger, L. Letellier, H. Lang, A. Bietsch, C. Gerber, and M. Hegner, "membrane protein – ligand interactions using microcantilever array sensors," *Nat. Nanotechnol.*, vol. 4, no. March, pp. 179–185, 2009.
- [36] B. N. Johnson and R. Mutharasan, "Biosensors," in *Resonant MEMS–Fundamentals, Implementation and Application*, 2015.
- [37] S. Banerji, P. Michalik, D. Fernández, and J. Madrenas, "CMOS-MEMS resonant pressure sensors : optimization and validation through comparative analysis," *Microsyst. Technol.*, 2016.

- [38] V. Mortet, R. Petersen, K. Haenen, and M. D. Olieslaeger, "Wide range pressure sensor based on a piezoelectric bimorph microcantilever," *Appl. Phys. Lett.*, vol. 133511, no. 2006, 2014.
- [39] O. Brand, R. Lenggenhager, and H. Baltes, "Influence of Air Pressure on Resonating and Thermoelectric Microstructures Realized with Standard IC Technologies," *IEEE*, pp. 195–198, 1993.
- [40] A. K. Pandey, R. Pratap, and F. S. Chau, "Effect of Pressure on Fluid Damping in MEMS Torsional Resonators with Flow Ranging from Continuum to Molecular Regime," *Soc. Exp. Mech.*, pp. 91–106, 2008.
- [41] W. Heywang, K. Lubitz, and W. Wersing, *Piezoelectricity Evolution and Future of a Technology*. 2008.
- [42] T. Kamohara, M. Akiyama, N. Ueno, K. Nonaka, N. Kuwano, T. Kamohara, M. Akiyama, N. Ueno, and K. Nonaka, "Local epitaxial growth of aluminum nitride and molybdenum thin films in fiber texture using aluminum nitride interlayer Local epitaxial growth of aluminum nitride and molybdenum thin films in fiber texture using aluminum nitride interlayer," *Appl. Phys. Lett.*, vol. 071919, no. 2006, 2013.
- [43] R. B. Karabalin, M. H. Matheny, X. L. Feng, E. Defaÿ, G. Le Rhun, C. Marcoux, S. Hentz, P. Andreucci, M. L. Roukes, R. B. Karabalin, M. H. Matheny, X. L. Feng, E. Defaÿ, G. Le Rhun, and C. Marcoux, "Piezoelectric nanoelectromechanical resonators based on aluminum nitride thin films Piezoelectric nanoelectromechanical resonators based on aluminum nitride thin films," *Appl. Phys. Lett.* 95, vol. 103111, 2009.
- [44] N. Sinha, G. E. Wabiszewski, V. V Felmetzger, and S. M. Tanner, "Piezoelectric aluminum nitride nanoelectromechanical actuators," *Appl. Phys. Lett.* 95, vol. 053106, 2009.
- [45] P. Ivaldi, J. Abergel, M. H. Matheny, L. G. Villanueva, R. B. Karabalin, M. L. Roukes, P. Andreucci, S. Hentz, and E. Defaÿ, "50 nm thick AlN film-based piezoelectric cantilevers for gravimetric detection," *J. Micromechanics Microengineering*, vol. 21, no. 8, p. 085023, 2011.
- [46] V. M. Pantojas, W. Otano-Rivera, and J. N. Caraballo, "Statistical analysis of the effect of deposition parameters on the preferred orientation of sputtered AlN thin films," *Thin Solid Films*, vol. 492, pp. 118 – 123, 2005.
- [47] S. K. E. Ramadan and S. Evoy, "Low Temperature Reactive Sputtering of Thin Aluminum Nitride Films on Metallic Nanocomposites," pp. 1–22, 2015.
- [48] P. J. Kelly and R. D. Arnell, "Magnetron sputtering : a review of recent developments and applications," *Vacuum*, vol. 56, pp. 159–172, 2000.
- [49] D. K. Maurya, A. Sardarinejad, and K. Alameh, "Recent Developments in R.F. Magnetron Sputtered Thin Films for pH Sensing Applications—An Overview," *Coatings*, pp. 756–771, 2014.
- [50] M. Ishihara, S. J. Li, H. Yumoto, K. Akashi, and Y. Ide, "Control of preferential orientation of AlN films prepared by the reactive sputtering method," *Thin Solid Films*, vol. 316, pp. 152–157, 1998.
- [51] S. Marauska, T. Dankwort, H. J. Quenzer, and B. Wagner, "Sputtered thin film piezoelectric aluminium nitride as a functional MEMS material and CMOS compatible process integration," *Procedia Eng.*, vol. 25, pp. 1341–1344, 2011.

- [52] D. R. Pelley, D. J. Christie, B. D. Fries, A. E. Industries, and F. Collins, "Pulsed DC Power for Magnetron Sputtering : Strategies for Maximizing Quality and Flexibility," *Soc. Vac. Coaters*, pp. 183–186, 2014.
- [53] H. Jin, B. Feng, S. Dong, C. Zhou, J. Zhou, Y. Yang, T. Ren, J. Luo, and D. Wang, "Influence of Substrate Temperature on Structural Properties and Deposition Rate of AlN Thin Film Deposited by Reactive Magnetron Sputtering," *J. Electron. Mater.*, 2012.
- [54] S. Khan, M. Shahid, A. Mahmood, A. Shah, I. Ahmed, and M. Mehmood, "Texture of the nano-crystalline AlN thin films and the growth conditions in DC magnetron sputtering," *Prog. Nat. Sci. Mater. Int.*, vol. 25, no. 4, pp. 282–290, 2015.
- [55] R. K. Choudhary, P. Mishra, A. Biswas, and A. C. Bidaye, "Structural and Optical Properties of Aluminum Nitride Thin Films Deposited by Pulsed DC Magnetron Sputtering," *ISRN Mater. Sci.*, vol. 2013, 2013.
- [56] M. Dubois and P. Mural, "Stress and piezoelectric properties of aluminum nitride thin films deposited onto metal electrodes by pulsed direct current reactive sputtering," *J. Appl. Phys.*, vol. 89, 2001.
- [57] J. Kim and S. Jeong, "Effects of Deposition Parameters on AlN Film Growth Using Reactive DC Magnetron Sputtering," *J. Korean Phys. Soc.*, vol. 38, no. 1, pp. 19–24, 2001.
- [58] H. Okano, Y. Takahashi, T. Tanaka, K. Shibata, and S. Nakano, "Preparation of c-Axis Oriented AlN Thin Films by Low-Temperature Reactive Sputtering," *Appl. Phys.*, vol. 31, 1992.
- [59] W. J. Meng, J. A. Sell, T. A. Perry, G. L. Eesley, M. J. A. Sell, T. A. Perry, and G. L. Eesley, "Real time stress measurements and elastic constant of aluminum nitride thin films on Si (111)," *J. Vac. Sci. Technol. A* 11, vol. 1377, 1992.
- [60] F. Martin, P. Mural, and M.-A. Dubois, "Thickness dependence of the properties of highly c-axis textured AlN thin films," *Am. Vac. Soc.*, pp. 361–365, 2004.
- [61] A. Artieda, M. Barbieri, C. S. Sandu, P. Mural, A. Artieda, M. Barbieri, C. S. Sandu, and P. Mural, "Effect of substrate roughness on c-oriented AlN thin films Effect of substrate roughness on c-oriented AlN thin films," *J. Appl. Phys.* 105, vol. 024504, no. 2009, 2009.
- [62] R. B. Karabalin, L. G. Villanueva, M. H. Matheny, J. E. Sader, and M. L. Roukes, "Stress-Induced Variations in the Stiffness of Micro- and Nanocantilever Beams," *Phys. Rev. Lett.*, vol. 236101, no. June, pp. 1–5, 2012.
- [63] D. Deniz, T. Karabacak, and J. M. E. Harper, "Competitive growth mechanisms of aluminum nitride thin films deposited by off-normal reactive magnetron sputtering," *J. Appl. Phys.* 103, vol. 083553, pp. 3–6, 2008.
- [64] E. Alfonso, J. Olaya, and G. Cubillos, "Thin Film Growth Through Sputtering Technique and Its Applications," 2011.